INVESTIGATION ON THE IMPACT DAMAGE OF GLASS USING THE COMBINED FINITE/DISCRETE ELEMENT METHOD

XUDONG CHEN

BEng, MSc

A thesis submitted to the University of Birmingham

for the degree of

DOCTOR OF PHILOSOPHY

School of Civil Engineering

University of Birmingham

March 2013

TO MY FAMILY

ABSTRACT

Glass and laminated glass are widely used for structural members in industry. To investigate how they fracture under impact as well as the subsequent fragmentation, the combined finite-discrete element method (FEM/DEM) which incorporates finite elements into single discrete elements was employed in this thesis.

The mode I fracture model was extended for glass by changing the strain softening curve to a bilinear-like exponential decay shape. Analysis based on this model was performed and numerical examples in both 2D and 3D were investigated, showing the applicability and reliability of the mode I model. A parametric study was carried out and the conclusion was reached that the tensile strength, fracture energy and thickness are the top three parameters in improving the performance of monolithic glass under impact.

Two mixed mode (I + II) fracture models (the elasto-plastic fracture model and the scaling model) were developed for the glass and the interface in laminated glass. The elasto-plastic model had some similarity with the Mode I model, while some modification is needed for the scaling model. Results on laminated glass from the FEM/DEM were compared and verified with that from FEM, DEM and experiments. A parametric study on the laminated glass was performed, showing that it had more energy absorption capacity than monolithic glass. Also, the relationship between the stiffness of interlayer and delamination was studied.

ACKNOWLEDGEMENTS

This thesis could not have happened without the support and encouragement from the University of Birmingham and the Chinese Scholarship Council, who provided the funding for the research.

I would like to express my gratitude to my supervisors, Professor Andrew H C Chan and Dr Jian Yang, who guided, supported and advised me on the research throughout my PhD study.

I would like to thank Professor Antonio Munjiza from the Queen Mary, University of London. He provided the FEM/DEM program and support without any reservation. Dr Zhou Lei and Dr Dong Xu also helped me with some technical issues on that program.

I also would like to show my appreciation to the High Performance Computation (HPC) specialist Paul Hatton from the IT service, University of Birmingham. He helped figure out the execution of the FEM/DEM program on the university HPC facility and improved its efficiency.

The majority of the computations in this thesis were performed on the University of Birmingham's BlueBEAR HPC service, which was purchased through HEFCE SRIF-3 funds (see http://www.bear.bham.ac.uk for more details). The computer in the Birmingham Centre

for Resilience Research and Education also contributed some results in this thesis. These facilities are highly appreciated.

I should thank my parents and grandparents, who endured my absence from China and encouraged me continuously during my stay in Britain. I should also extend the thanks to the administrative staffs in the School of Civil Engineering, who helped me deal with cumbersome affairs that a PhD student has to face to. Last but not least, I would like to thank my colleagues, friends, and all the other people that helped me during my PhD study but have not been explicitly mentioned here.

CONTENTS

LIST OF SYMBOLS

Chapter 1

σ	Failure stress of annealed glass
n	Constant depends on the environment
T	Duration of load
σ_H	Failure bending stress of heat-strengthened glass
σ_R	Residual compressive surface stress

Chapter 2

$2a$	Crack length in a infinite elastic plate
E	Young's modulus
2γ	Surface energy
σ_f	Fracture stress
G	Fracture energy
K	Stress intensity factor
w	Opening in Hillerborg's model
$H(x)a_I$	Heaviside enrichment term
$\sum_{\alpha=1}^{4} F_\alpha(x) b_I^\alpha$	Crack tip enrichment term
u_I	Conventional FE shape function

Chapter 3

i	Number of discrete elements
f_i	Net external force i
t_i	Net external torque i
m_i	Mass of discrete element i
r_i	Position of discrete element i
I_i	Moment of inertia of discrete element i
ω_i	Angular velocity of discrete element i
dA	The penetration of any elemental area
$d\mathrm{f}_\mathrm{t}$	An infinitesimal contact force
P_c	Point belongs to the contactor
P_t	Point belongs to the target
$grad$	The gradient
φ_c	Potentials on the contactor
φ_t	Potentials on the target
S	Overlapping area
f_c	Contact force
A_1, A_2, A_3	Sub triangles inside the discrete element
E_p	Contact penalty parameter
$\varphi(P_G)$	Potential of Gauss point
V	Overlapping volume

o	Opening in the FEM/DEM
s	Sliding in the FEM/DEM
d	Damage index in the FEM/DEM
$d_e(o, s)$	Elastic limit
$d_t(o, s)$	Ultimate damage state
x_i, $i = 0-3$	Coordinates of joint element in x direction
y_i, $i = 0-3$	Coordinates of joint element in y direction
elx	The x component of the middle line of joint element
ely	The y component of the middle line of joint element
h	The length of the middle line of joint element
$o1$	The opening distance of Gauss point 1
$s1$	The sliding distance of Gauss point 1
$rdis$	Relative displacement in 3D joint element
$vnor$	Normal vector of the middle plane in 3D joint element
s_x, s_y, s_z	The x, y and z components of sliding vector

Chapter 4

K_c	The critical stress intensity factor
σ	Bonding strength
f_t	Tensile strength
δ	Separation

δ_c	The critical separation
δ_P	The separation when bonded stress reaches the tensile strength
a, b, c	Constants
D	Independent variable indicating the fracture damage index
z	Heuristic parameter
Δt	Time step
ρ	Material density
p_1	Penalty parameter /YD/YDPE/D1PEPE in the FEM/DEM
p_2	Penalty parameter /YD/YDPJ/D1PJPE in the FEM/DEM
α	Coefficient
d	Allowed penetration
λ	Lamé elastic constant
ν	Poisson's ratio

Chapter 5

κ	Non-dimensional parameter
h	Thickness
E_k	Kinetic energy of the projectile
v	Impact velocity
α	Impact angle
v_H	Horizontal component of impact velocity

v_V	Vertical component of impact velocity
h_o	The depth of horizontal crack from the upper surface of the beam
η	Ratio of the characteristic size of projectile to the beam thickness
EI	Bending stiffness
b	The width of the beam

Chapter 6

ε	Strain
F	Yield surface
$\bar{d}$	Current damage index
$f_1(\bar{d})$	Strain softening curves for Mode I
$f_2(\bar{d})$	Strain softening curves for Mode II
σ_{ult}	Ultimate normal stress, equals to the tensile strength f_t
τ_{ult}	Ultimate tangential stress, equals to the shear strength f_s
F_0	Initial intact surface
F_1, F_2	Intermediate yield surfaces
σ_i	The stress of previous time step
δ_i	The separation of previous time step
δ_{i+1}	The current separation
$d\varepsilon$	Increment of separation
D_e	Decoupled elastic matrix

D_{ep}	Coupled elasto-plastic matrix
n_g	Associated plasticity
H	Hardening modulus
K_{Ic}	Critical Mode I stress intensity factor
K_{IIc}	Critical Mode II stress intensity factor
$K_{I\max}$	Maximum Mode I stress intensity factor
$K_{II\max}$	Maximum Mode II stress intensity factor
T	Detection function
o_c, s_c	Current state of separation
o'_{ult}, s'_{ult}	Reduced new ultimate separation
o_{c1}, s_{c1}	The opening and sliding of step one
o_{c2}, s_{c21}	The opening and sliding of step two
o_{ult1}, s_{ult1}	The ultimate opening and sliding for step one
o_{ult2}, s_{ult2}	The ultimate opening and sliding for step two
f_{t1}, f_{s1}	The tensile and shear stress for step one
f_{t2}, f_{s2}	The tensile and shear stress for step two
σ_{c1}, τ_{c1}	The normal and shear stress of step one
σ_{c2}, τ_{c2}	The normal and shear stress of step two

Chapter 7

h_o	The thickness of outer glass layer

h_i	The thickness of inner glass layer
h_{PVB}	The thickness of PVB
K_l	Residual kinetic energy of laminated glass after simulation
K_m	Residual kinetic energy of monolithic glass after simulation
K_i	The initial kinetic energy
i	Index assessing the energy absorption capacity

LIST OF ABBREVIATION

2D	Two-dimensional
3D	Three-dimensional
BVP	Boundary value problem
CDM	Continuum damage mechanics
CTOD	Crack tip opening displacement
DEM	The discrete element method
FEA	The finite element analysis
FEM	The finite element method
FEM/DEM	The combined finite-discrete element method
HPC	High Performance Computation
LDEC	Livermore distinct element code
LEFM	Linear elastic fracture mechanics
MCS	Maximum circumferential stress
MERR	Maximum energy release rate
MPI	Message Passing Interface
MSED	Minimum strain energy density
MTS	Maximum tangential stress
NBS	No Binary Search
PMMA	Polymethyl methacrylate

PVB	Polyvinyl butyral
SGP	SentryGlas® Plus
SHPB	Split Hopkinson pressure bar
XFEM	The extended finite element method

INTRODUCTION

1.1 Project Background

As a man-made material, the time when humans started making glass can be traced back to around 10,000 BC in Egypt (Sedlacek et al., 1995). Archaeological findings (Dussubieux et al., 2010) demonstrated that in ancient times, soda glass rich in alumina was rare around the Mediterranean area as well as the Middle East due to the complexity of production and lack of essential techniques. Before 1,890 AD, the development of glass industry was slow (Axinte, 2011). Due to its transparency and resistance to chemical agents, most glass was provided for upper class decoration and equipment in chemistry laboratories, such as flasks and containers.

In the 19th century, following the invention of the Siemens-Martin firing method, mass glass production was made possible (Sedlacek et al., 1995). This resulted in the application of glass to windows and facades, like crystal palaces and greenhouses.

Around 1960, Sir Alastair Pilkington introduced a new revolutionary manufacturing method for float glass production, which is still in use and covers 90% of float glass production today (Axinte, 2011). Since then, float glass (or flat glass) has gained dominant market share for windows, facades, roofs and etc. As a development, new types and varieties of glass have been introduced from time to time. During the 1970s, special glass for storing radioactive

wastes was also made available.

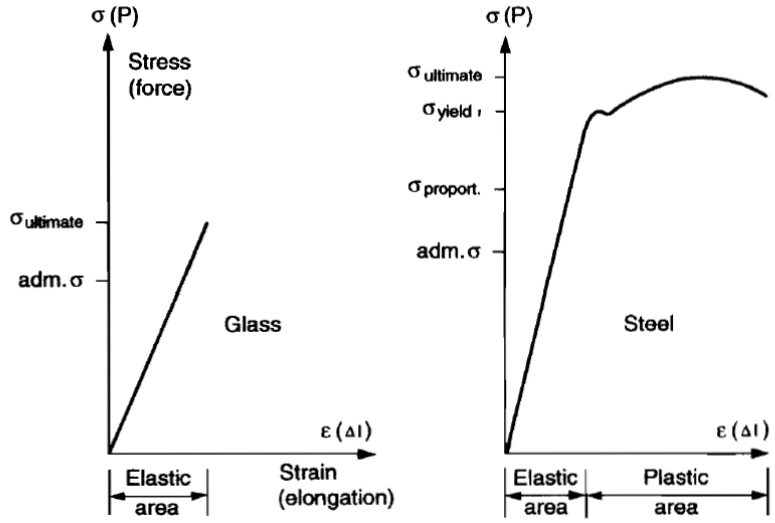

Figure 1.1 Stress-strain curves of glass and steel (after Sedlacek et al., (1995))

Although the elastic properties and density of glass are similar to those of aluminium (see Table 1.1), it does not exhibit sufficient ductility and provide sufficient warning before damage occurs due to its brittleness. Thus glass can be considered as an ideally brittle material that does not exhibit yielding and hardening (Figure 1.1).

	Annealed glass	Toughened glass	Aluminium
Strength	7-28 N/mm^2	59-150 N/mm^2	130 N/mm^2
Young's Modulus	70 kN/mm^2	70 kN/mm^2	70 kN/mm^2
Density	2400kg/m^3	2400kg/m^3	2600kg/m^3
Poisson's ratio	0.22	0.22	0.34

Table1.1 Properties of glass and aluminium (after Ledbetter et al. (2006))

1.2 Types and Application of Glass

In industry, glass is manufactured into different products using different methods catering for different purposes. According to Axinte (2011), glass can be classified as common glass (basic and decorative) and special glass. Among these types: annealed, heat-strengthened, toughened and laminated glasses are commonly used in civil engineering.

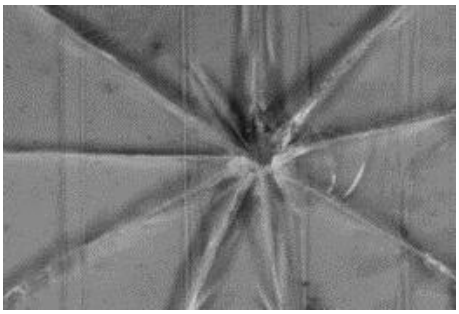

(a) Annealed glass (Bouzid et al., 2001)

(b) Heat-strengthened glass (mimosa.com.sg, n.d.)

(c) Toughened glass (mimosa.com.sg, n.d.)

(d) Laminated glass (Laminated Glass (SR002), n.d.)

Figure 1.2 Shatter patterns of different types of glass

1.2.1 Annealed Glass

Annealed glass, or float glass, is cooled gradually from high to room temperature. This process eliminates the residual stress to the maximum extent and allows them to be cut conveniently. It is the most commonly available type and also the most vulnerable type of glass (Masters et al., 2010). Large shards with sharp edges (Figure 1.2a) will be produced when the glass breaks. Penetration and collapse of the glass structure may occur. The failure stress of annealed glass is also relatively low. Should σ be the failure stress of annealed glass, n is a constant depends on the environment and T equals the duration of load, Sedlacek et al. (1995) gave the relation between failure stress and load duration:

$$\sigma^n T = \text{constant} \tag{1.1}$$

The curve plotting failure stress versus load duration was shown in Figure 1.3, where n=16 is normally used in building design and the characteristic bending stress is 45MPa according to EN 572-1. It should be noted that this visco-elasto-plastic behaviour is not considered in this thesis.

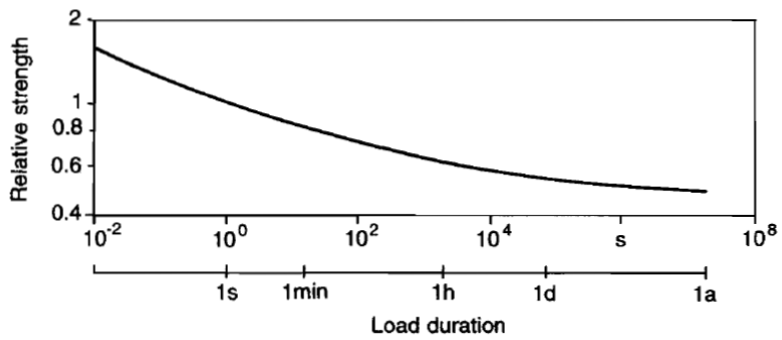

Figure 1.3 Dependence of the bending strength on load duration (after Sedlacek et al., (1995))

1.2.2 Heat-strengthened Glass

Heat-strengthened glass has to experience a controlled heating and cooling process to enable a permanent compressive surface residual stress. Applying the superposition principle (Ledbetter, 2006), if the failure bending stress of heat-strengthened glass is σ_H, and the residual compressive surface stress is σ_R, an expression in equation (1.2) can be obtained:

$$\sigma_H = \sigma + \sigma_R \tag{1.2}$$

where σ is the strength of annealed glass mentioned previously. Obviously, the existence of the residual compressive surface stress will enable the heat-strengthened glass a higher bending strength than that of annealed glass. EN 1863-1 requires a 70MPa characteristic strength for heat-strengthened glass. Despite its enhanced strength, the damage pattern of heat-strengthened glass is similar to that of annealed glass (Figure 1.2b), producing large sharp fragments which pose potential injury to users.

1.2.3 Toughened Glass

If the glass is processed in the same way as heat-strengthened glass but been cooled more rapidly, toughened glass, which is also called fully-tempered glass by the Americans, will be produced. It is heated in a furnace to approximately 640 Centigrade and then chilled by cold

air from a jet system. A residual compressive surface stress over 69MPa can be obtained and a higher strength for toughened glass can be achieved (characteristically 120MPa in accordance with EN 12150-1). In the event of breakage, numerous small blunt fragments will be generated, normally diced (Figure 1.2c).

Sedlacek et al. (1995) pointed out that the higher the pre-stress, the higher the disintegrating force will be once the toughened glass gets damaged, and the smaller the fragments will be as a result. These fragments do not have sharp edges as annealed and heat-strengthened glass does, and deep cutting injuries are unlikely to happen either. However, small fragments are not able to resist residual load once breakage occurs, resulting in a full or partial collapse of the glass structure.

1.2.4 Laminated Glass

Laminated glass is an assembly of glass sheets together with one or more interlayer(s) (Figure 1.4). Commonly found makeup can be glass / interlayer (0.38 or 0.76mm) / glass.

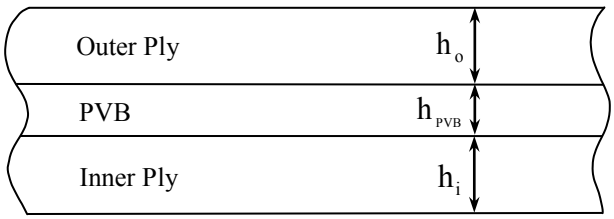

Figure 1.4 Illustration of the composition of laminated glass

It is manufactured in an autoclave under high temperature and pressure. In general, laminated glass can be developed from any type of glass mentioned above (annealed, heat-strengthened or toughened). The strength, breakage and post-failure behaviour of laminated glass depend heavily on the glass type, glass thickness, interlayer type and its thickness. Different types of glass sheets lay different emphasises. Toughened glass is used to provide sufficient strength to resist load while annealed and heat-strengthened glass are used to govern the post-failure behaviour. Film interlayer for laminated glass is normally polyvinyl butyral (PVB) for construction and automobile but stiff resins like SentryGlas® Plus (SGP) is also prevalent in some applications (Bennison et al., 2002; Delincé et al., 2008).

The inclusion of interlayer makes the laminated glass a complicated composite material. Under sustained load, layered behaviour will be presented but for short load duration, more shear transfer can be provided. Research (Behr et al., 1993; Norville, 1999) has demonstrated that for wind gust, laminated glass behaves in similar way as monolithic glass of the same thickness.

Post-failure analysis of laminated glass is of significance. Once shattered, spider web cracks (Figure 1.2d) will be produced and the interlayer will hold the broken glass fragments if there is enough adhesion. This feature is particularly important as potential injury and damage caused by sharp pieces of flying glass fragments can be minimized. Quality requirements for laminated glass can be found, for instance, in ASTM C 1172 and EN ISO 12543.

1.2.5 Applications of Structural Glass

Back to its original form, the most common application of glass for structural use is windows glazing and facades. Roof is also popular as light can pass through freely without any obstruction. In these cases, only the load imposed directly onto it, such as snow, wind and self-weight will be carried by the glass. Based on the definition in Ledbetter et al. (2006), the term “glass structures” includes glass elements that transfer loads other than those imposed directly on to it. Examples include beams, columns, walls, balustrades, stairs, floors, bridge etc.

Saunders and his group published a guide book on structural use of glass for the Institution of Structural Engineers in 1999 and some examples of glass structures are listed. Glass beams are generally simply supported or clamped and early examples can be found in the work of Dewhurst McFarlane (Dawson, 1995) and Nijsse (1993). A notable example is the entrance canopy to the Yuraku-cho underground station in Tokyo (Dawson, 1997), compromising 4 lengths of glass bolted together (Figure 1.5a). Glass columns and load-bearing walls are rare due to its brittleness as it can fail in a sudden way without any warning. A representative example (Figure 1.5b) is the 13.5m high, ground-based glass wall at the Royal Opera House, Covent Garden, London (Dodd, 1999).

(a) Canopy to underground station, Japan (Cantilevered glass canopy, n.d.)

(b) Glass wall at Royal Opera House, UK (MacMillan ballet highlight, n.d.)

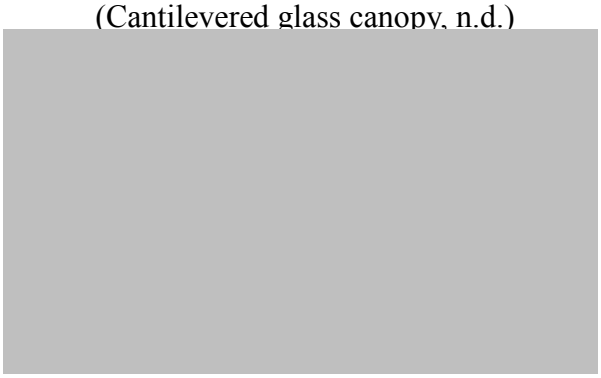

(c) Grand Canyon Skywalk, US (Top tourist attraction, n.d.)

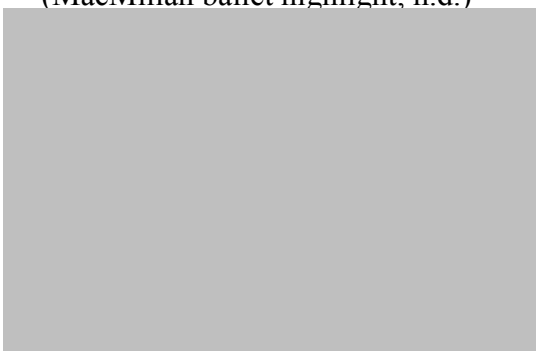

(d) Sears Tower Glass Platform, US (Sears Tower Scary, n.d.)

Figure 1.5 Examples of glass structures in the world

Many years have passed since 1999. Due to the aesthetic appearance and transparency, more and more challenging glass applications emerged in civil engineering during past years. One of the examples is the Grand Canyon Skywalk (Figure 1.5c) in Arizona, the United States. The glass observation deck of the Skywalk enables the tourists to gaze deep into the abyss without any visual barriers. In 2009, four reinforced glass “balconies” (Figure 1.5d) were added to the Sears Tower (now Willis Tower) for visitors. With its four 10 foot by 10 foot compartments protruding 4.3 feet from the building's 103rd floor observation room, the platform provides a completely transparent space to generate the sensation of hovering over Chicago.

Whether it is the entrance canopy in Tokyo or the modern platform in Chicago, impact (caused by dropping objects or windborne debris) is always a great threat to these brittle glasses. Structural analysis is needed to investigate these modern, high-technique constructions. Also, these investigations will involve the fracture and fragmentation of glass due to its brittle nature. As a result, genuine dynamic analysis is vital to the research on the fracture of glass. Obviously, traditional analytical approaches are not capable of solving such sophisticated responses. Experimental tests are usually carried out with the support of high-speed photography, which is indispensable if transient response is needed (Baird, 1947; Salman and Gorham, 2000; Hopper et al., 2012). With the development of computer hardware and improvement of numerical algorithms, Virtual Experimentation Labs (VELs) are becoming a reliable and efficient approach to engineers and researchers (Flocker and Dharani, 1997b; Sun et al., 2005; Timmel et al., 2007). Numerical simulation is also quite attractive due to its comparative low cost and high manipulability.

Nowadays, the most commonly used software for analysing engineering problems is based on the finite element method (FEM) formulation (Clough, 1960; Zienkiewicz and Taylor, 1967), which excels in solving continuum problems but considered not to be so helpful for discrete modelling. These discrete problems usually involve large non-linear displacements and considerable number of moving fragments. Although some new progress has been achieved in XFEM and showed its applicability to cracks (Areias and Belytschko, 2005), it is still difficult

to solve these issues mentioned above. For discrete problems, typically the fracture of glass followed by the consequent fragmentation and interaction, the best way of solving it is to use the discrete element method (DEM). The combined finite-discrete element method (FEM/DEM) is a special extension that belongs to the DEM family with the combination of the FEM and DEM techniques. It originated in Swansea University (Munjiza, 1992; Munjiza and Bicanic, 1994) and was developed at Queen Mary, University of London and an accompanying open-source FEM/DEM program "Y" (Munjiza, 2000, 2004) has been released. In this method, each macro-element is a discrete element, making the method quite capable of achieving any discrete behaviour. Within the discrete macro-element, a finite element formulation is embedded with one or more finite elements, providing a more accurate estimate of the contact forces and deformation of fragments. The FEM/DEM can be considered as "the discrete element methods combining with finite element formulations".

Further details on the FEM/DEM will be introduced in Chapter 3. It is a useful tool for structural engineers to understand the behaviour of glass under impact. Based on the knowledge of damage process, a safe and robust design could be produced and contribution to the industry can be achieved.

1.3 Aim and Objectives

The aim of this thesis is to study the impact response and breakage behaviour of monolithic

and laminated glass under hard body impact using the combined finite-discrete element method. Based on this aim, several objectives are to be achieved.

(1) Use the FEM/DEM to simulate monolithic and laminated glass - Simulate the different types of failure in monolithic and laminated glass. Compare and verify the results with other data: FEM, DEM and experimental test.

(2) Develop new fracture models for glass and laminated glass - This includes developing suitable models for glass and the interface between glass and the interlayer in laminated glass. Also, the mixed-mode and unloading has to be considered.

(3) Perform parametric studies on glass and laminated glass - Study the influences of parameters on the response of monolithic and laminated glass under impact. Find out the way to improve the performance of glass and laminated glass. Provide the guidance for manufacturing and design.

1.4 Major Innovations

In this section, key innovations of this thesis are briefly addressed.

(1) The FEM/DEM is a relatively new method. Although it has been used in some other areas

(such as rock failure and molecular dynamics), application in the glass and laminated glass fracture analysis has not been done. In this research, simulation of damage on glass and laminated glass subject to impact using the FEM/DEM was provided, yielding a more accurate estimate of the results.

(2) The original fracture model in the FEM/DEM program is for modelling Mode I concrete fracture only. The combined single and smeared crack model and strain-softening curve based on the experimental observation of concrete were used. In this thesis, by changing the shape of the strain-softening curve, the Mode I fracture model was extended to the modelling of fracture of glass.

(3) A mixed Mode I+II elasto-plastic fracture model was developed for the glass as well as the interface between the glass and interlayer of laminated glass. Elasto-plastic models are commonly used in ductile and quasi-brittle materials, such as metal and concrete. Since glass is very brittle and the elastic-plastic behaviour is not obvious, the implementation proved the applicability of the elasto-plastic model to brittle glass material while some other researchers use the continuum damage mechanics (Sun et al., 2005) or equivalent static load (Flocker and Dharani, 1997b). Further study on this model demonstrated that for glass, Mode I fracture is still the dominant mode of failure.

(4) Another mixed Mode I+II model, a scaling fracture model was developed based on the

reduction of stress from the original strain-softening curve. The idea of a scaling factor can be applied to the softening curve with any shape. However, investigation into this model suggested that the basic principle of the cohesive model can be violated, which may result in unrealistic crack patterns. Further modification to this model would be required if it is to be used for the modelling of glass fracture in the future.

(5) The thesis performed parametric studies on both monolithic and laminated glass. Guidance for designing and manufacturing the glass were concluded, listing the top three factors in improving the performance of monolithic glass: tensile strength, fracture energy and the thickness. The propagation of stress waves within the glass body was investigated by employing classical theory (Kolsky, 1953). The relationship between fracture pattern and reflection of stress waves were investigated and revealed. Some conclusions of the parametric study also have been used in the arguments of other chapters in this thesis.

For laminated glass, the influences of several factors were investigated, obtaining the energy absorption capacity of the laminated glass and its advantage over its monolithic counterpart. Also, the relationship between the stiffness of interlayer and delamination was established.

1.5 Layout of the Thesis

This thesis comprises eight chapters. Following the summary, the reference is provided.

In chapter 2, literature on the fracture of glass (including theoretical, experimental and numerical approaches) was reviewed. The review on classic fracture mechanics started from Griffith (1920), followed with experimental investigation that can be traced back to Hertz (1896). In the numerical section, literatures on FEM (including XFEM), DEM and FEM/DEM were reviewed, respectively. Conclusion was achieved that the FEM/DEM could be applied for the fracture initiation and propagation of glass subject to impact.

In the methodology chapter, chapter 3, the FEM/DEM as well as its program "Y" was discussed in details. Basic equations on the FEM/DEM and evaluation of contact forces along with the supporting pre/post-processing programs were introduced.

Chapter 4 focused on the Mode I fracture model of glass. It is extended from the single and smeared crack model that original implemented in the FEM/DEM program, with a different strain-softening descending curve. Sensitivity analysis was carried out to investigate the influences of element size, time step and penalty parameters. Numerical examples were shown, with a Hertzian type cone obtained in 2D and radial cracks in 3D.

Chapter 5 performed the parametric study based on 2D for the monolithic glass. The fracture model used in this chapter was the one developed in Chapter 4. Parameters investigated included the tensile strength, fracture energy, impact velocity and angle, stress wave

propagation, projectile size, thickness of glass and etc. Among these factors, tensile strength, fracture energy and thickness are considered the top three that can improve the performance of monolithic glass under impact.

Chapter 6 discussed mixed mode modelling. Two mixed mode (I + II) fracture models were developed for glass and the interface in laminated glass: the elasto-plastic model and the scaling model. Brief reviews on mixed-mode fracture and the elasto-plastic model was performed at the beginning of this chapter. After introducing the mixed fracture models as well as their advantages and limits, laminated glass was investigated using the elasto-plastic model, showing its good energy absorption ability.

Chapter 7 has two topics: comparative study and parametric study. In the comparative study, results from the FEM/DEM were compared, discussed and verified with that from other research using the FEM, DEM and test. In the parametric study, input energy, strength of interface and the Young's modulus of interlayer were investigated and their influences on the responses of laminated glass under impact were addressed.

And finally a summary was made in chapter 8. Conclusions of what this thesis has achieved were given and aspects that should be improved for the FEM/DEM were listed. The future work that could be done on the fracture analysis of glass (including laminated glass) subject to impact was also provided.

LITERATURE REVIEW

2.1 Introduction

As a transparent material, glass is increasingly used despite its inherent brittle properties. The role of glass in buildings is moving forward from non-structural elements, such as windows and facades, to load-bearing ones, e.g. beams, staircases and balconies. The all glass squash courts (Hill, 1982) in early 1980s set off the research on the structural properties of glass.

This chapter reviews literature on the structural application and fracture investigation on glass. Shortly after the introduction of glass application in section 2.2, classic literature on the fracture mechanics of brittle materials started from Griffith (1920) is reviewed and discussed in section 2.3, followed by the experimental and numerical investigation in section 2.4 and 2.5. In experimental investigation, work early from Hertz (1896) to recent development is concluded; while in the numerical simulation section, finite element method (FEM, including the XFEM), discrete element method (DEM) and finite discrete element method (FEM/DEM) are reviewed separately. A summary is given in the final section and the conclusion is achieved that the FEM/DEM could be applied for the fracture initiation and propagation of glass subject to impact.

2.2 Structural Application of Glass in Civil Engineering

Although the structural application of glass has become popular in recent decades, research on the damage of glass, particularly fracture, has enjoyed a long history. Preston (1926) demonstrated that the manner of breakage in annealed glass is directly related to the appearance of fracture surfaces. This view has been supported by Murgatroyd (1942) and Shand (1954). Some of the general features of fracture in glass were described by many other researchers (Holloway, 1968; Clarke and Faber, 1987; Ward, 1987).

The fracture of glass also plays an important role in other areas besides civil engineering. For forensic interpretation, the earliest record on blunt-impact window fracture was published by Russian criminologist Matwejeff (1931). McJunkins and Thornton (1973) also stated in their review on glass fracture that fragments caused by impact are usually reconstructed for criminal investigation. This was further verified by Haag and Haag (2006) on the bullet impact on glass. In aeronautics, hypervelocity impact at the magnitude of km/s on glass was taken into account. A review by Cour-Palais (1987) presented the research carried out during NASA Apollo lunar missions between 60s and 70s in the last century. As to the development, a damage equation was given by Taylor and McDonnell (1997) and oblique hypervelocity impact on thick glass target was also studied (Burchell and Grey, 2001). Automotive industry investigates the fracture of glass intensively for the safety of passengers. Timmel et al. (2007) investigated the behaviour of windscreen failure subject to external projectile. On the other hand, human head impact on windshields is also a major consideration in safety control of

automotive industry (Zhao et al., 2006).

Different domains have different emphasis. For civil engineering, glass is commonly used for balconies, facades and other structural elements. In practice, glass will have to endure load from wind, blast, impact and etc. Research on the blast and pulse pressure loading posed on glass (Goodfellow and Schleyer, 2003; Norville and Conrath, 2006) provided an effective design guide for reducing human injuries. Minor and Norville (2006) studied the influence of lateral pressure on glass and a relevant design guide was given. In the work of various researchers (Rao, 1984; Calderone and Melbourne, 1993), glass behaviour under wind loading was investigated, which is significantly useful in high buildings and wind-prevalent areas. Regarding the impact, Minor (1994) indicated the response of building glazing subject to windborne debris impact, including both small and large missiles. The stress and safety for ordinary (annealed) glass liable to human impact (Toakley, 1977) was also discussed in order to minimize the injuries.

Since the monolithic glass is vulnerable under impact and other external effect, laminated glass started to be investigated and employed in industry. Early studies on laminated glass plate were carried out experimentally (Behr et al., 1985; Behr et al., 1986; Vallabhan et al., 1993). Some studies on laminated glass beam (Hooper, 1973; Norville et al., 1998) were also performed. Shutov et al., (2004) experimentally investigated laminated glass plates with different laminated strategies, such as three glass plies with two interlayers, two glass plies

with one interlayer and one outerlayer, two glass plies with one interlayer, which is the most commonly used one. All the research indicated that laminated glass can significantly absorb impact energy and prevent a projectile from penetrating. Meanwhile, numerical simulation using FEM were also carried out, research from Flocker and Dharani (1997a), Du Bois et al., (2003), Timmel er al., (2007) and etc. also demonstrated that laminated glass has better capacity than monolithic ones.

As seen in civil engineering, particularly the structural analysis, the response of glass elements subject to various loading is important. Since its brittle nature leads to crucial problems, the fracture of glass (both monolithic and laminated) has been widely and intensively investigated. The traditional elastic theories (Love, 1892; Timoshenko and Prokop, 1959) which based on the continuum assumption will no longer be applicable to these discrete phenomena after fracture. Development calls for new theory especially concerning its fracturing.

2.3 Fracture Mechanics of Brittle Solids

Theoretically, as an ideally brittle isotropic material, the fracture of glass has to obey some physical laws. One of the theories is the Linear Elastic Fracture Mechanics (LEFM). Although modern microscopic technique asserted that the essence of fracture is the breakage of the bonds between atoms, the cause of fracture was largely a mystery over a considerable period

in history.

Love (1892) remarked in his elasticity text that “the conditions of rupture are but vaguely understood”, however, the era of fracture from a scientific point of view was coming. In 1920, pioneering work on the quantitative connection between fracture stress and flaw size was published by Griffith (1920) and concluded in his later work (Griffith, 1924). He analysed the stress around a through-thickness elliptical flaw in an infinite elastic plate of crack length $2a$, Young’s modulus E and surface energy 2γ with an applied remote tensile stress σ perpendicular to the major axis of the ellipse (Figure 2.1) from an experiment performed by Inglis (1913) to consider the unstable propagation of a crack.

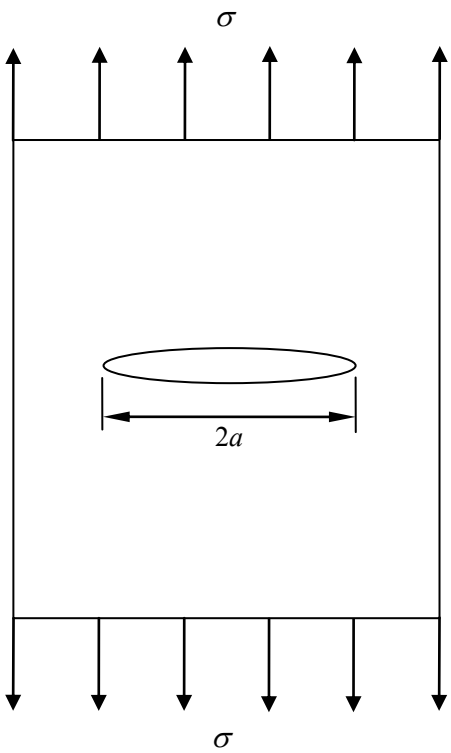

Figure 2.1 Griffith approach: an elliptical crack in a plate subject to remote tensile stress

Griffith's model gave the propagation criterion for an elliptical crack and solved the fracture stress σ_f shown in Equation 2.1:

$$\sigma_f = \sqrt{\frac{2\gamma E}{\pi a}} \tag{2.1}$$

It also correctly predicted the relationship between strength and flaw size in glass specimens. Since the model considers that work for fracture comes exclusively from surface energy, Griffith's approach only applies to ideally brittle materials. Further, as it assumes that the brittle material contains elliptical microcracks, high stress concentration was also introduced near the elliptical tips. In addition, a large gap in mathematical derivation of Griffith's work was left, where these details can now be found from other research (Hoek and Bieniawski, 1965; Jaeger and Cook, 1969).

Shortly after the Second World War, Irwin (1957) in U.S. Navy Research Laboratory extended the Griffith's model and introduced a flat crack instead of an elliptical one. This flat crack is more realistic in engineering problems and suitable for any arbitrary cracks (Anderson, 1991; Ceriolo and Tommaso, 1998). It is worth mentioning that although Irwin developed Griffith's model, the singularity at the crack tip was also introduced, which is not the correct stress state in reality as no stress should exist at free surfaces.

In Irwin (1956), the concept of strain energy release rate was developed. Energy absorbed for cracking must be larger than the critical value to create a new crack surface. If we

set $G = 2\gamma$ in (2.1), the critical state can be obtained in equation 2.2.

$$G = \frac{\sigma^2 \pi a}{E} \tag{2.2}$$

Furthermore, according to Westergaard (1939), Irwin showed that stress field in the area of crack tip can be completely expressed by the quantity *K*, namely the stress intensity factor. *K* is usually given a subscription of *I*, *II* or *III* to denote different modes of loading (Figure 2.2). In fracture mechanics (Knott, 1973; Barsom, 1987; Anderson, 1991), Mode I is for the principal load normal to the crack plane, leading to open the crack. Mode II and III are shear sliding modes and tend to slide one crack face with respect to the other, but in different planes. It is widely held that Mode I fracture is the most common and dominant type, which has been supported by Anderson (1991), Roylance (2001) and many other researchers.

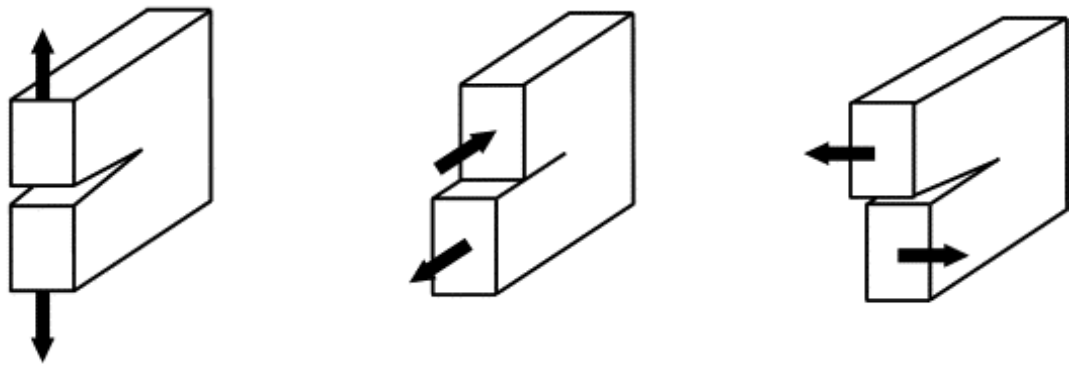

Mode I: opening Mode II: in-plane shear Mode III: out-of-plane shear

Figure 2.2 Three modes of fracture loading conditions (after Zimmermann et al., (2010))

Concerning further theoretical development on fracture mechanics, Rice (1968) developed a new parameter, J-integral, which is independent of the integration path around the crack tip. It is shown (Anderson, 1991) that the J-integral is equivalent to the energy release rate in the

analysis of fracture mechanics for brittle solids which limits its use in Linear Elastic Fracture Mechanics.

The fracture mechanics developed gradually from Griffith approach to cohesive models. Before the prominent Hillerborg's model (Hillerborg et al., 1976), some researchers attempted to include the cohesive forces into the crack tip region in order to solve the stress singularity introduced in Irwin's model. Barenblatt (1959, 1962) assumed that cohesive forces existed in a small cohesive zone near the crack tip and enable the crack face close smoothly. However, the distribution of these cohesive forces is unknown. Dugdale (1960) held the same hypothesis as Barenblatt's but considered the closing force is uniformly distributed (Figure 2.3) for elastic-perfectly plastic materials.

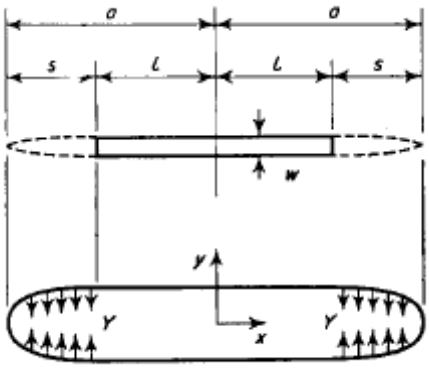

Figure 2.3 Uniform distribution of cohesive force at crack tip in Dugdale's model (after Dugdale (1960))

Although Barenblatt's and Dugdale's models proposed the concept of a cohesion zone, they

still differ from the model of Hillerborg (1976) in several important aspects (see Figure 2.4).

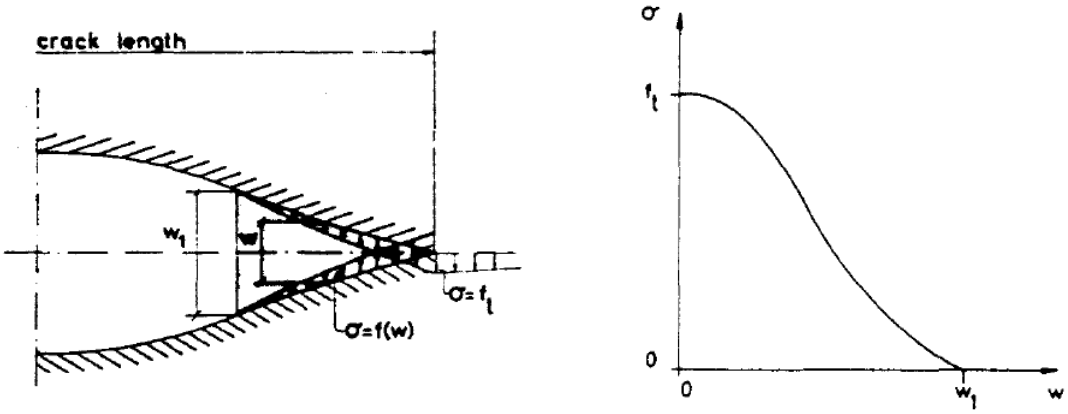

(a) Relation between σ and opening w (b) Relation of stress σ and opening w

Figure 2.4 Stress distributions along crack tip and strain softening curve in Hillerborg's model (after Hillerborg (1976))

One of these differences is that Barenblatt and Dugdale both assume a pre-existed crack in the analysis, while Hillerborg included the tension softening process through a fictitious crack. Thus there are two zones in Hillerborg's model: a real crack where no stress transfer and a damaging zone where stress can still be transferred. As a turning point, this model successfully achieved the crack transition based on the strain softening and can be implemented conveniently in numerical analysis. Its variation (Bazant, 1976; Bazant and Cedolin, 1979) considers that the closed fracture processing zone can be represented through a stress-strain softening law, making itself suitable for finite element analysis.

Although the models described above are mostly based on the Mode I loading conditions,

which is the dominant type in fracture, reviews and surveys on brittle fracture in compression never ceased and could be found in many references (Adams and Sines, 1978; Logan, 1979; Horii and Nemat-Nasser, 1986; Guz and Nazarenko, 1989a, 1989b; Myer et al., 1992). As was mentioned before, pure compression cannot fracture material as the inter-atomic bond must be stretched to enable fracture. According to Wang and Shrive (1995), no fracture will occur if material is loaded under hydrostatic compression. There is evidence (Wang and Shrive, 1993) showing that the initiation and extension of a crack under compression must involve Mode I crack propagation, or Mode I plus one or both other two shear sliding types. Wang and Shrive (1993) insisted that despite significant differences in compression and tension, the dominant mechanism of brittle fracture in compression is Mode I cracking.

Direct observations (Costin, 1989) suggested that cracks from the pre-existing flaws propagate predominantly as Mode I fracture. Lajtai (1971) stated that the propagation of tension cracks is the most noticeable event in a compression test. His later research (Lajtai et al., 1990) also claimed that Griffith theory is still fundamental to all investigations of brittle solids. This has been further verified by recent research investigations (Ougier-Simonin et al., 2011). Consequently, Mode I type cracking is still dominant and needs the most emphasis even in compression.

Thanks to the scientific efforts starting from Griffith in 1920s, the theoretical fundamentals for fracture mechanics now is approaching maturity. However, pure theoretical analysis is

difficult to be applied to sophisticated structures. Some, e.g. the Griffith and Irwin model still assume pre-existed cracks, which limited their application. The limitation of LEFM is obvious that it can only resolve the fracture initiation but can offer little help for fracture propagation. Thus a new method (such as FEM/DEM) is needed to overcome these difficulties. At the same time, researchers are also investigating the fracture of glass from other approaches, such as experimentation and numerical application.

2.4 Experimental Investigations

As a traditional and vibrant approach to explore the unknown, experimentation has never slowed its pace. Genuine specimen with genuine material properties under almost genuine testing conditions, the advantage of experimentation is obvious. In this section, reviews will be from both static and dynamic aspects. For static and quasi-static indentation, the fracture patterns will be provided; for dynamic investigations, drop-weight test is commonly used for low velocity impact. For higher loading rate, Hopkinson pressure bar test will be discussed.

Tracing back to the late 19th century, Hertz (1896) initially observed that a cone shaped crack (Figure 2.5) will be generated on the material surface when a hard spherical indenter is pressed normally into a brittle material.

Figure 2.5 Hertzian cone crack formed by indentation of a blunt indenter (after Roesler (1956))

Later, Huber (1904) gave a detailed discussion on the stress distribution for the contact between two elastic spheres or a sphere and a half-space. However, this analysis just gives an accurate prediction of the stress distribution in the glass plate before fracturing begins. As long as a new fracture surface is formed, the stress distribution will be modified and Huber's approach will not apply any more. Although the stress distribution before the elastic limit has roughly been solved, Hertzian indentation as well as the cone crack has received considerable attention from various researchers (Tsai and Kolsky, 1967; Johnson et al., 1973; Hills and Sackfield, 1987; Warren and Hills, 1994; Geandier et al., 2003) during the succeeding years. In recent years, Elaguine et al. (2006) performed experimental investigation of a frictional contact cycle between a steel spherical indenter and flat float glass. And this has further been studied for different geometries and contacting materials by Jelagin and Larsson (2007).

Although Hertzian contact has been widely studied, other forms of crack are also available under different circumstances. Cook and Pharr (1990) summarized the general crack types generated in the surface of glass by indentation contact: cone, radial, median, half-penny and lateral.

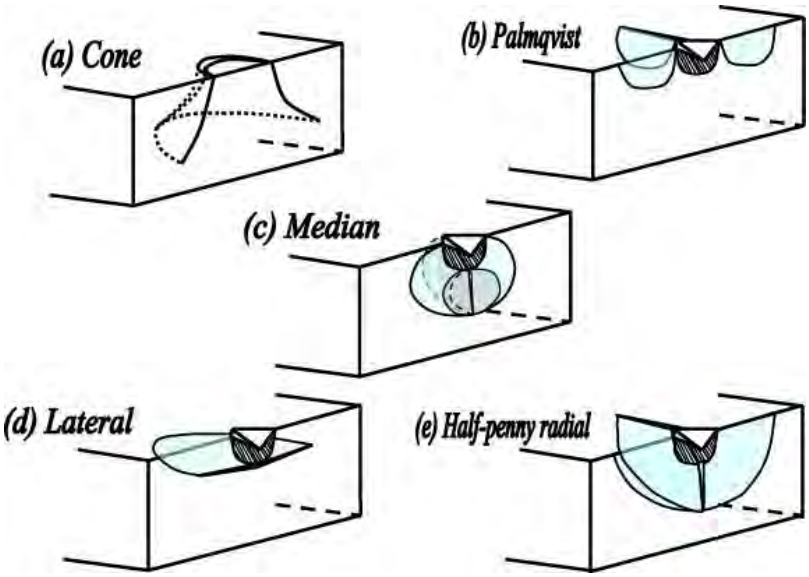

Figure 2.6 General types of crack subject to indentation (after Chen (2012))

In the review by Cook and Pharr (1990), both blunt and sharp indenters were used in the experimental test and the whole process, from loading to unloading was observed and recorded with the aid of high-speed camera and optical techniques. Peak load of 40N has been used in their study while behaviour under higher peak loads has been studied by other researchers (Lawn and Swain, 1975; Lawn et al., 1980) The crack types (near-cone and median vent cracks) subject to indentation were also discussed and concluded in some further research (Komvopoulos, 1996; Gorham and Salman, 1999; Park et al., 2002) with a variety range of loads.

Although glasses are commonly tested using the Hertzian indentation or Vickers indentation method (Fisher-Cripps, 2007; Le Bourhis, 2008), the disadvantages of these conventional methods are obvious: Hertzian indentations are difficult to realize in a normal laboratory

(Bisrat and Roberts, 2000). There is evidence (Quinn and Bradt, 2007; Kruzic et al., 2009) showing that indentation fracture methods are not appropriate for the measurement of any basic fracture resistance. Static or quasi-static indentation cannot reflect the real dynamic response and such local damage cannot control a real carrying capacity of the material (Gogotsi and Mudrik, 2010).

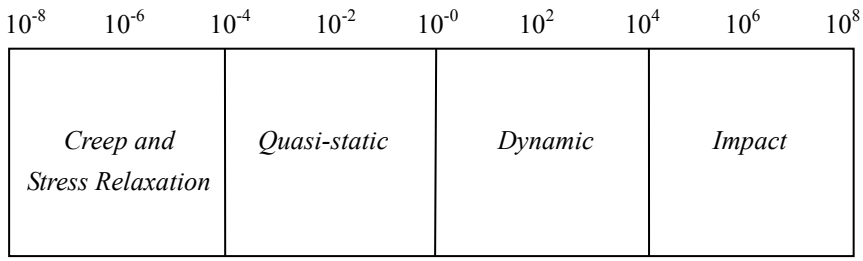

Figure 2.7 Strain-rate regimes according to loading rate (s^{-1})

According to Field et al. (2004), a range of strain rates span 16 orders of magnitude from creep to impact (Figure 2.7). Early in the 19th century, people were increasingly aware that material properties and behaviour of specimen under impact differs greatly from those under static or quasi-static loading (Young, 1807; Hopkinson, 1872). As a solution, series of impact tests were conducted throughout the last few decades.

Ball (or sphere) impact tests have been widely investigated (Andrews, 1931; Tillet, 1956; Tsai and Kolsky, 1967). Knight et al (1977) studied the impact of small steel spheres on soda-lime glass surface under the velocities varying from 20 to 300 m/s. During the loading and unloading cycle, a number of failure patterns (cone, median, radial and lateral cracking) were

obtained and discussed. Ball and McKenzie (1994) performed low velocity (ranging from10 to 50m/s) steel ball impact tests on circular annealed glass plate with thickness between 3 and 12mm. Grant et al. (1998) experimental studied 4 types of impact damage subject to low velocity impact, calling (a) surface crushing; (b) star cracking; (c) cone cracking and (d) combined damage. Salman and Gorham (2000) investigated the fracture behaviour of soda-lime glass spheres in the diameter range of 0.4-12.7mm and concluded that at lower velocities, Hertzian ring and cone crack system will be typical while higher impact velocities lead to fragmentation arising from radial, lateral and median cracks. However, no clear boundary between low and high velocities was given in their research. Recent observation (Chai et al., 2009) used sharp and spherical tip projectiles investigating the crack propagation in layered glass and chipping phenomena.

Besides the drop impact test, launching missiles to glass specimen is also a common method to investigate its mechanical behaviour. Most early laboratory work was performed on monolithic glass subject to small hard missile impact. Glathart and Preston (1968) observed two major damage modes for monolithic glass plate in their research: (1) Hertian cones will appear on the upper surface outside the contact zone if the thickness of the plate is large; (2) Glass breaks on the lower surface underneath the contact centre if the thickness of the plate becomes small. This demonstrated that the propagation of the cone crack depends largely on enough dimension along the thickness, otherwise local bending damage will be dominant. Minor et al. (1978) also reported small missile impact tests for monolithic glass panels. The

influence of glass thickness and type was studied for various geometries and projectile masses. Their study found that toughened glass shows higher resistance to impact than annealed glass due to higher residual stresses, which has been supported by Varner et al. (1980) in their experimental work.

The behaviour of laminated glass subjected to small missile impact at low velocity (10m/s) was investigated by Flocker and Dharani (1997a). Results showed that Hertzian cone crack was the primary concern in these cases. As the impact velocity increases to 30-40m/s, fractures will occur in both outer and inner glass plies (Behr and Kremer, 1996). The main difference of fracture patterns between monolithic and laminated glass is that laminated glass can hold the inner glass layer while monolithic cannot.

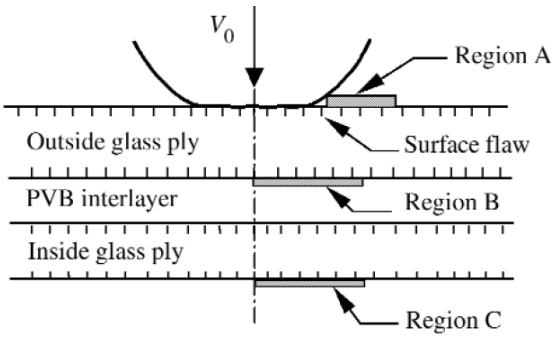

Figure 2.8 The three possible crack initiation regions (after Dharani et al. (2005))

For soft impact, failure modes depend on the flexural stress and crack initiations are mainly situated at three possible regions A, B and C defined by Dharani et al. (2005). Region A: outside of the contact area; Region B: close to the centre of the interface between the impact

side glass panel and the interlayer; Region C: the centre of the external surface of the non-impact side glass panel (Figure 2.8). Dharani and Yu (2004) conducted global-local stress analysis and illustrated that the shape of the contact surface will influence the failure mode. For spherical contact surface, crack initiates from Region B while it will start from Region C for flat ones.

Returning to the early 20th century, Hopkinson (1914) invented a ballistic pendulum method to determine the pulse response caused by impact of bullets or detonation of explosives at one end of a long rod. This device as well as its variations is called the Hopkinson pressure bar. Later, researchers (Taylor, 1946; Kolsky, 1949) perceived the idea of using two Hopkinson pressure bars to measure the dynamic response of specimen in compression, which is called the split Hopkinson pressure bar (SHPB). The original SHPB was schematically shown in Figure 2.9.

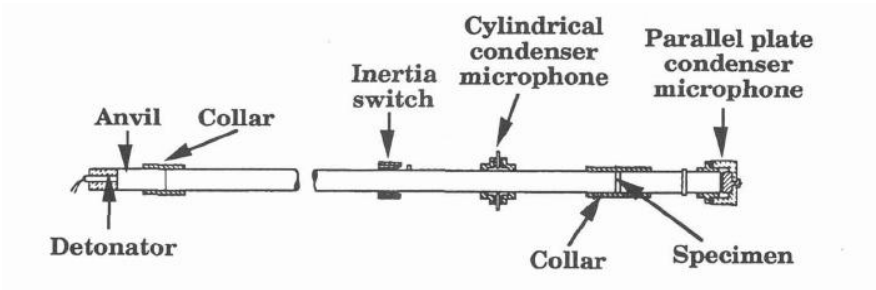

Figure 2.9 Schematic diagram of original the split Hopkinson pressure bar (SHPB) (After Kolsky (1949))

More details on this testing method can be found in many research works (Lindholm, 1964; LeBlanc and Lassila, 1993; Field et al., 1994, 2004). As an application, Bouzid et al. (2001)

verified their fracture model using the SHPB test and observed the fracture patterns under high strain rate.

Since the drop ball test is constrained by the height of dropping distance, there is a limit for the impact velocity that can be reached under normal laboratory conditions. For 5m dropping distance, the impact velocity is 9.9m/s and for 10m, this value will be 14m/s. For the split Hopkinson pressure bar (SHPB) test, higher impact velocity can be achieved as it does not depend on the height limit of the laboratory. Thus the drop ball test is suitable for low impact velocity simulation while missile or SHPB is more applicable to higher impact velocities. In the author's research on lower impact velocity simulation, usually a blunt spherical surface was employed to contact the glass, which is relevant to the drop ball test. For higher impact velocity simulation, SHPB can provide some good experimental data to compare with.

In this thesis, the drop ball test will be used for validation. The SHPB test can also be simulated using the FEM/DEM, however, since no experimental data is readily available to the author, this simulation have not been performed in the thesis.

2.5 Numerical Simulations

The advantage of experimentation is apparent: direct and real data. However, it also has some disadvantages. Carrying out experimental tests are usually time consuming and expensive. It

is not easy to control and most impact test needs the support of optical techniques such as high speed photogrammetry. Due to some initial errors, response of specimen may be unrepeatable and subject to random errors which make prediction difficult. With the modern development of computer hardware and software, numerical simulation becomes more and more prevalent in today's research.

In this section, the numerical methods that are used to investigate the response of glass will be reviewed, including the finite element method (FEM), discrete element method (DEM) and the combined finite-discrete element method (FEM/DEM).

2.5.1 FEM

The finite element method (FEM) was named in the work of Clough (1960) when he was in the Boeing Summer Faculty Program. After that, the methodology of FEM developed rapidly and major developments have been illustrated in later reviews (Clough, 1979; Zienkiewicz and Taylor, 1967; Zienkiewicz, 1995). With its development, modern technology, such as mesh-adaptivity, was combined into the FEM and fracture models were investigated by many researchers (Carranza et al., 1997; Khoei et al., 2012; Schrefler et al., 2006). Although FEM has been widely used in computational analysis of fracture mechanics, modelling of discrete crack configurations as well as their growth is laborious. Moving discontinuity needs the update of mesh to match the newly created geometry surfaces as crack growth can only occur

along the boundary of elements. Moreover, singularity at the crack tip needs accurate representation by the approximation (Tong and Pian, 1973). Methods for effective crack solving were not proposed until late 1990s.

Several new FEM based techniques were developed to model cracks and crack growth, including those proposed by Oliver (1995), Rashid (1998) etc. Belytschko and Black (1999) introduced a new procedure for resolving cracks. In their method, remeshing is minimized by refining the elements near crack tips and along the crack surfaces, and the partition of unity (PU) method (Melenk and Babuska, 1996) was employed to account for the presence of the cracks. Soon after, Moes et al. (1999) published a much more straightforward technique. In their research, discontinuous fields and the near tip asymptotic fields were incorporated into a standard displacement-based approximation, allowing independent representation of the entire crack away from mesh. This extended displacement interpolation was given in equation 2.3, with addition of Heaviside enrichment term $H(x)a_I$ and crack tip enrichment term $\sum_{\alpha=1}^{4} F_\alpha(x)\, b_I^\alpha$ to the conventional FE shape function u_I.

$$u^h(x) = \sum_{I \in N} N_I(x) \left[u_I + H(x)\, a_I + \sum_{\alpha=1}^{4} F_\alpha(x)\, b_I^\alpha \right] \tag{2.3}$$

Later, Daux et al. (2000) introduced the concept of junction function to enable the representation of branch cracks and named their method the extended finite element method

(XFEM). Using XFEM, Sukumar et al. (2000) investigated mode I cracks in three dimensions. Dolbow et al. (2000) studied the fracture behaviour of Mindlin plates and 2D crack growth with frictional contact (Dolbow et al. 2001). Xu et al. (2010) analysed the windshield cracking subject to low-velocity head impact based the XFEM and both radial and circumferential cracks were characterized.

Based on the implementation found in ABAQUS, XFEM does not require mesh to match the geometry of the discontinuities (Figure 2.10) and remeshing is not necessary in simulating crack initiation and propagation. However, this elegant method still has its limitations. Apart from limited element types (currently only linear continuum elements can be used), interacting cracks (shattering, branches) cannot be modelled (SIMULIA, 2011). Also, one element cannot be traversed by more than one crack and crack cannot turn more than 90 degrees in one increment (SIMULIA, 2011).

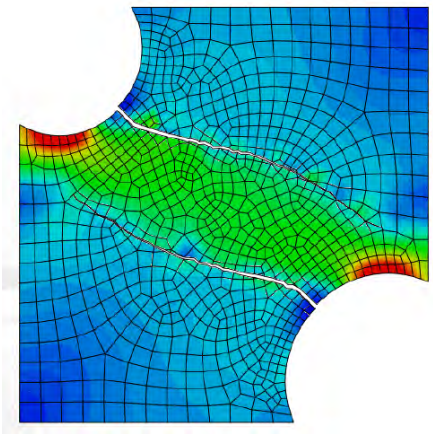

Figure 2.10 Crack onset and propagation independent of mesh in XFEM (after SIMULIA (2011))

Almost at the same time, another approach called the generalized finite element method (GFEM) was introduced by Strouboulis et al. (2000a, 2000b, 2001) and Duarte (2000). This method embedded analytically developed or numerically computed handbook functions into classical FEM estimate to improve the local and the global accuracy of the solution. According to Karihaloo and Xiao (2003), the p-adaptivity is considered in GFEM and accurate numerical simulations with practically acceptable meshes can be provided by enlarging the FE space with analytical or numerically calculated solution of a given boundary value problem (BVP). However, on the other hand, XFEM pays more attention to the creation of nodes to model the new surface boundary, making it solution-dependent and enjoy more flexibility.

There is a lot work on the fracture and crack modelling using the FEM. Setoodeh et al. (2009) performed low velocity impact analysis on laminated composite plates, with 3D elastic theory coupled with layerwise FEM approach. Liu and Zheng (2010) reviewed the recent development on composite laminates damage modelling using finite element analysis (FEA). Barkai et al. (2012) calculated the crack path in brittle material using quasi-static FEA.

For numerical simulation of glass and laminated glass fracture, usually appropriate failure models were incorporated into the FEM package, such as the continuum damage mechanics (CDM) model (Sun et al., 2005; Zhao et. al., 2006), the fracture mechanics approach (Dharani

and Yu, 2004), and the two-parameter Weibull distribution (Dharani et al., 2005). Pyttel et al. (2011) also recently presented a fracture criterion for laminated glass and implemented it into an explicit finite element solver. The crack initiation is based on the critical energy threshold while propagation is related to "local Rankine" (maximum stress). The FEM have been applied in predicting cracks and crack growth with reasonable accuracy, however, they are still subjected to restrictions of the FEM itself. One of the disadvantages is that post-damage discrete fragments and movement of them are difficult to be simulated by FEM, which is a major concern in glass design industry.

An alternative option of performing crack simulation by the FEM is the smeared crack approach and will be discussed later in chapter 4.

2.5.2 DEM and FEM/DEM

The discrete element method (DEM) is a method proposed for discontinuous analysis. The method was pioneered by Cundall and Strack (1979) for the study of the behaviour of 2D soil slope stability problems. Newton's second law of motion was employed and kinetic equations were built in the discrete element method. Some discrete elements were assumed to be rigid, represented by the rigid-body-spring model of Kawai (Kawai, 1977; Kawai et al., 1978), while deformable 2D and 3D discrete elements were available from the research of Hocking et al. (1985) and Mustoe (1992). Most discrete elements are of the shape of circles in 2D and

spheres in 3D, which are convenient for analysing collapse as these shapes have been widely used in granular analysis (Cundall and Hart, 1992; Griffiths and Mustoe, 2001; Robertas et al., 2004; Scholtes and Donze, 2012). Other element type such as hybrid Kirchhoff element was used according to Hocking (1992), which has been applied for simulating the fragmentation of ice sheet - conical off shore structure interaction (Figure 2.11). Similarly, cube or block elements were also used in modelling collapsing of discontinuous columns in recent research (Jin et al., 2011).

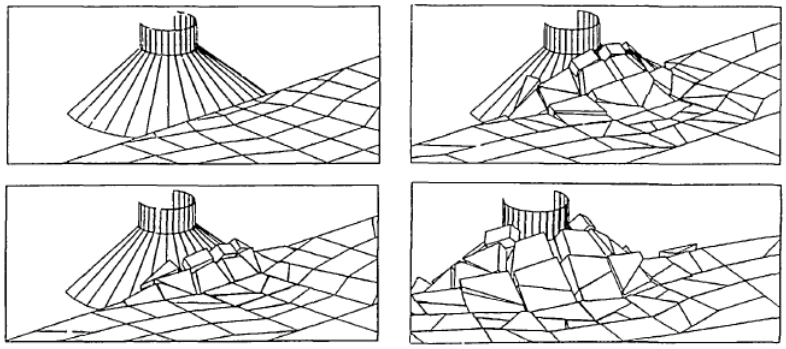

Figure 2.11 DEM simulation of a floating ice sheet impacting a conical structure (after Hocking (1992))

Owen and his group (Klerck et al., 2004; Owen et al., 2004; Pine et al., 2007) developed some crack models based on the discrete element method. Klerck et al. (2004) and Pine et al. (2007) simulated the fracture in quasi-brittle materials, such as rock. Their models were based on a Mohr-Coulomb failure surface in compression and three independent anisotropic rotating crack models in tension. In Owen et al. (2004), a model for multi-fracturing solids was presented and a combination of both continuous and discrete media was considered. It should

be noted that “discrete/finite element combination” in their text is not the same idea of the combined finite-discrete element method which will be discussed shortly and be used throughout this thesis. Instead, the terminology represents for the discrete and continuous media and a coupled dynamic interaction between them was considered in the research.

The same idea of the above-mentioned FEM-DEM coupling was also used in the Livermore distinct element code (LDEC), which was originally developed by Morris et al. (2003). In Morris et al. (2006), the code was used to simulate the fracture and fragmentation of geologic materials, like rocks (Figure 2.12).

(a) t = 0ms (b) t = 200ms

Figure 2.12 A tunnel collapse simulation by using the LDEC (after Morris et al. (2006))

The DEM simulation of glass subject to impact is rare. Oda et al. (1995) employed the DEM to simulate the impact behaviour of laminated glass. Later, they extended their research to bi-layer type of glass (Oda and Zang, 1998). Impact behaviour of both single and laminated

glass subject to ball impact was studied by Zang et al. (2007), and penetration as well as the following fragmentation was simulated. Results within the elastic limit were compared with the data generated from FEM code LS-DYNA and good agreement was achieved. In spite of fewer element layers, acceptable fragmentations were predicted. However, in their research, both glass and PVB elements are of circle shapes, which resulted in non-realistic fracture patterns (Figure 2.13).

(a) single glass (b) laminated glass

Figure 2.13 DEM simulation of the fracture of monolithic and laminated glass (after Zang et al. (2007))

According to Jin et al. (2011), although DEM can predict the fragments and fragmentations after damage, this method requires quite a large number of elements, if reasonable results are desired, plus a very small time step. Smaller time step further requires more time steps to complete an analysis for a given time duration and resulted in longer computation time, which can be quite expensive in terms of CPU time. Since the FEM/DEM inherits all the merits of ordinary DEM and can produce a more accurate estimate of the contact force and deformation as finite elements were embedded in, more attention should be paid to its development and application in glass fracture problems.

The combined finite–discrete element method (FEM/DEM), which belongs to the discipline of computational mechanics of discontinua, is a newly developed numerical method aims at investigating failure, fracture and fragmentation in solids. The method was pioneered by Munjiza (Munjiza et al., 1995) during 1990s. According to the definition (Munjiza et al., 2004), the major difference to DEM is that finite element discretization is used to discretize the contacting domains, thus discretized contact solutions (Munjiza et al, 1997) are used for both contact detection and contact interaction. As finite element formulation is introduced into the discrete elements so that the estimate and prediction of structural response can be more accurate. Meanwhile, penalty function was used to better control the contact force, inter-penetration and fracture behaviour (Munjiza and Andrews, 2000).

Munjiza et al. (1995) discussed the issues involved in the FEM/DEM from a theoretical point of view and related algorithmic considerations. Later, Munjiza and Andrews (1998) proposed a No Binary Search (NBS) method for contact detection, which greatly improved the performance of CPU efficiency and RAM requirement. The fracture model in the FEM/DEM, which is a combined single and smeared crack model, was discussed by Munjiza et al. (1999). However, the model was limited to Mode I loading cracks of concrete and a relatively fine mesh is required to obtain accurate fracture patterns. Details on the influence of mesh size was presented by Munjiza and John (2002), giving the approximate length of plastic zone Δ so that reasonable size of elements can be meshed around the crack tip, making the stress

representation more accurate within that zone.

The basis of the FEM/DEM was published by Munjiza (2004, 2008) in his textbooks and papers. He named the accompanying demonstration program Y. Although the element types in Y-code is restricted to three-noded triangle subjecting plane stress condition in 2D, a two-noded thin beam element (Bangash and Munjiza, 2003) was included for the investigation of the failure and collapse of concrete beams. Results obtained compare well with analytical and experimental data. Similar validation on beam element was also carried out by (Munjiza et al., 2004), and validation on the sliding friction was address by Xiang et al. (2009).

Although there are some applications of the FEM/DEM in geologic engineering and molecular dynamics, most of them are on the fracture behaviour of concrete and rock (Lisjak and Grasselli, 2010) and individual collision and movement of molecules (Rougier et al., 2004). Furthermore, the current FEM/DEM program costs considerable time to execute. Regarding the performance, Wang et al. (2004) analysed the parallel computation of the FEM/DEM on PC clusters by adopting a dual-level decomposition scheme and achieved a good speed-up ratio. MPI strategy for 2D FEM/DEM program was also being carried out by Lukas and Munjiza (2010).

2.6 Summary

This chapter reviewed the literature on the fracture of glass. Studies on this topic are numerous and only some representative ones were selected and discussed. The introduction and application sections gave an overview on the fracture of glass through the history and in other areas besides civil engineering: forensic (McJunkins and Thornton, 1973), aeronautics (Cour-Palais, 1987) and automobile industry (Timmel et al., 2007). As was mentioned in section 2.2, different domains have different emphasis and glass is more and more serving a structural role in civil engineering. In such a case, behaviour of glass under blast, impact, wind and other hostile effect has to be considered.

As fracture and fragmentation always occur with these dynamic loading (blast, impact and wind), the energy balance approach that developed by Griffith (1920) is a good starting point to evaluate the relationship between the absorbed energy and intrinsic property of material. Irwin (1957) developed Griffith's approach. However, both methods introduced stress singularity. Hillerborg's model (Hillerborg et al., 1976) solved this problem and predicted the stress around the crack tip. Although theoretical fracture mechanics is still developing, the major frames for brittle material are approaching completion. Fracture mechanics is not the direct tool but more like a bridge in the analysis of the fracture of glass.

On the experimental side, many researchers still prefer the indentation or impact tests, which

are direct but not easy to perform. Optical technique is usually indispensible in such observation and high-speed camera is used to capture the transient images of the damage. Cook and Pharr (1990) observed some general crack types in the surface of glass by indentation. Genuine impact tests can also been found throughout the history (Andrews, 1931; Tsai and Kolsky, 1967; Knight et al., 1977; Ball and McKenzie, 1994; Chai et al., 2009).

Numerical investigation became popular with the development of computer hardware and software. In this domain, FEM and DEM are two distinct branches with different emphasis on the problem. FEM is more appropriate and accurate for the calculation of the critical fracture state while DEM is particularly excelled in simulating the fragments and fragmentation. In this review, more attention was paid to the XFEM (Moes et al., 1999) and FEM/DEM (Munjiza et al., 1995). Although numerical methods for crack onset and propagation have developed over the last two decades, not much has been done on the modelling on glass and it is even rarer for the FEM/DEM (Chen et al, 2010, 2012).

The literature review of this chapter was concerned about the methods and development in analysis of glass fracture mechanics. Apart from the introduction and application section, theoretical, experimental and numerical endeavours on this topic were presented. Detailed results on the fracture of glass and numerical models used for simulation will be reviewed and discussed separately in appropriate following chapters.

The current knowledge gap is that the available model on glass is not as mature as that for concrete, which comes from considerable tests and experiments. This requires better numerical modelling. Also, from the method level, traditional finite element method has difficulties in simulating fragments as well as their movement after damage. Since the post-damage behaviour is important in glass fracture analysis as people may get injured from the flying shards, the FEM/DEM was used in this research.

METHODOLOGY

3.1 Introduction

In this chapter, the FEM/DEM method and related computer programs being used in the research are discussed in details. When glass is subjected to impact, fracturing and fragmentation are inevitable if the impact force is large enough. Since this will result in a discontinua problem, traditional FEM is not adequate to describe the behaviour. The analysis of discontinua problems requires discontinua method. Though recent development in XFEM can deal with the fracture problem to some extent (see section 2.4.1), limitations in post-damage simulation make it inadequate for the research of glass fracture analysis where fragmentation is important.

In this research, the combined finite-discrete element method (FEM/DEM) is adopted as it is capable of handling a discontinua problem more effectively. In section 3.2, some key aspects of FEM/DEM are highlighted, including the evaluation of contact force, discrete elements and the joint elements. The FEM/DEM program Y provided by Professor Munjiza (Queen Mary, University of London) is the research tool used for the analysis of glass failure, fracture and fragmentation in this project and is discussed in section 3.3. The FEM/DEM program is a research program and both pre and post-processing are performed by commercial or open-source programs, such as ABAQUS CAE (SIMULIA, 2004), M (Munjiza, 2000) and

LS-Pre/Post (LSTC, 2004). In section 3.4, these are briefly covered. At the end of this chapter, a summary is made, giving an overall view of the methodology used in the project.

3.2 FEM/DEM

The FEM/DEM, which is short for the combined finite-discrete element method, is a novel numerical method aims at the solution of mechanics problems for solids which are considered as a combination of both continua and discontinua. In such a combined numerical simulation, the deformability of particles is described using continua formulation (FEM) while the motion and interaction between particles is well considered in discontinua format (DEM).

It can be understood that DEM is governing the motion by Newton's second law and interaction from contact force in a more macroscopic and general level while FEM is responsible for the stress and deformation of individual discrete elements.

For the DEM, translational and rotational motions of each discrete element *i* are controlled by net external force f_i and torque t_i separately:

$$m_i \frac{d^2}{dt^2} r_i = f_i \tag{3.1a}$$

$$I_i \frac{d}{dt} \omega_i = t_i \tag{3.1b}$$

where m_i is the mass of discrete element *i*, r_i is the position. I_i is the moment of inertia

and ω_i the angular velocity. Explicit numerical integration determines the velocity and position of a particular discrete element.

The deformation of the discrete element in FEM/DEM has to obey the standard FEM definition, which can be found in many comprehensive review literatures (e.g. Clough, 1979; Zienkiewicz, 1995). The FEM/DEM merged the finite element method and discrete element method together, achieving the most advanced approach available so far for systems comprising large number of deformable discrete elements simultaneously fracture and fragment.

In this section, the contact force in the FEM/DEM will be introduced. Forces between two discrete elements in contact will be evaluated by the gradients of their potentials over the overlapping area. The FEM also has contribution to it. The discrete element and currently available element types in FEM/DEM will be discussed after the introduction of contact force. Finally, the joint element, which is a set of dummy elements that control the transition from continua to discontinua will be described and discussed. Fracture criterion used in the FEM/DEM will be discussed in chapter 4.

3.2.1 The Evaluation of the Contact Force

The FEM/DEM aims at solving problems of transient dynamics involving a large number of

deformable discrete bodies that interact with each other. Each individual discrete body is modelled by several single discrete elements. Each discrete element is meshed by one or more finite elements in order to analyse the contact force and deformation.

Following the theoretical approach given in Munjiza (2004), the distributed contact force is adopted for two discrete elements in contact, one of which is denoted as the contactor and the other as the target (Figure 3.1).

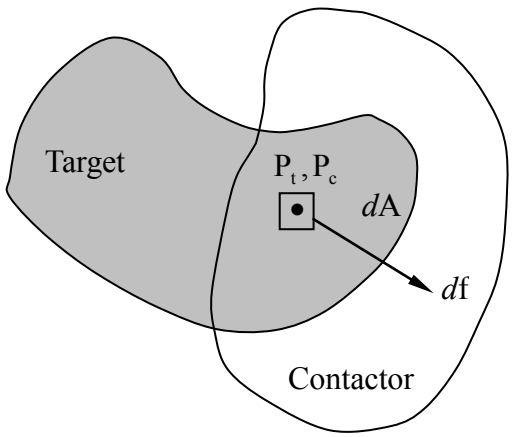

Figure 3.1 Contact force due to an infinitesimal overlap around points P_c and P_t

In 2D, the penetration of any elemental area dA of the contactor into the target results in an infinitesimal contact force $d\mathrm{f}_\mathrm{t}$, which can be given by equation (3.1):

$$d\mathrm{f}_\mathrm{t} = -E_p \, grad \, \varphi_t(\mathrm{P}_t) \, dA \tag{3.2a}$$

Meanwhile, similarly, an infinitesimal force of the target penetrating the contactor can be obtained:

$$d\mathrm{f}_\mathrm{c} = E_p \, grad \, \varphi_c(\mathrm{P}_c) \, dA \tag{3.2b}$$

where the point P_c belongs to the contactor and P_t belongs to target (Figure 3.1). *grad* represents for the gradient. φ_c and φ_t are potentials on the contactor and target, respectively. And E_p is the contact penalty parameter that equals p_1 which will be introduced in chapter 4. So the total infinitesimal contact force can be given by equation (3.3):

$$d\,\mathrm{f} = E_p\,[grad\,\varphi_c(\mathrm{P}_c) - grad\,\varphi_t(\mathrm{P}_t)]dA \tag{3.3}$$

Denoting *S* the area that contactor and target discrete elements overlap with each other, the total contact force can be obtained by integrating equation (3.3) over the overlapping area *S*, yielding the expression of contact force f_c in equation (3.4).

$$\mathrm{f} = E_p \int_S [grad\varphi_c - grad\varphi_t]\,dA \tag{3.4}$$

According to Munjiza et al. (2011), there are a number of ways to define the force potential φ over the contactor triangle but the following requirements should be satisfied for 2D linear triangular element: the potential should be constant on the boundary of the discrete element. Thus, the potential at point P inside the triangular element can be defined in equation (3.5) so that the constraint can be unconditionally met.

$$\varphi(P) = \min\{3A_1 / A, 3A_2 / A, 3A_3 / A\} \tag{3.5}$$

where A_1, A_2, A_3 are the sub-triangles shown in Figure 3.2. So that the potential of any point on or outside of the edge will be zero, and the potential at the centre of the triangle reaches the maximum 1.

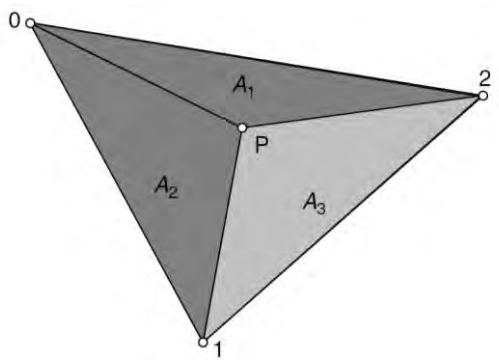

Figure 3.2 The potential at any point of a linear trianglualr element (after Munjiza (2004))

In the FEM/DEM program and Munjiza et al. (2011), the contact force is given by

$$\mathrm{f} = E_p \varphi\left(P_G\right) S \tag{3.6}$$

where $\varphi\left(P_G\right)$ is the potential of Gauss point expressed in Equation 3.5 and S is the interacting area mentioned above. And this is the formula used in the FEM/DEM code.

In 3D, the total contact force due to the overlapping volume V can be derived as in equation (3.7) and the potential of the tetrahedron can be defined in a similar approach as equation 3.5 did.

$$\mathrm{f} = E_p \int_V [grad\varphi_c - grad\varphi_t]\, dV \tag{3.7}$$

Thus the contact force in the FEM/DEM can be expressed in terms of the deformation (FEM contribute to it) and motion of the FEM/DEM elements in contact. The details on the

FEM/DEM element will be discussed in the following section.

3.2.2 The Discrete Element

In essence, FEM/DEM is a discrete element method. However, the implementation of FEM within each discrete element makes it different from ordinary DEM. With one or more finite elements implemented in, the discrete elements are able to deform. The stress field within each discrete element also can be better represented by the finite element method. Theoretically, FEM/DEM element can be of any shape, like rectangles (2D) or hexahedral cubes (3D) which are commonly used in finite element analysis. For simplicity, only the 3-node constant strain triangle is employed for 2D problems and the 4-node constant strain tetrahedron element is applied in 3D. These two element types are the only two available types of element in the current FEM/DEM program Y.

Structures, or entities, need to be meshed with discrete elements before carrying out numerical simulation. In the current study, each individual discrete element is only meshed by one finite element for the analysis of deformability, fracture and fragmentation. The discrete element in FEM/DEM is a combination of both discrete and finite element.

Although the implemented types of elements are of the simplest in shape, these elements can be applied to any conceivable boundary with complex curvature as is shown in Fig 3.3. In

addition, despite their constant strain property, satisfactory results can still be achieved by increasing the numbers of elements in desired domain.

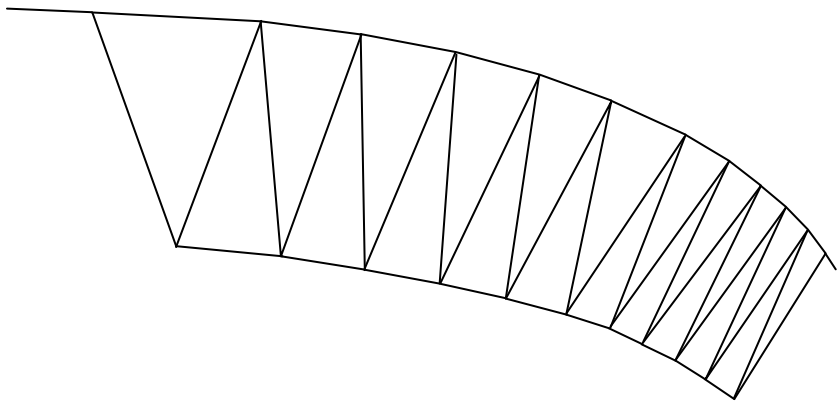

Figure 3.3 Use triangular elements to approximate curved boundary

The advantage of using the simplest type of element is obvious. It can improve the CPU time and the overall efficiency for contact algorithm (Munjiza, 2004) although the current computational time is quite considerable. Also, the generalised triangles and tetrahedrons can be used to configure complex curvature. However, using only constant strain elements in analysis may require more elements in some stress concentrated area and increase the total number of elements, which may reduce the efficiency (in 2D, one quadrilateral contains two triangles while in 3D one parallelepiped may contain five or six tetrahedrons). Further, this may also lead to some element-generated bias towards results.

3.2.3 The Joint Element

The concept of joint element is included in the FEM/DEM to capture and determine the transition from continua to discontinua. These joint elements, which are dummy elements in essence with zero thickness, exist between any adjacent pair of finite-discrete elements. Thus, the fracture criterion is linked to the deformation of joint elements.

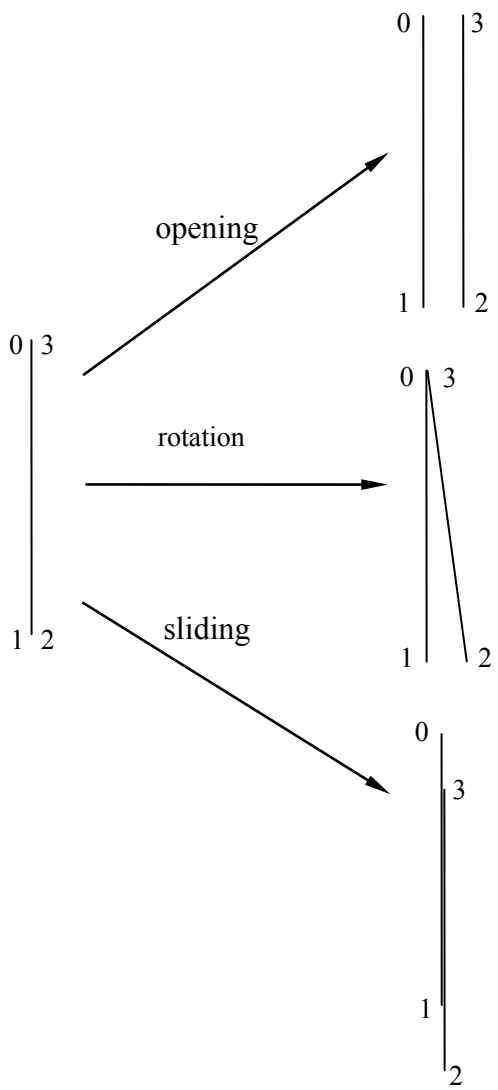

Figure 3.4 The opening and sliding deformation of a joint element

Geometrically, each joint element is a pair of lines or triangles in 2D or 3D respectively. Figure 3.4 illustrated the three kinds of deformation (opening, sliding and rotation) that may happen to a 2D joint element. However, in the FEM/DEM, fracture is considered on a point basis, where rotation does not apply and only opening and sliding be used. We use o for opening and s for sliding. The damage index d used in this work is a function of both o and s: $d = d\ (o,\ s)$. Should we assume no deformation at the initial stage, these two lines (in 2D) or triangles (in 3D) should coincide exactly with each other, which means that there is no separation between the finite-discrete element couple. With the development under the influence of external forces or other actions, the separation may increase and the joint element deforms correspondingly. Before the deformation of joint element reach certain value $d_e(o,\ s)$, we consider the finite-discrete element pair is within the elastic limit. The point of elastic limit is also the start of damage. After that, the finite-discrete element pair will experience strain-softening period (see Figure 4.4, section 4.3), leading to increase in damage. Once the separation reaches certain critical value $d_t(o,\ s)$, the joint element should be considered completely damaged and be removed from the existing list of joint elements, making it not to participate in the following computation of fracture evaluation. Meanwhile, the corresponding finite-discrete element pair will be disassociated. By investigating the deformation of joint elements, the damage status between two adjacent finite-discrete elements can be determined.

As was shown in Figure 3.4, for each 2D joint element, there are four nodes 0, 1, 2, 3, with their coordinates (x_0, y_0), (x_1, y_1), (x_2, y_2), (x_3, y_3). To evaluate the deformation of the

joint elements, *o* and *s* need to be determined. Without loss of generality, we consider the deformed joint element as shown in Figure 3.5.

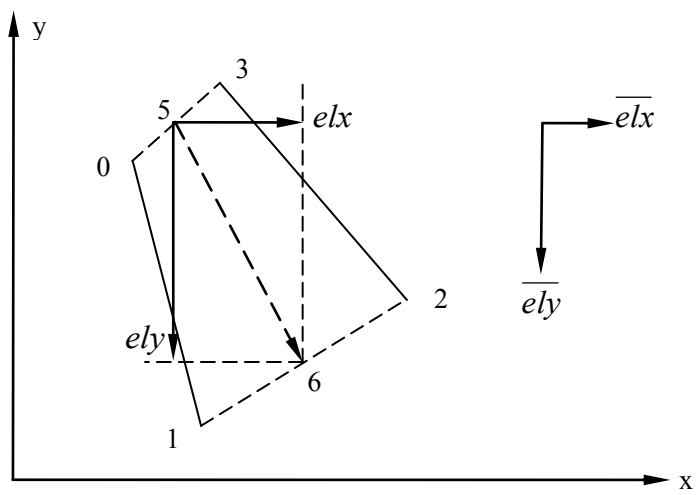

Figure 3.5 The deformation of joint element

Take the middle vector $\overline{56}$ between $\overline{01}$ and $\overline{32}$, the components of $\overline{56}$ in both *x* and *y* direction can be obtained (Munjiza, 2000):

$$elx = \frac{1}{2}\left(x_1 + x_2 - x_0 - x_3\right) \tag{3.8a}$$

$$ely = \frac{1}{2}\left(y_1 + y_2 - y_0 - y_3\right) \tag{3.8b}$$

Also, the length *h* of vector $\overline{56}$ can be expressed as:

$$h = \sqrt{elx^2 + ely^2} \tag{3.9}$$

Take $\overline{elx} = \frac{elx}{h}$ and $\overline{ely} = \frac{ely}{h}$, then $\left(\overline{elx}, \overline{ely}\right)$ is the normalized unit vector of $\overline{56}$.

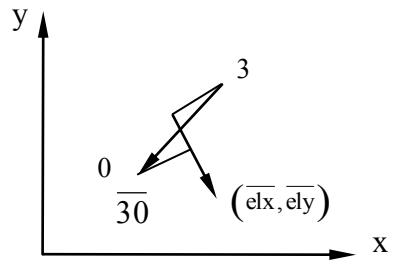

Figure 3.6 The projection of vector $\overline{30}$ onto normalized vector of $\overline{56}$

According to the definition of dot and cross product, the opening $o1$ and sliding $s1$ between points 0 and 3 can be given in equation (3.10) as the projection of vector $\overline{30}$ onto $\left(\overline{elx}, \overline{ely}\right)$ as was shown in Figure 3.6.

$$o1 = \left| \left(x_0 - x_3, y_0 - y_3\right) \times \left(\overline{elx}, \overline{ely}\right) \right| \tag{3.10a}$$

$$s1 = \left(x_0 - x_3, y_0 - y_3\right) \cdot \left(\overline{elx}, \overline{ely}\right)^T \tag{3.10b}$$

Similarly expressions can be obtained for separation $o2$ and $s2$ between points 1 and 2. Thus, separations of other integration points can be determined by ($o1$, $s1$, $o2$, $s2$) according to the proportional relationship along the joint element.

(a) 3D triangle joint element after deformation

(b) The relative displacement (*rdis*) and normal vector (*vnor*) of the middle plane

Figure 3.7 The deformation of 3D joint element and the calculation of normal and sliding separation from the relative displacement

For 3D problems, the derivation can be extended similarly but with some differences. The joint element in 3D is a 6-node triangle plane. After deformation, a middle plane will be obtained as illustrated in Figure 3.7(a). The stresses are obtained on the integration-point-basis. Consider the relative displacement of certain integration point to be vector *rdis* (it is obtained based on the coordinates of the upper and lower surfaces of the joint element) and the normalised normal vector of the middle plane *vnor* (Figure 3.7(b)), the normal separation at the integration point of the triangle can be obtained using the definition of dot product in equation 3.11:

$$o = rdis \cdot vnor \tag{3.11}$$

The x, y and z components of sliding vector at this integration point are obtained by removing the normal separation in global coordinate direction in equation 3.12:

$$\begin{aligned} s_x &= rdis - o \cdot vnor_x \\ s_y &= rdis - o \cdot vnor_y \\ s_z &= rdis - o \cdot vnor_z \end{aligned} \tag{3.12}$$

So that the sliding distance for this point can be obtained from equation 3.13 and calculation from the middle plane can be avoided. And the shear stress is along the direction of *s*, obtained by mapping its value to the strain softening curve, which is not actually correct as the friction stress depends on the increment and history.

$$s = \sqrt{s_x^2 + s_y^2 + s_z^2} \tag{3.13}$$

By doing this, the deformation of joint elements can be represented by the opening *o* and sliding *s*, respectively. The normal and shear force are along the direction of *o* and *s*. The

limitation of this approach is that all the discrete elements will have to share the same critical separating distance regardless of their size.

3.3 FEM/DEM Program Y

The FEM/DEM program Y is designed for the purpose of demonstrating some of the concepts explained in the FEM/DEM book (Munjiza 2004). This program contains both the 2D and 3D elements and is the research tool being used in the project. It is devised and provided by Professor Munjiza (Queen Mary, University of London).

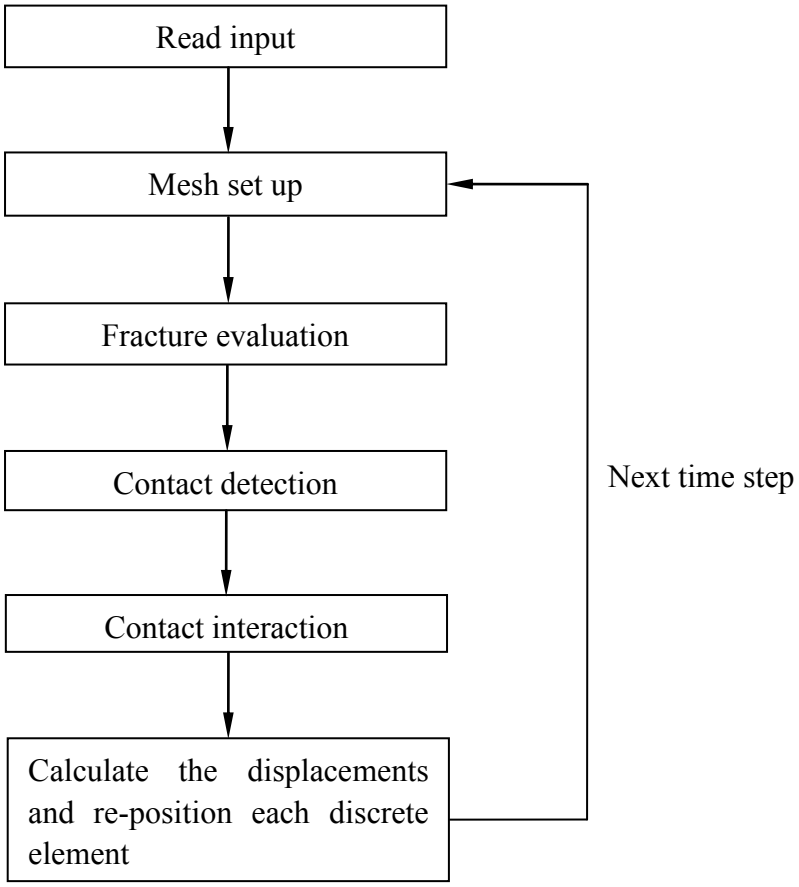

Figure 3.8 The working process of FEM/DEM program

In order to use the FEM/DEM program, users need to prepare an input file to describe the problem. The working process and flowing chart is schematically shown in Figure 3.8. After each time step, the relevant data need to be updated in the database. The database will be accessed every time step as new data are needed for the computation of the next time step. Since the method is explicit, the time step is much smaller than finite element method using implicit scheme. Thus considerable computational time is needed, making the FEM/DEM much slower than usual FEM package, which has been indicated as a 'Grand Challenge' by Munjiza (2004).

3.4 Pre and Post Processing

As was mentioned previously, the current FEM/DEM program is a research program and both pre and post-processing need external support. In this section, the software ABAQUS CAE, M and LS-Pre/Post will be discussed, demonstrating their use in the research. ABAQUS CAE is used to set up the model and generate the mesh, while M and LS-Pre/Post is for post-processing 2D and 3D output, respectively.

3.4.1 Pre-processing

The geometrical model and element mesh of any FEM/DEM problem can be created by any

available FEM pre-processing software. In this project, the ABAQUS CAE (SIMULIA, 2004), which is available within the university is used for this purpose.

Ideally, the numerical results will be most accurate if the structure is assigned with extremely fine mesh (atomic level). However, this large number of elements is not numerically affordable in practice. Generally, small elements will be used within the impact effective area where the stress variation is intense in order to reach an acceptable level of accuracy. Meshes close to the support may also need to be refined if significant reaction is expected. For the rest part of the structure, a relatively coarse mesh can be employed according to Saint-Venant's principle. Thus, analysis over the stress distribution after impact is necessary to get some idea that some part should be assigned with fine mesh while in other area, a coarse mesh will be adequate. Representative meshes for rectangular and circular plates subject to impact in the middle are shown in the Figure 3.9.

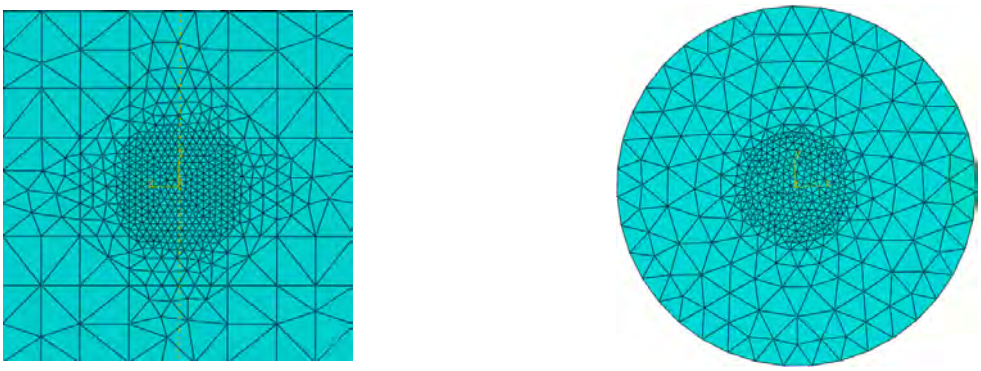

(a) Rectangular plate (b) Circular plate

Figure 3.9 Mesh strategies for plates subject to impact in the middle (view from top)

Besides allocating different size of meshes in the plane perpendicular to the impact direction, the mesh size along the thickness of target can also be evaluated according to different situations encountered. For thin glass beam or plate, a fine mesh can be employed within the impact effective zone throughout the thickness, while for large glass blocks, a coarse mesh can be used for those areas that are far from the impact point in depth (Figure 3.10). This is largely due to the stress wave propagation consideration and will be discussed in chapter 5 in details.

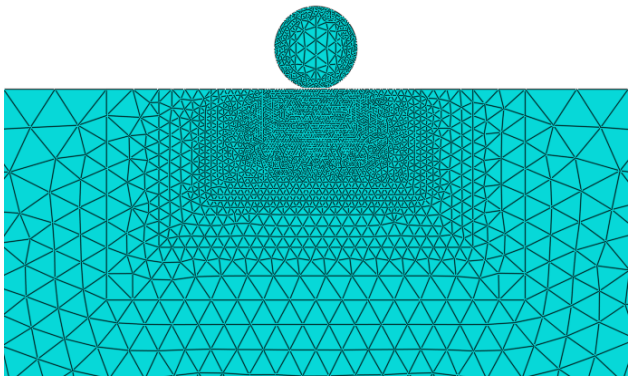

Figure 3.10 A mesh distribution for large glass block subject to impact

As was mentioned previously, apart from ABAQUS CAE, any mesh generator that can produce triangular or tetrahedral elements (such as FEMGEN) can be used in this project. The advantage of using ABAQUS CAE relates to the fact that it is an advanced, well established program with significant stability, and have little problem when generating mesh. The drawback of using a single pre-processor in the research is that mesh will be produced by its own strategy, which is favoured by ABAQUS FEM analysis, while it may not be most suitable for FEM/DEM analysis. Fortunately, one can expect that with the intervention of user,

this can be reduced to a minimum.

3.4.2 Post-processing

There are two programs for post-processing FEM/DEM output, M for 2D and LS-Pre/Post for 3D. M program is an accompanying program for plotting 2D output files generated by the FEM/DEM program. It is small and easy to use. The fracture pattern (Figure 3.11) can be plotted by M, as can be found in the following chapters. Besides the fracture patterns, the distribution of some simple field (stress, velocity) can also be plotted, but without value given on the graph. In general, M is more for demonstration than engineering analysis purpose.

Figure 3.11 The fracture pattern plotted using M program (Chen et al., 2012)

For 3D, LS-Pre/Post (LSTC, 2004) can be used as a post-processor. It is a product of Livermore Software Technology Corporation and is freely distributed. LS-Pre/Post is a balance between computer resources (about 30MB on hard drive) and plotting robustness. It is capable of reading the LS-DYNA binary output generated from the FEM/DEM program. Figure 3.12 showed the Von Mises stress while a bullet projectile penetrated the glass plate.

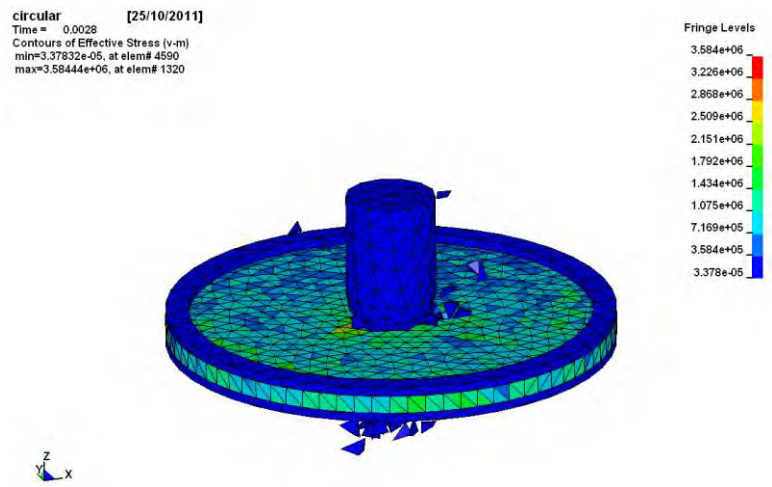

Figure 3.12 Ls-Pre/Post plotting of a bullet impact on a clamped glass plate

The LS-Pre/Post provided a good visualisation of the 3D results. However, it is not able to get the Linux version of LS-Pre/Post working on the university HPC (High Performance Computation) facility, thus limiting the application.

3.5 Summary

In this chapter, the FEM/DEM as well as the program being used in the research has been discussed.

For the FEM/DEM, key equations of DEM and essential information were introduced. Also, the contact force, discrete elements as well as the joint elements were briefly covered. More details can be found in the text book (Munjiza, 2004).

The FEM/DEM program Y as well as its working process was also introduced for better understanding. Further discussion can be referred to the user's manual (Munjiza, 2000).

To the pre and post-processing, ABAQUS CAE, M and LS-Pre/Post were discussed briefly. The physical model is pre-processed in ABAQUS CAE then transferred into the FEM/DEM format by using a special program developed by Chan (2010). Meanwhile, M and LS-Pre/Post are used for 2D and 3D plotting separately. Although these programs are the currently available and compatible ones to the FEM/DEM, one can still develop their preferred output format and make it be read by other post-processing programs. Thus many drawbacks, like the limitation of M in plotting can be resolved.

The FEM/DEM method makes the research theoretically applicable, while programs (both Y and pre/post-processors) enable the practical implementation. These aspects mentioned above are the foundations of this research.

MODE I FRACTURE MODEL OF GLASS

4.1 Introduction

The fracture model, which aims at modelling crack initiation and propagation by breaking the element connections in the combined finite-discrete element method (FEM/DEM), is the combined single and smeared crack model. In the current model, each discrete element contains a finite element. The fracture is realised by following the strain softening curve of the joint elements. Details can be found in section 4.3 and Munjiza (1999). The original model is based on the Mode I loading condition, which applies to most practical application of brittle and quasi-brittle materials, and can be extended readily for the glass fracture analysis.

Joint elements are employed in the FEM/DEM fracture model and have been discussed in Chapter 3. For any connecting pairs of finite-discrete elements, there is no contact force at the beginning and just be connected by the corresponding joint element. The status from continua to discontinua is determined by the deformation of joint elements, and discussion can be found in section 3.2.2.

In this chapter, a glass fracture model based on Mode I loading condition is discussed. Literature over the fracture models are reviewed in section 4.2. In section 4.3, the combined

single and smeared crack model originally implemented for concrete is extended to glass by modifying the strain softening curve. Sensitivity analysis, including the convergence, influences of time step and penalty parameters are discussed in section 4.4. Numerical examples are used for verification with discussions in section 4.5 and some conclusions were reached in section 4.6.

4.2 Literature Review

There are various models proposed to describe the damage behaviour from fracture mechanics, such as the stress intensity factor approach (Irwin, 1956), the “strip-yield” model by Dugdale (1960) and the cohesive force model by Barenblatt (1959, 1962).

Irwin (1956) developed the concept of stress intensity factor when he extended the elliptical flaw to line crack from Griffith (1920).The stress intensity factor approach studied the stress near the crack tip and the stress will theoretically be infinite at the crack tip according to equation 4.1

$$\sigma = \frac{K}{\sqrt{2\pi r}} \tag{4.1}$$

Where r is the distance to the crack tip and K is the stress intensity factor. Anderson (1991) listed some expressions of K under different types of loading. When K reaches the critical value K_c, the crack propagates. This method only applies to some simple cases as it is difficult to get a closed form solution of K for complicated specimen dimensions and loading

type. Moreover, the stress at the crack tip is singular, which limits the application of this method.

Dugdale (1960) developed a model suitable for elastic-plastic fracture in ductile material, like metal. A plastic zone with a stress distribution equal to the yield strength is assumed near the crack tip. Barenblatt (1959, 1962) proposed a similar model to Dugdale's but with variable stress distribution in relation with the deformation near the crack tip. Both methods define a fracture process zone (or cohesive zone, see Figure 4.1) and belong to the classification of cohesive model.

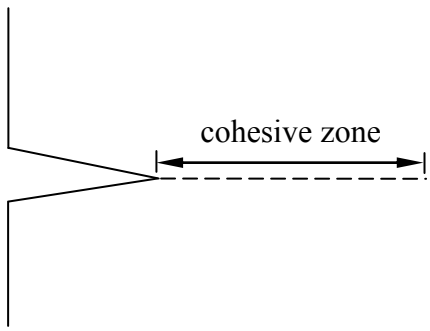

Figure 4.1 Schematic representation of a cohesive zone

There is a disadvantage in common that all the above methods require a pre-existed crack (or flaw) and cannot simulate the initiation but propagation only. This situation does not change until Hillerborg et al. (1976) introduced a fictitious crack model in middle 1970s.

In Hillerborg's model, the crack will develop when bonding stress σ reaches the tensile strength f_t, which is the start of the damage. However, the bonding stress is not assumed to

drop to zero immediately but to decrease gradually as the crack width δ increases. When δ reach the critical width δ_c, the stress will fall to zero. The relationship between bonding stress and crack width can be depicted as a descending curve, with the area between the curve and the coordinate axis equals to the energy absorbed per unit crack area as in equation 4.2.

$$G = \int_0^{\delta_c} \sigma \, d\delta \tag{4.2}$$

From this point of view, the outstanding descending curve is a combination of both cohesive model and energy approach (equation 4.2). Also, as Hillerborg's model does not assume a pre-existing crack, it is capable of capturing the initiation of a crack.

Seemingly, fracture energy G and the tensile strength f_t are two most important parameters in cohesive models, but researches (e.g. Rots, 1986; Chandra et al., 2002) indicated that the shape of the descending curve plays a much bigger role in combination with the fracture energy expressed in equation 4.2. Some representative curves were shown in Figure 4.2. Figure 4.2(a) is suitable for typical yielding material while Figure 4.2(c) has good agreement with quasi-brittle material. In this thesis, a strain softening curve similar to Figure 4.2(c) will be used. The details on this curve will be given and discussed in section 4.3.

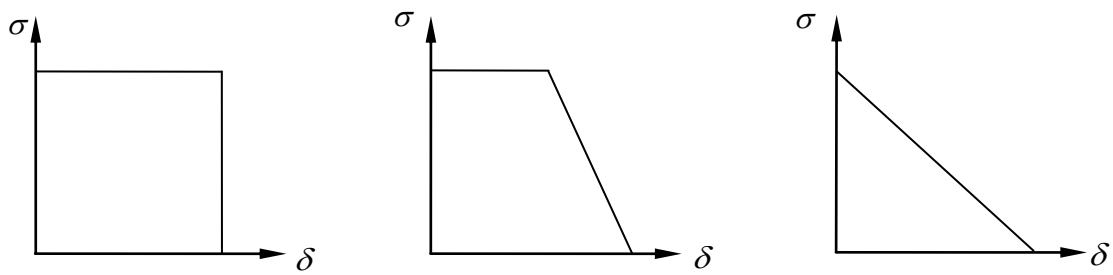

(a) (b) (c)

Figure 4.2 Possible assumptions of stress σ with crack width δ during softening

Regarding the development of the cohesive zone method, a modern computational framework has been established by Needleman (1987) and Camacho and Ortiz (1996). Within the framework of cohesive method, both discrete and smeared crack approaches can be implemented.

Ngo and Scordelis (1967) introduced the discrete crack model, which aims at simulating the initiation and propagation of dominant cracks. In its original form, a discrete weak interface is inserted into the entity if the crack path is experimentally or analytically known in advance. So that as long as fracture occurs, it can only develop along that particular direction. Figure 4.3 schematically demonstrated the crack in a single-edge notched (SEN) concrete beam obtained by Rots (1991) by inserting a pre-defined discrete interface between continuum elements along the potential crack path.

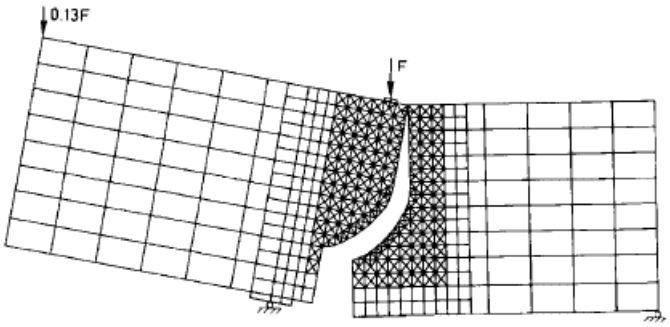

Figure 4.3 Deformed configuration of SEN-beam by smeared crack method (Rots, 1991)

Xu and Needleman (1994) inserted these discrete interfaces between all the continuum elements to obtain a more arbitrary direction of crack propagation. Camacho and Ortiz (1996)

proposed a related method using remeshing, which is not suitable for large-scale analysis. To alleviate the change of topology result from remeshing, meshless Galerkin method was proposed by Belytschko et al. (1994) and shortly had been combined with FEM by Hegen (1996).

Unlike the discrete crack model developed by Ngo and Scordelis (1967), the smeared crack approach does not resolve the individual dominant cracks numerically but captures the damage process through a weak constitutive relation of the material, enabling the cracks being smeared out over the continuum. It is based on the idea that small cracks nucleate in a later stage of loading to form one or more dominant cracks. This approach was first introduced by Rashid (1968) for the analysis of concrete pressure vessels. The concept has been further developed by Bazant and his co-workers (Bazant and Cedolin, 1979, 1980; Bazant and Oh, 1983). Malvar and Fourney (1990) implemented the smeared crack approach into FEM code ADINA and verified their model in both 2D and 3D with three point bend test by Malvar and Warren (1988). Petrangeli and Ožbolt (1996) discussed the material modelling using the smeared crack approach and the classification of this model based on material and structural properties was concluded and presented by Weihe et al. (1998). de Borst et al. (2004) tried to bridge the gap between discrete and smeared crack models and devised cohesive segment method, which is capable of describing the transition from distributed micro-cracking to a dominant crack. And a thorough review of the formulations used over last 40 years with both discrete and smeared crack approach was carried out by Cervera and Chiumenti (2006).

Regarding recent developments, a new model aims at radial crack was presented by Repetto (2000) without artificially constraining fragment rotation within meridian planes of glass rods. Sun and Khaleel (2004) applied the continuum damage mechanics (CDM) into ABAQUS and studied the response of soda-lime glass subject to static indentation. Later, Sun and his co-workers (Sun et al., 2005) extended this CDM to the investigation of the monolithic glass ply under stone impact. By using this method, the change of strain within the specimen can be obtained and the critical stress can be estimated. However, since CDM cannot predict the growth and propagation of individual cracks, no discrete crack can be obtained by this type of FE analysis. Grujicic et al. (2009) proposed a simple high strain-rate, high-pressure (around 400m/s) material model for the ballistic impact of soda-lime glass and embedded the model into the ABAQUS/Explicit. Their research focused on the propagation of the elastic (longitudinal and transverse) waves in the target within the very early impact stage (of the order of several μs) while no further investigation for the post-damage period.

4.3 Glass Fracture Model

The cracking model used in the FEM/DEM is similar to Hillerborg's (1976). The standard FEM formulation for the damage region combines the discrete-crack model for the crack opening. Smeared crack approach is applied after the normal stress reaches the tensile strength of the material. Unlike the discrete crack model developed by Ngo and Scordelis

(1967), the smeared crack approach does not solve the individual dominant cracks numerically but captures the damage process through a weak constitutive relation of the material, enabling the cracks being smeared out over the continuum.

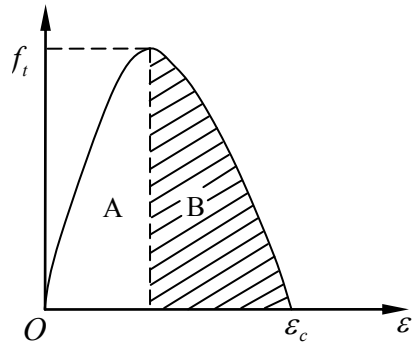

Figure 4.4 Strain hardening and softening curve

Figure 4.4 illustrated an ordinary stress-strain curve from elastic to fracture. The stress-strain curve can be divided into two parts. The left zone A depicts the elastic region that can be implemented by standard constitutive law. The shaded area B on the right represents the strain softening region. When the stress hits f_t, the crack initiates with a crack tip process zone where stress declines. As the bonding stress σ_n drops to zero, a complete separation will occur. At this point, we consider the two adjacent finite-discrete elements dissociated.

4.3.1 Model Description

In the model, cracks are assumed to occur coincide with element edges (Williams, 1988)

where joint elements are implemented in, which is a major limitation of this method. For Mode I fracture, the key idea is to calculate the bonded tensile stress of the joint element from the separation δ. Afterwards, nodal forces and deformation can be evaluated according to the finite element integration and rigid displacement can be obtained based on the Newton's second motion law.

Define δ_P to be the elastic limit, which is also the separation when bonded stress reaches the tensile strength f_t. δ_c is the ultimate separation when bonded stress decreases to zero. The calculation of bonded tensile stress σ_n can be classified as three conditions: (i) $\delta < 0$ (ii) $0 \le \delta \le \delta_p$ and (iii) $\delta > \delta_p$. The complete relations between normal bonding stress σ_n and the separation δ were expressed in the form of equation 4.3: (Munjiza, 1999)

$$\sigma_n = \begin{cases} \left[2\dfrac{\delta}{\delta_p} - \left(\dfrac{\delta}{\delta_p} \right)^2 \right] f_t & 0 \le \delta \le \delta_p \\ f_t \, z & \delta_p < \delta \le \delta_c \\ 2\dfrac{\delta}{\delta_p} f_t & \delta < 0 \end{cases} \tag{4.3}$$

where z is a heuristic parameter expressed in equation 4.4: (Munjiza, 1999)

$$z = \left[1 - \frac{a+b-1}{a+b} e^{D\,(a+bc/((a+b)\,(1-a-b)))} \right] \left[a(1-D) + b(1-D)^c \right] \tag{4.4}$$

while a, b and c are constants and D is the independent variable indicating the fracture damage index and varies within the interval $[0,\ 1]$. For $\delta > \delta_c$, $D = 1$; for $\delta_p < \delta \le \delta_c$, $D = (\delta - \delta_p)/(\delta_c - \delta_p)$.

For concrete, a = 0.63, b = 1.8, c = 6, $f_t = 3.15\text{MPa}$ and $\delta_c = 0.238\text{mm}$ (Munjiza et al., 1999). Suppose $\delta_p = 0.1\delta_c$, the normalized shape of curve expressed in Equation 4.3 from $-0.1\delta_c$ to δ_c was schematically shown in Figure 4.5.

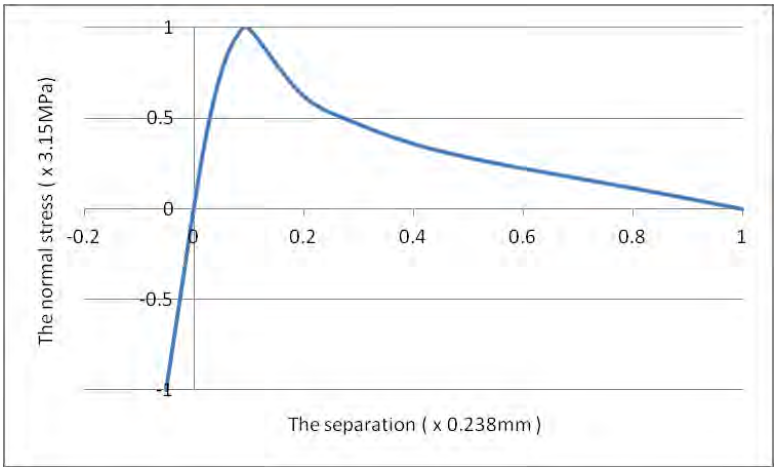

Figure 4.5 The normalized (f_t) stress-elongation and compression curve

If we take the damage index D to be the independent variable of the function z, some properties can be found in this z curve regardless of the values of a, b and c in equation 4.4. At the beginning $D = 0$, which means the material just start to damage, we have $z = 1$ and the tensile bonded stress is f_t. When D increases to 1, z decreases to zero, resulting in no bonded stress. By setting D to 1 when $\delta > \delta_c$, one can guarantee that for any separation exceeds the critical value δ_c, no bonding will exist between any two adjacent FEM/DEM elements, leading to the total fracture and free movement between them.

It can easily be demonstrated mathematically that equation 4.3 is C^0 continuous on $D \in [0,\ 1]$,

avoiding any stress interruption. After obtaining the bonded stress, nodal forces can be integrated using normal FEM approach and displacement calculation, contact detection and interaction can be carried out afterwards.

4.3.2 Determination of Strain Softening Curve

In order to determine the strain softening behaviour of glass, numerical trials with different values of *a*, *b* and *c* were performed. A 2m long 20mm thick 2D glass beam was considered as the sample. The projectile is of the shape of a regular octagon with the diameter of 50mm, impacted the beam at the velocity of 5.85m/s. This is a typical shallow beam problem with the projectile large enough to damage and penetrate. Configurations of the structure are shown in Figure 4.5 and material properties are tabulated in Table 4.1. The material properties of glass beam were taken from Ledbetter et al. (2006) and the projectile is steel with fracture energy and tensile strength be set as large values so that fracture will not occur.

Figure 4.5 The configuration of glass structure

	Beam	Projectile
Density	2500kg/m^3	7800kg/m^3
Young's Modulus	7x10^{10}N/m^2	2x10^{11}N/m^2
Shear Modulus	3x10^{10}N/m^2	7.69x10^{10}N/m^2
Poisson's Ratio	0.2	0.3
Fracture Energy	4.0 N/m	2.5x10^5 N/m

Tensile Strength	20MPa	2.35 x10^5MPa

Table 4.1 Material properties of the beam and projectile

Different values of *a*, *b* and *c* in equation 4.4 will result in different shapes of curves along the interval $D \in [0, 1]$. Four curves were tested including linear descending and three decay curves. For the sake of convenience, curves are noted as i, ii, iii and iv. For curve i, *a* = 0.9, *b* = 0.55, *c* = 1.0; curve ii, *a* = 1.2, *b* = 0.55, *c* = 0.9; curve iii, *a* = 1.2, *b* = -1.0, *c* = 1.0; and curve iv, *a* = 1.09, *b* = -1.0, *c* = 1.0. Figure 4.6 schematically showed the four curves (the ultimate strain for curve (i) is normalised to unity).

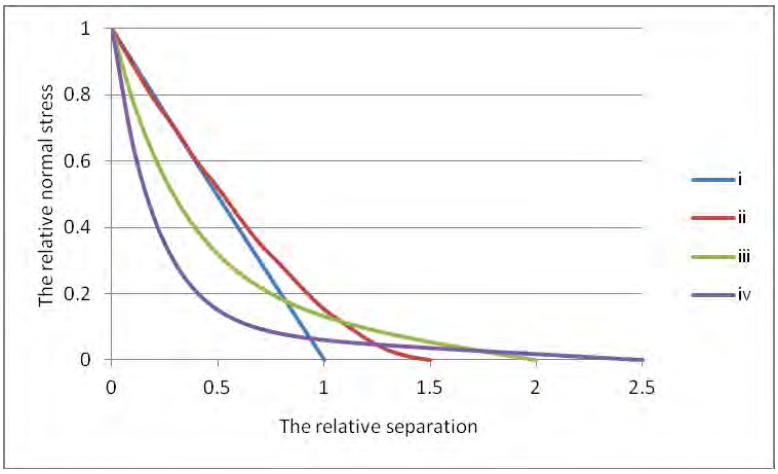

Figure 4.6 Different strain softening curves according to different values of *a*, *b* and *c*

Corresponding damage responses of the beam at t = 2ms were presented in Figure 4.7. For strain softening curves i and ii, two types of damage can be found in Figure 4.7 (a) and (b). One is in the middle of the beam where the impact area situates, the other is slightly away from the middle where the beam exhibited bending damage and fractured through the

thickness.

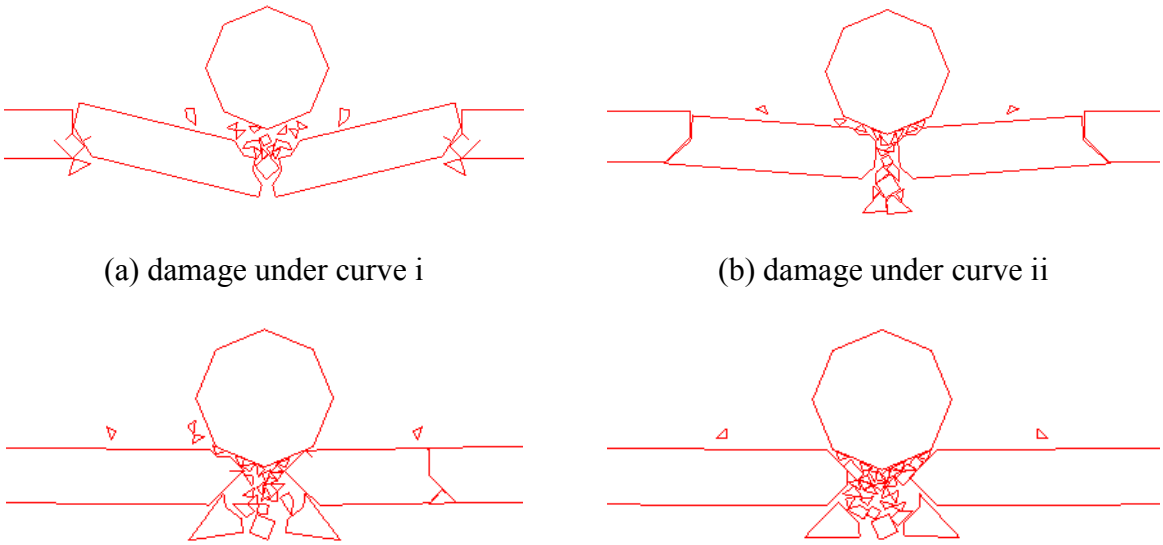

(a) damage under curve i (b) damage under curve ii

(c) damage under curve iii (d) damage under curve iv

Figure 4.7 Cracking patterns of the sample under different softening curves at t = 2ms

For curves iii and iv, the observed damage patterns were localized within the impact area and a cone type crack was obtained for both curves (Figure 4.7(c) and (d)). The difference is Figure 4.7(c) suffered some bending cracking on the right of the impact point but Figure 4.7(d) did not. This can be explained by equation 4.5 (Munjiza, 2000)

$$G_f = \frac{1}{n} f_t \delta_c \tag{4.5}$$

where n is a coefficient to ensure the area covered by the strain softening curve and the coordinate axis is equal to the fracture energy. Since fracture energy G_f and tensile strength f_t are assumed to be constants, z curve with sharper drop will have a larger value of n, resulting in a larger δ_c, making the structure requiring larger separation to break. That is why bending damage was not found in Figure 4.7(d).

Comparing with the results in Figure 4.7, cone type cracks were obtained using curves iii and iv while bending was dominant for the results using curve i and ii. Referring to Figure 4.6, curve iii has moderate critical separation distance and sharp enough softening descending slope. Numerically, according to the power softening law (Equation 4.6) given by Foote et al., (1986), brittle material can be represented by a large exponent *n*, which demonstrated a exponential curve such as curve iii and is suitable for glass.

$$\frac{\sigma}{f_t} = \left[1 - \frac{\delta}{\delta_c}\right]^n \tag{4.6}$$

The CEB-FIP Model Code (1990) recommended a bilinear curve for the softening, which was shown in Figure 4.8.

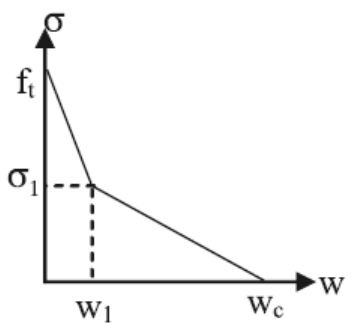

Figure 4.8 The bilinear strain softening curve (after Rama Chandra Murthy et al., 2009)

In Jefferson (1989), a stepwise softening curve was used to obtain the stability of computation for bilinear descending curve. By using an exponential decay curve iii, the bilinear property can be represented in a smooth way. And all the results on the fracture of glass in the rest of this chapter were based on that curve.

4.4 Sensitivity Analysis

As a smeared crack model, the combined single and smeared crack model used in FEM/DEM is sensitive to mesh topology. This is determined by the characteristic of the model itself (Petrangeli, 1996; Cervera, 2006). In addition, the model is also sensitive associated with FEM/DEM parameters.

In this section, the structure configurations in Figure 4.5, material properties in Table 4.1 and the impact velocity were kept unaltered to investigate the sensitivity to mesh size, time step and penalty parameters.

4.4.1 Convergence

Different meshes of the glass beam were used to study the convergence of the FEM/DEM program. The study started from the coarse mesh to a fine one with the number of elements in the glass beam from 400 to 25600, and damage patterns at t = 2.5ms were presented below their mesh configuration (Figure 4.8).

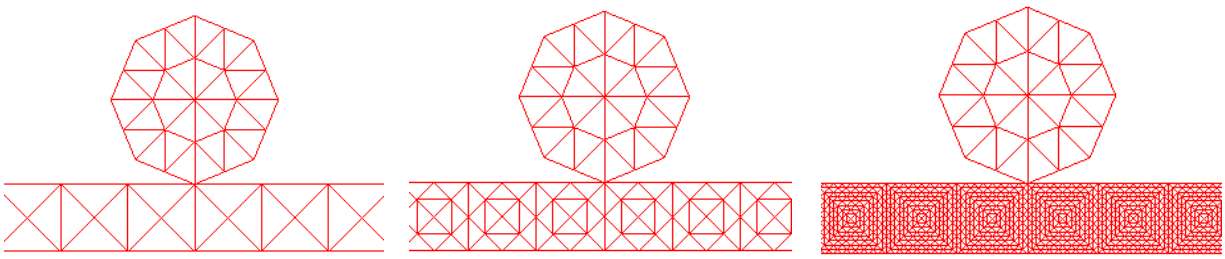

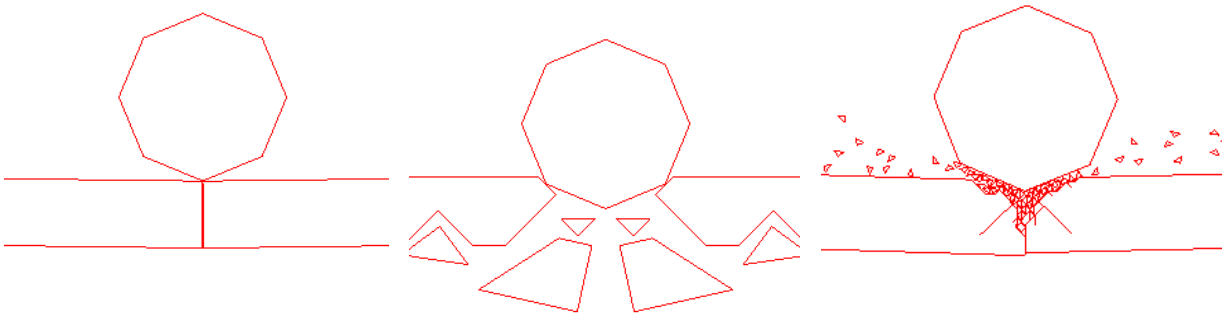

(a) 400 elements (b) 1600 elements (c) 25600 elements

Figure 4.8 Mesh configurations for the convergence study at t = 2.5ms

It can be observed from Figure 4.8 that the coarse mesh is more inclined to generate dominate crack (only a through thickness crack was obtained in Figure 4.8(a)) due to poor stress distribution and lack of sufficient elements to model the stress distribution more accurately. While fine mesh produces better numerical results and small fragments were obtained in Figure 4.8(c). In the following research, mesh strategy with finer mesh in the impact area while coarser mesh in the distance will be employed.

4.4.2 Time step

As was mentioned in Chapter 3, time step is crucial to guarantee the success of simulation. Determination of the time step is a balance between efficiency and effectiveness. If the time step is too small, the program will be executed in an inefficient way; on the contrary, the simulation can be unstable resulting in numerical distortion.

As a general rule, time step Δt should satisfy the inequality (4.7).

$$\Delta t < h\sqrt{\frac{\rho}{E}} \tag{4.7}$$

Where h is the smallest characteristic size of discrete elements, ρ is the material density and E is the Young's Modulus. This inequality provides an estimate of the time step.

If the time step of the example in section 4.3.2 was set to a large value, the structure will be unstable and explode (Figure 4.9), which is unrealistic.

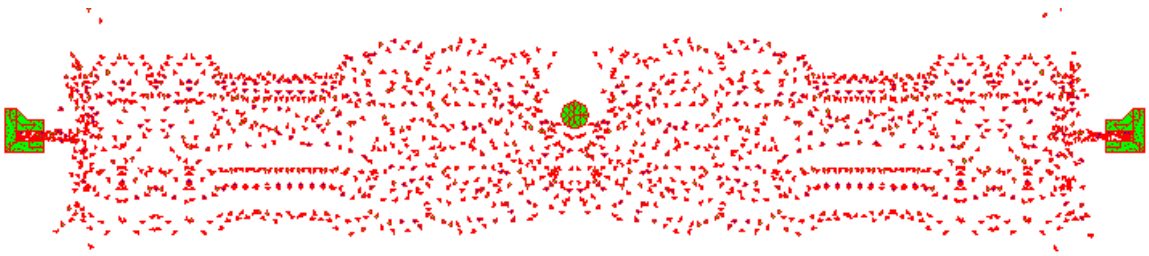

Figure 4.9 The exploded beam due to large time step

On the other hand, should the time step lie below the critical value, simulation can be carried out correctly and no visible difference on the damage behaviour between the results from larger time step and smaller one. However, there may be small difference in the change of the total kinetic energy for smaller time step as more intermediate values between larger time steps can be outputted. Figure 4.10 showed the two curves of the change of total kinetic energy with different time steps below the critical value.

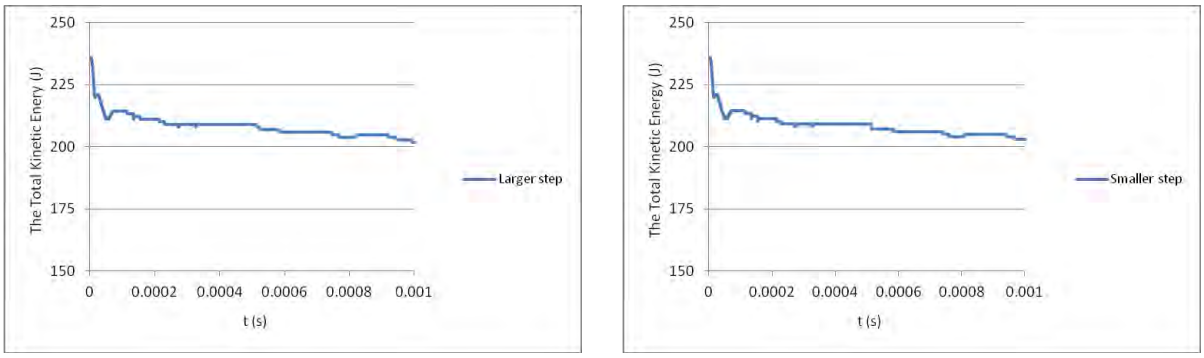

(a) Larger time step (b) Smaller time step

Figure 4.10 Tiny difference of total kinetic energy obtained using large and small time steps respectively

4.4.3 Penalty Parameters

There are two penalty parameters defined in the FEM/DEM: /YD/YDPE/D1PEPE (p_1 for short) and /YD/YDPJ/D1PJPE (p_2 for short). The first one is associated with contact while the second is related to fracture.

In the FEM/DEM, parameter p_1 is used to control the penetration between elements. To limit the penetration, an appropriate value that proportional to the modulus of elasticity should be selected for p_1 in equation (4.8)

$$p_1 = \alpha E \tag{4.8}$$

where α is a coefficient. Thus, the contribution of the allowed penetration d to the displacement u can be expressed in equation (4.9).

$$d = \frac{u}{\alpha} \tag{4.9}$$

Obviously, the larger α, the smaller *d*. Munjiza (2004) suggested that p_1 to be 2 to 100 times of the Lamé elastic constant λ expressed in (4.10) to achieve reasonable results.

$$\lambda = \frac{\nu E}{(1+\nu)(1-2\nu)} \tag{4.10}$$

For glass, since $E = 70\text{GPa}$ and $\nu = 0.2$ were used from Table 4.1, $\lambda = 1.94\times10^{10}$ Pa. In the previous study, $p_1 = 1\times10^{11}$ Pa was chosen. Smaller p_1 will result in larger penetration as was shown in Figure 4.10.

(a) t =0.375 ms (b) t = 0.75 ms

Figure 4.10 The penetration of projectile due to small $p_1 = 1\times10^7$ Pa

The second parameter p_2 is used for describing the fracture criterion. In the FEM/DEM program, the elastic limit o_p and the critical separation o_t are defined in equation (4.11)

$$o_p = \frac{2hf_t}{p_2} \tag{4.11}$$

And in order to make sure $o_t > o_p$, $o_t = \max\left(2o_p, \frac{n\,G_f}{f_t}\right)$, where *n* is a constant depends on the shape of strain softening curve.

Ideally, $2o_p < \frac{n\,G_f}{f_t}$ so that the properties of the strain-softening curve can be reflected all the way to the critical separation o_t. In conjunction with equation 4.11, this requires the

penalty parameter p_2 be larger than a critical value (Inequality 4.12).

$$p_2 > \frac{h f_t^2}{G_f} \tag{4.12}$$

For glass with $G_f = 4.0N/m$, $f_t = 30MPa$ and h = 0.5mm, p_2 should be larger than 1.125×10^{11} Pa. For the previous glass example, $p_2 = 1\times10^{14}$ Pa was used, which satisfies the requirement.

If p_2 is not large enough, o_p will be so large that o_t will always take the value of $2o_p$ regardless of what the real critical separation distance $\frac{n\,G_f}{f_t}$ should be. This actually changed the material properties, leading the fracture more difficult to occur as the critical separation has been increased (Figure 4.11), and Munjiza (2004) also suggested p_2 "several orders of magnitudes greater than the Lamé constant".

(a) t = 0.75 ms (b) t = 1.5 ms

Figure 4.11 The artificial "strong" sample due to small $p_2 = 1\times10^7$ Pa

4.5 Numerical Examples

In this section, 2D and 3D models were investigated. In 2D, a plane stress problem with a glass beam subject to the impact of a circular projectile was studied. In 3D, a clamped circular

glass plate subjected to a steel bullet impact.

4.5.1 2D Glass Beam Subject to Impact of Circular Projectile

Consider a monolithic glass beam with the length of 2m clamped (no rotation but free horizontal movement) with both edges in rigid channels (Figure 4.12(a)). The beam, with the height of 20mm, is subjected to the impact of a 25mm radius steel circular projectile at a velocity of 5.85m/s. Material properties are the same as that given in Table 1.

Element meshes were generated using ABAQUS CAE, then transfered to the FEM/DEM program Y input format (Munjiza, 2000). Free mesh algorithm was used and irregular mesh orientation was achieved. The mesh density was very fine in the impact area but coarse in the far field, and the total number of elements is 26976 for glass and 441 for the projectile. It cost about 83 hours to run 0.2ms simulation. The mesh configuration within the impact effective area was schematically shown in Figure 4.12(b).

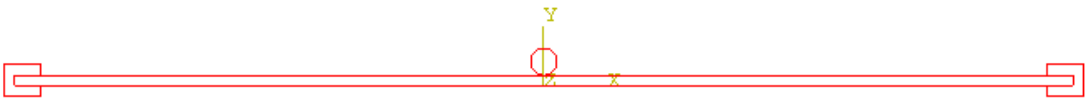

(a) The structural configuration and boundary condition of the 2D glass beam

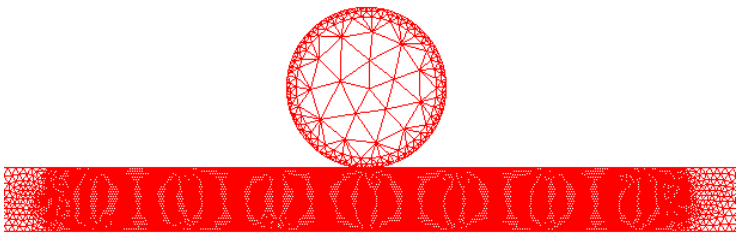

(b) The mesh configuration of the 2D glass beam within the impact effective area

Figure 4.12 The structural and mesh configuration of the 2D model

Transient responses at the early stage of impact were presented in Figure 4.13, showing the damage initation and propagation process and the formation of a Hertzian type cone.

From Figure 4.13, the damage process was illustrated by the development of crack pattern. Immediately after the ball hits the glass surface (t = 0.002ms), only some local damage occurred as can be seen in Figure 4.13(a). Later on, a horizontal crack developed as the departing stress wave from the top meets the reflected one from, tearing the glass within the glass thickness (Figure 4.13(b) and (c)). With the time elapsing, a Hertzian type cone crack was observed and developed (Figure 4.13 (d) to (f)). Meanwhile, small fragmentations were also produced in the local damage area due to the impact. The projectile was still staying on the glass beam and has not punched through it yet at the end of the simulation.

(a) t = 0.002 ms

(b) t = 0.01 ms

(c) t = 0.02 ms

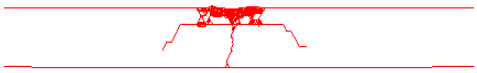

(d) t = 0.04 ms

(e) t = 0.1 ms

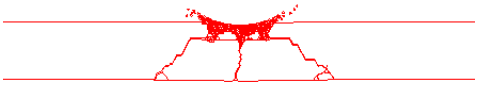

(f) t = 0.2 ms

Figure 4.13 The transient fracture cracks at different time points

It is worth mentioning thay at t = 0.1 ms, the formation of the cone type crack almost finished. The formation of cone crack in such short time agrees with the observation of Hertz (1896).

4.5.2 3D Clamped Glass Plate Subject to Hemisphere Cylinder Impact

In order to study the damage response of 3D glass plates, a circular monolithic glass with the radius of 50mm and the thickness of 4mm clamped around the entire circumference was investigated. The projectile is a 33mm high hemisphere cylinder. The radius of the cylinder is 10mm and hit the middle of the glass with the velocity of 1.98m/s. These dimensions and impact velocity were such chosen so that direct comparison can be made with the experimental and numerical results from Pauw (2010). One layer of elements with the characteristic size of 4mm were used in the FEM/DEM simulation to save the computation time. The number of glass elements is 4358, and 22.7 days of computational time (Intel 2.66GHz processor) was used to bring the simulation to 10ms. Structure and mesh configurations were shown in Figure 4.14(a). In the FEM/DEM simulation, two steel rings with the outer radius of 50cm, inner radius of 45mm and thickness of 2mm (Figure 4.14(b)) were used to rigidly fix the boundary of the circular plate. The plate cannot rotate in the clamps but can move freely within the plane of itself. In this case, the Poisson's ratio is 0.23 (as it was in Pauw (2010)), and all other material properties are the same as that in Table 4.1.

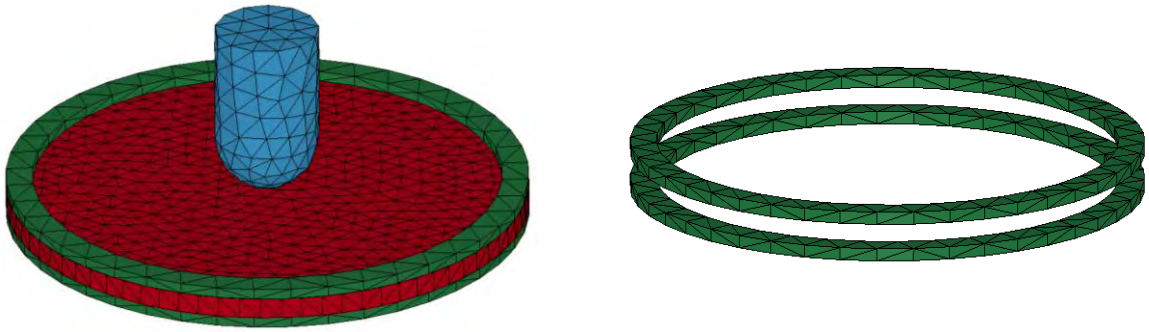

(a) Structural and mesh configurations (b) Ring supporters

Figure 4.14 Structure, boundary and mesh configurations of the 3D impact problem

The final damage pattern at t = 10ms was given by Figure 4.15(a). It can be observed that damage is mainly localized within the impact area and the projectile started to penetrate the glass plate. Since there is only one layer along the thickness of the glass plate, the bending of the plate cannot be well represented and no radial crack was obtained. However, the result agrees with that obtained from ABAQUS using the same type of elements and same number of layers along the thickness in Figure 4.15(b) (Pauw, 2010).

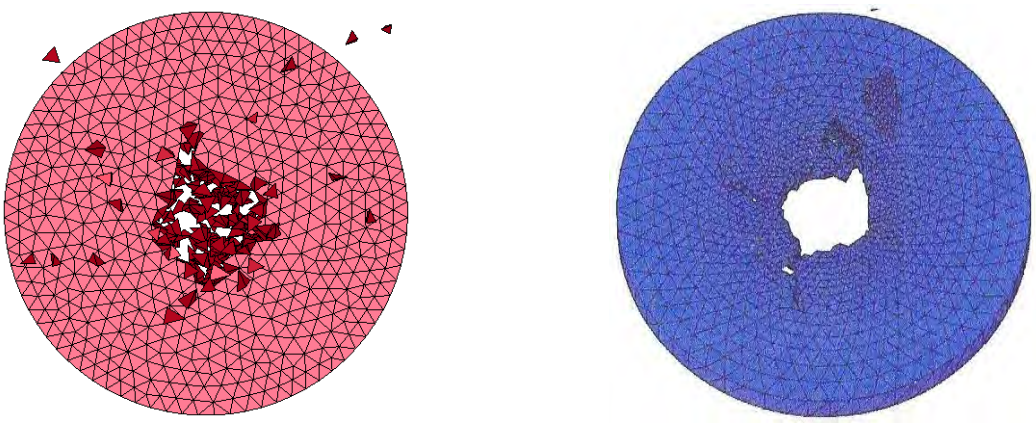

(a) By FEM/DEM (b) By ABAQUS

Figure 4.15 Damage pattern of 3D circular plate at 10ms

By refining the mesh (Figure 4.16), example with two layers was studied for this problem with results schematically shown in Figure 4.17. About 6 days of computational time was used for the simulation up to 10ms. Due to bending, the damage at the bottom was more severe than that of the top. Some propagation of radial crack can be found at the bottom in the final configuration of the damage.

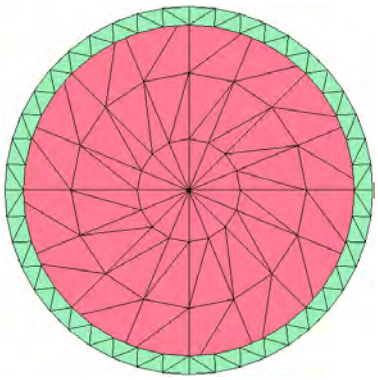

Figure 4.16 The mesh configuration used in the glass plate with two layers

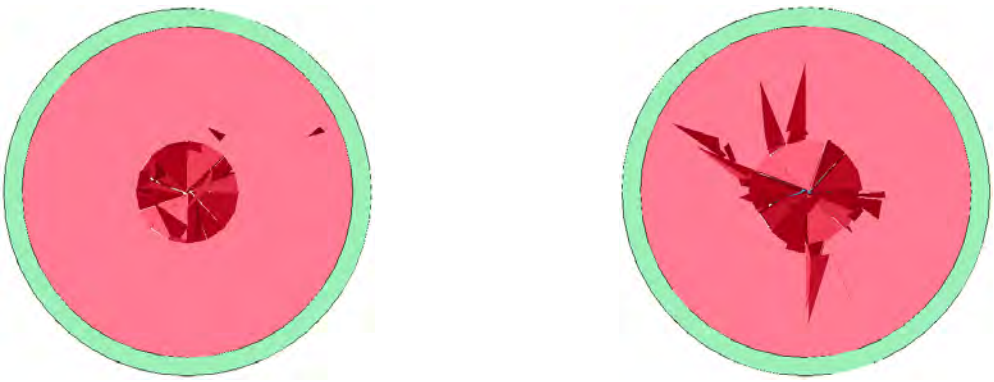

(a) View from top (b) View from bottom

Figure 4.17 Damage response of the glass plate with two layers along thickness at t = 10ms (the dark pink in the middle of the plate represent for the fractured glass fragments)

Should the element size along the thickness be further halved from Figure 4.16, a four layer

example was obtained. Since there are more elements along the thickness, the bending of the plate became much more obvious. Figure 4.18 gave the damage response of the plate with four layers along the thickness at t = 0.4ms. It can be observed that besides the central punching, radial cracks developed and propagated to the boundary of the glass plate.

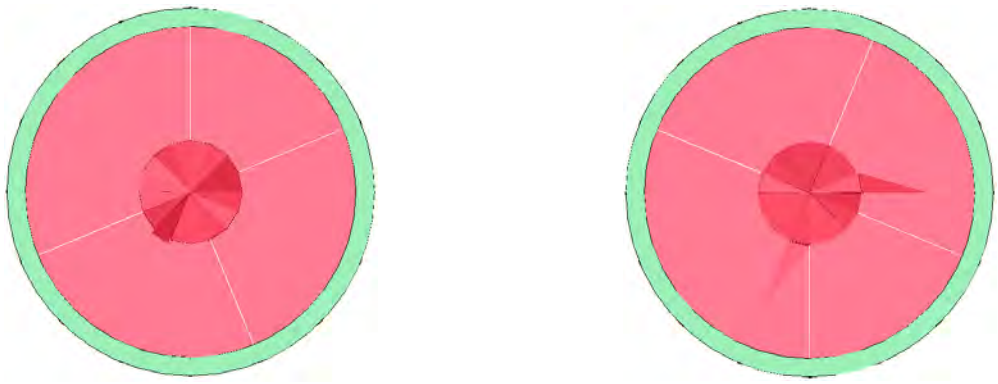

(a) View from top (b) View from bottom

Figure 4.18 Radial crack and central damage with four layers along thickness at t = 0.4ms

Pauw (2010) also performed FEM study using multiple layers of elements along the thickness and radial cracks were obtained (Figure 4.19). By comparing Figure 4.18 and 4.19, satisfactory agreement was obtained.

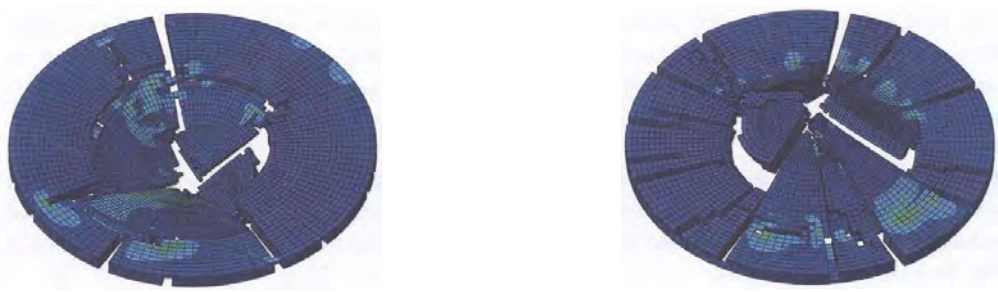

(a) View from top (b) View from bottom

Figure 4.19 Damage response of glass plate at t = 10ms from FEM simulation using

hexahedral sweep element and multi-layers along thickness (after Pauw (2010))

Although the simulated results from the FEM/DEM is not exactly the same as the experimental observation shown in Figure 4.20, it can be anticipated that with further increase in the number of elements along the thickness, the results will be more and more close to the test data.

Figure 4.19 Experimental observation of the damage after impact (after Pauw (2010))

It also should be noted that with the increase of element numbers, the computation time for 3D is quite considerable and usually cannot be obtained with reasonable time using the facility available. For the example with four layers, roughly 10 days are needed for the computation of 0.4ms of model time. This results in great difficulty in simulating large scale problems and parallelisation is currently the best solution but a parallelised version of the program has not been made available to this research. These computation issues will all be further addressed in chapter 8.

4.6 Conclusions

In this chapter, the Mode I fracture model of glass was presented. The model is extended by modifying the strain softening curve from the combined single and smeared crack model in the FEM/DEM. Specific literature review on numerical model was performed in section 4.2 and details of the model were given in section 4.3 followed by the analysis of sensitivity, showing that the FEM/DEM has good convergence with (1) the refinement of element mesh (2) small enough time step (3) large enough penalty parameters.

Numerical examples of both glass beam and plate were given in section 4.6. Cases of the beam subjected to the impact of a circular body and circular plate subjected to half-sphere cylinder were studied. Results were discussed and demonstrated that the FEM/DEM together with the proposed Mode I crack model is applicable for analysing glass impact problems. For 2D example, a Hertzian type cone was obtained, reaching good agreement with Hertz (1896). For 3D modelling, results from the FEM/DEM were compared with the independent FEM simulation and test results. For glass plate with one element layer along the thickness, damage was localised at the middle of impact area and no radical crack can be obtained since little bending occurred. With an increase of layers along the thickness, the trend of bending became more and more obvious and radial cracks were observed in the example with four element layers. Results in this example reached good agreement with the experimental and numerical data from Pauw (2010).

Through examples, the reliability of the crack model implemented in the FEM/DEM program

was demonstrated and verified. Parametric studies will be performed in Chapter 5, taking into account various factors influencing the behaviour of glass under impact.

PARAMETRIC STUDY ON MONOLITHIC GLASS

5.1 Introduction

In this chapter, parametric studies of the material parameters of the monolithic glass are described. The fracture model used in this chapter is the one aims at the Mode I loading condition described in Chapter 4. Influences of parameters to the fracture responses of glass are studied and a few parameters are investigated, including the tensile strength and fracture energy of glass, impact velocity and angle, stress wave propagation, projectile size and number, thickness of glass and etc. Each section in this chapter will focus on one or two relevant parameters and results will be presented followed by essential discussions.

If not indicating specifically, material properties used in this chapter are the same as that in Table 4.1. While doing parametric study, only one parameter is changed at a time and all other parameters are kept unaltered.

Examples in this chapter show that monolithic glass is sensitive to impact and not suitable for structural purpose. Despite the vulnerability and brittleness of monolithic glass, some design guidance is still given at the end of this chapter and conclusions are summarised as well. The tensile strength, fracture energy and thickness of glass are considered the three most controlling factors that affect the impact damage responses of glass.

There are eight sections in this chapter. Apart from the introduction and summary at the beginning and the end, different parameters are addressed and discussed in the rest sections.

Section 5.2 will discuss the influences of tensile strength and fracture energy on the fracture behaviour of glass. Section 5.3 explains the impact velocity of projectile and its corresponding effect. The impact angle is investigated in section 5.4, followed by the stress wave propagation in section 5.5. The glass thickness is discussed in section 5.6 and in section 5.7, attention is given to the size and number of projectile.

5.2 Tensile Strength and Fracture Energy of Glass

As a cohesive model, tensile strength and fracture energy play important roles in the damage of glass subject to impact and other forms of external effect. (Elices et al., 2002; section 4.3 of thesis)

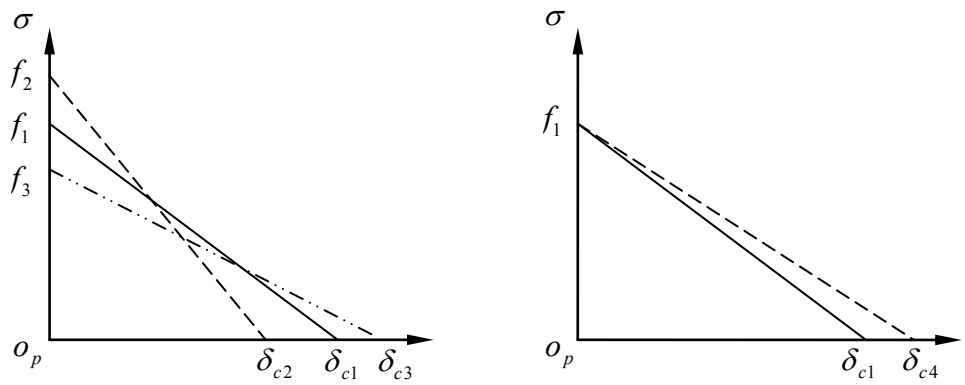

(a) Tensile strength (b) Fracture energy

Figure 5.1 Influences of tensile strength and fracture energy on strain softening curve

Take the linear strain softening curves for simplicity, Figure 5.1 clearly illustrated that both parameters affect the shape of the softening curve substantially. The solid line in Figure 5.1 represents the original strain softening curve while dashed lines denote the curves after change. It is worth mentioning that although linear softening curves were used here, similar

conclusion applies to curves of other shapes.

5.2.1 Tensile Strength

The tensile strength is the stress that damage process starts. According to Figure 5.1(a), since the fracture energy is fixed, higher tensile strength will raise the starting point of the strain softening curve from (o_p, f_1) to (o_p, f_2) and decrease the value of the critical separation distance from δ_{c1} to δ_{c2}, making the softening curve even steeper. On the contrary, lower tensile strength (f_3) requires a larger critical separation distance (δ_{c3}) to compensate the loss of area between the curve and the coordinate axis (equals to the fracture energy), resulting in a relatively flatter strain softening curve, and consequently, more ductile.

Figure 5.2 schematically illustrated the damage responses of a 2m long 20mm height clamped glass beam at t = 0.6ms with different tensile strengths subjected to a steel circle impact with the radius of 25mm at the velocity of 5.85m/s (refer to the section 4.5.1 in chapter 4 so that comparison can be done). In the following sections of this chapter, unless indicated specifically, numerical examples are based on the 2m long 20mm height clamped glass beam under the impact of a steel circle with the radius of 25mm, whose structural, boundary and mesh configurations can be referred to Figure 4.12.

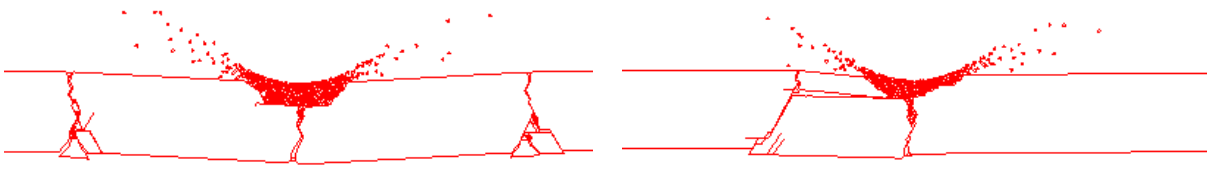

(a) f_t = 20 MPa (b) f_t = 40 MPa

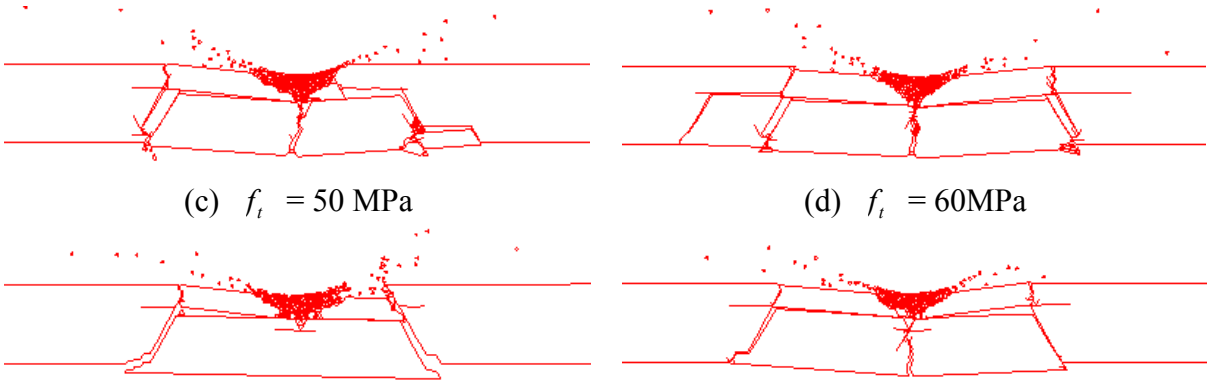

(c) f_t = 50 MPa (d) f_t = 60MPa

(e) f_t = 70MPa (f) f_t = 80MPa

Figure 5.2 Damage responses of glass with different tensile strength (f_t) for the same fracture energy (4N/m) at t = 0.6ms

It can be observed from Figure 5.2(a) that for lower tensile strength, ductility and bending damage was achieved. With the increase of tensile strength (Figure 5.2(b) to (f)), the beam became more and more brittle and the damage was mainly located within the impact effective area with no observation of bending failure, but a Hertzian type cone instead. This is due to the shortening of the descending curve and the material becomes more brittle.

5.2.2 Fracture Energy

In contrast with tensile strength, it is slightly simpler when it comes to the fracture energy. Keep the tensile strength unaltered, higher fracture energy (G_f) will result in a larger critical separation, namely δ_{c4} in Figure 5.1(b), pushing the stress going a flatter path during damage process.

In general, small G_f will exhibit brittleness while large value increases the ductility. Figure

5.3 listed a series of studies over different values of the fracture energy G_f and their final fracture patterns at t = 0.6 ms subject to impact of velocity of 5.85m/s.

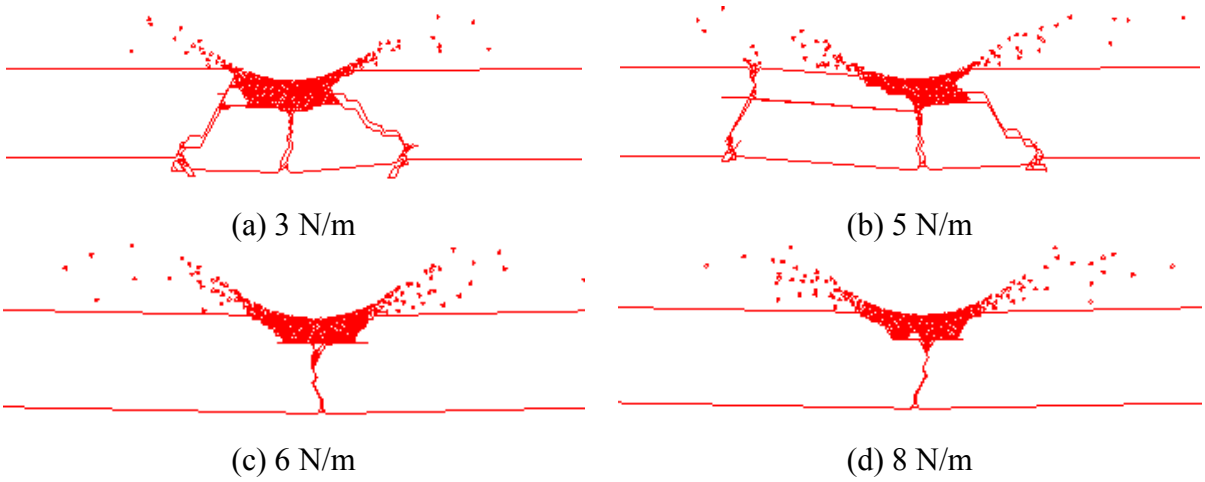

Figure 5.3 Damage responses of glass beam with different values of fracture energy with same tensile strength (f_t = 30 MPa) at t = 0.6ms

When G_f is low (3-5N/m, which is a reasonable range for glass (Linger and Holloway, 1968)), a Hertzian type cone is obtained (Figure 5.3(a) and (b)). If G_f becomes larger, no cone type crack can be obtained any more, leaving only a central through-thickness crack (Figure 5.3(c) and (d)). The disappearance of the cone crack can be attributed to the increase of the fracture energy, making some element boundaries unable to separate. Since less fracture occurred, only a central bending crack can be observed dominantly. The critical fracture energy which changed the failure mode from cone to bending crack is between 5N/m and 6N/m, and this value agrees well with Linger and Holloway (1968).

In order to evaluate the brittleness of the glass, a non-dimensional parameter κ in terms of the tensile strength f_t, fracture energy G_f and the thickness h was adopted, where

$$\kappa = \frac{f_t h}{G_f} \tag{5.1}$$

For some glass beam with a given thickness h, the larger the tensile strength (or the smaller the fracture energy), the larger the brittleness index κ will be, thus the more brittle the material is.

Although the relation in Equation 5.1 is simply linear, different combinations of f_t and G_f could generate different fracture behaviours of glass. According to the above study, for a velocity that is high enough, cone and bending cracks are two commonly observed types of damage. The transferring from bending to cone indicating that the material is experiencing brittling. The transit tensile strengths between these two damage types for different fracture energy were estimated in Table 5.1, which can be a guide for manufacturing glass catering to different needs.

G_f (N/m)	Transit f_t (MPa)
3	<20
4	20-30
5	20-30
6	>30

Table 5.1 The estimate of transition tensile strengths (from bending to cone crack) for glass under different values of fracture energy

The tensile strength is a starting point to control the damage commencement. Higher tensile strength will make the target more difficult to fracture if the input energy is not large enough. Meanwhile, when the target is in the fracture process, fracture energy has more control on the responses after damage commencement. For fracture problems employing cohesive models,

raising both the tensile strength (by using special cooling technique during manufacturing) and the fracture energy will greatly improve the performance of glass under impact.

5.3 Impact Velocity

Impact velocity is one of the most straightforward factors on the failure behaviour of glass. According to the expression of kinetic energy in equation 5.2,

$$E_k = \frac{1}{2} m v^2 \tag{5.2}$$

where m is the mass of projectile and v is the impact velocity, slight change of the impact velocity will change the input energy dramatically. In this study, only velocities below 50m/s were investigated and this is the basic wind speed of wind zone one (110-120 mph) according to ASTM E1996.

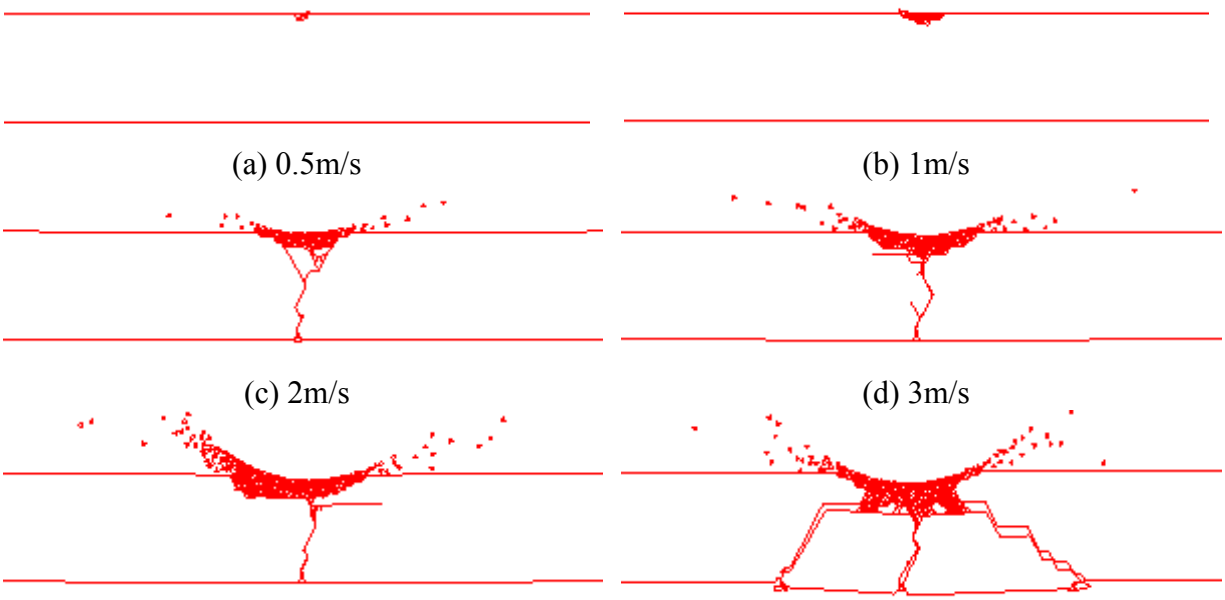

Figure 5.4 Damage patterns under different impact velocities (0.5-5m/s) at t = 0.6ms

Employing the same structural configurations in section 5.2, Figure 5.4 illustrated the damage patterns at t = 0.6ms under different impact velocities, ranging from 0.5m/s to 5m/s. Obviously, the damage was restricted to the local area when the impact velocity was very low (<1m/s). The projectile did not bounce back but staying on the beam with some residual velocity going downwards. Later, a penetration crack can be observed in the middle from Figure 5.4(c), (d) and (e). The cone crack will not appear until impact velocity reaches certain level (5m/s in this study).

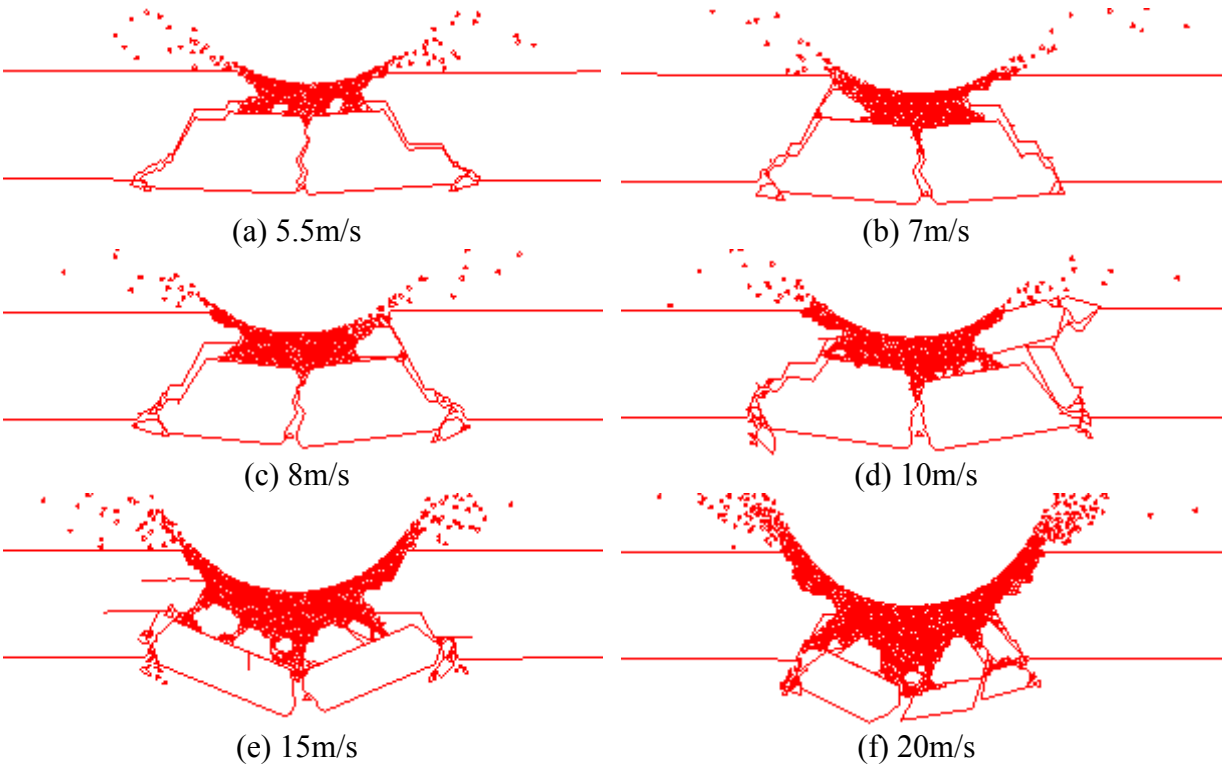

Figure 5.5 Damage pattern under different impact velocities (5-10m/s) at t = 0.6ms

For higher impact velocities (5-10m/s), a cone type crack is a typical phenomenon as can be observed in Figure 5.5. The higher the impact velocity, the more severe the damage will be. However, cone type crack is still recognizable when the impact velocity is below 20m/s. Even at 20m/s, the crack is still cone type.

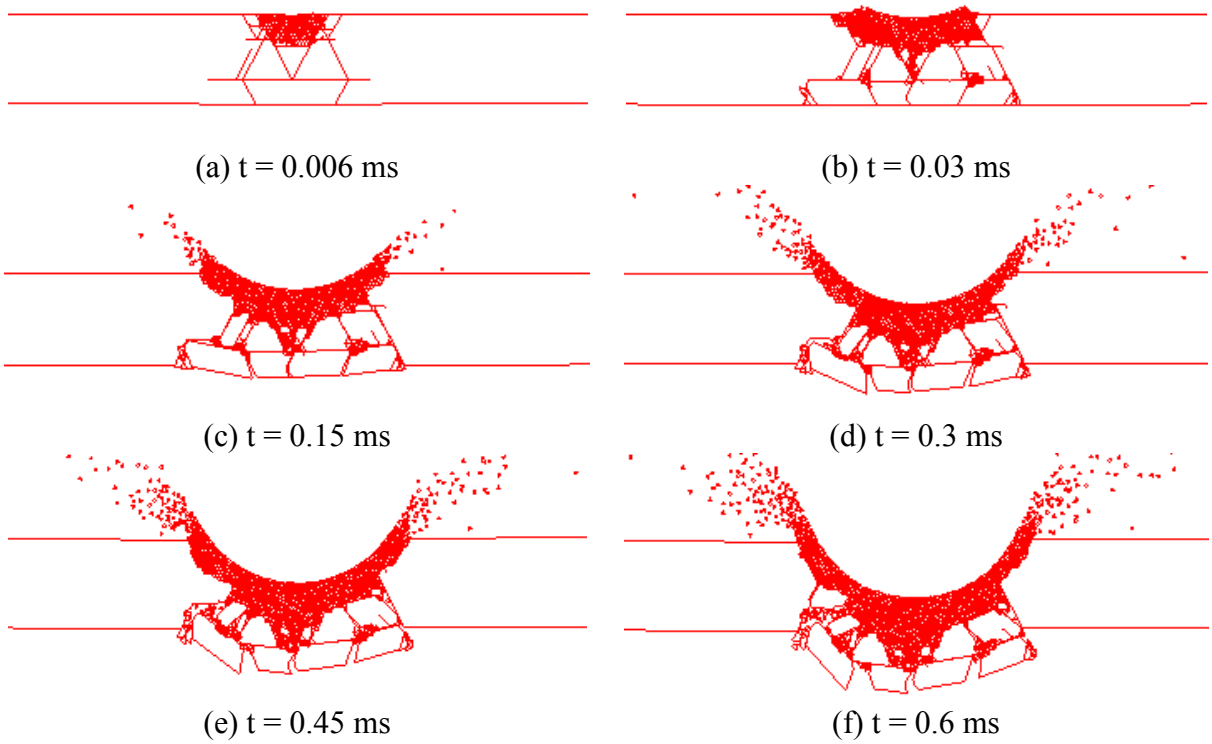

Figure 5.6 Transient dynamic response of beam subject to impact of 25m/s

Projectile with velocities higher than 20m/s cannot generate any recognizable Hertzian cone crack. Instead, crushing is dominant, leaving the impact area quickly be damaged. Large amount of input energy completely overpowers the resistance of glass, making the stress field within the glass body does not match the one that cone crack can be obtained. Figure 5.6 clearly illustrated the transient damage process under the impact at the velocity of 25m/s, and typical crushing was obtained.

For velocities higher than 25m/s, similar crushing damage was obtained and shown in Figure 5.7 (t = 0.6 ms). The glass within the impact effective area has been crushed into many fragments. Individual FEM/DEM elements (with one finite element mesh inside) were flying

above the top surface of the beam due to acquisition of kinetic energy, while larger fragments that have not yet been crushed due to bending and quick punching, separation and moving were obtained at the bottom of the beam.

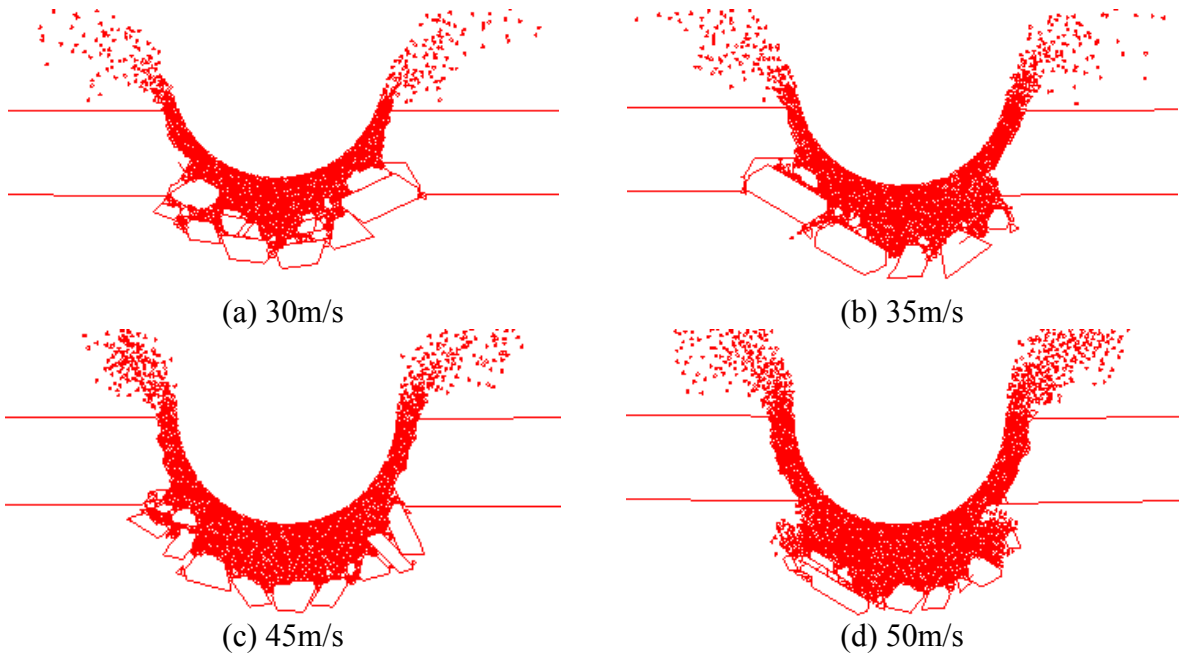

Figure 5.7 Damage under different impact velocities (30-50m/s) at t = 0.6ms

If we take the impact velocity *v* to be x-axis and the time *t* when the central penetration crack will appear (if applicable) to be y-axis, a descending curve can be plotted in Figure 5.8. This suggests that higher impact velocity will bring in more input energy, making the glass easier to fracture and the central penetration crack can be formed earlier as well. And one of the conclusions that can be made from Figure 5.8 is that for the punching failure, v-t has almost a constant linear relation.

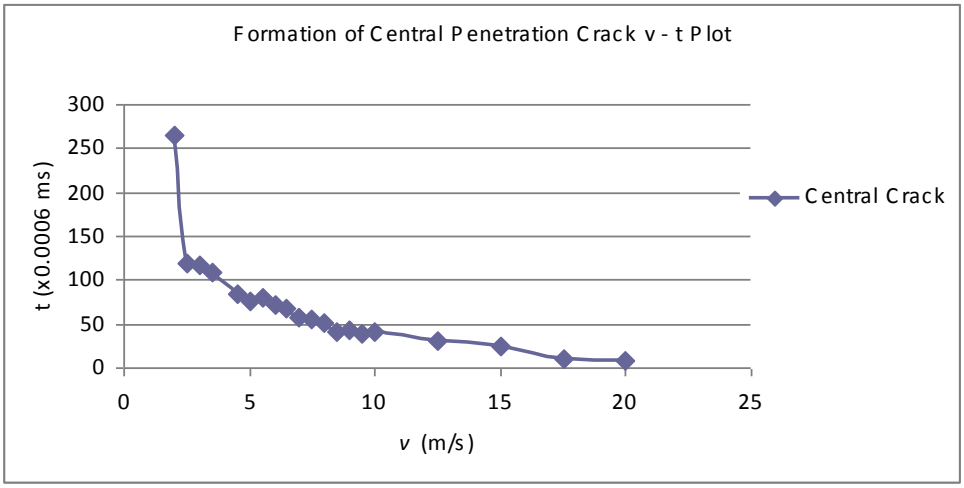

Figure 5.8 Time of the formation of central penetrating crack versus impact velocity

Another curve in Figure 5.9 showed the time when the cone crack was formed (if applicable). Similarly, the higher the impact velocity, the earlier a complete cone crack will appear. It is worth mentioning that the curves of central penetration crack and cone crack are almost parallel when the impact velocity v is higher than 7m/s. This suggested that cone failure requirs a certain amount of more time than central crack.

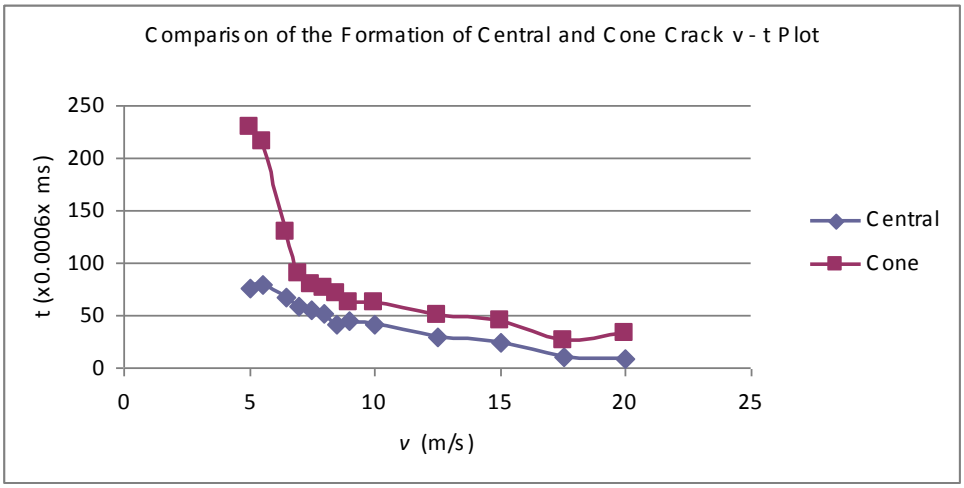

Figure 5.9 Comparison of the formation of central and cone crack

The trend of damage patterns under different velocities can be determined. Usually very local damage will occur at the surface where the projectile and target in contact when the impact velocity is very low. Then a central penetration crack followed by the cone type crack will appear up to certain critical velocity. Higher impact velocities will introduce crushing, making any regular crack impressions difficult to be observed.

Since four regimes of damage: (1) local minor damage, (2) central bending crack, (3) cone and (4) punching were observed, further study revealing the damage regimes was performed. From the energy point of view, if the fracture energy and the input kinetic energy were studied together, a diagram that indicates the change of the damage regimes can be obtained. Suppose the fracture energy times the thickness $G_f h$ (N) be the horizontal axis, and the input kinetic energy $\frac{1}{2}mv^2$ (J) be the vertical axis, zones of different types of damage were schematically shown in Figure 5.10.

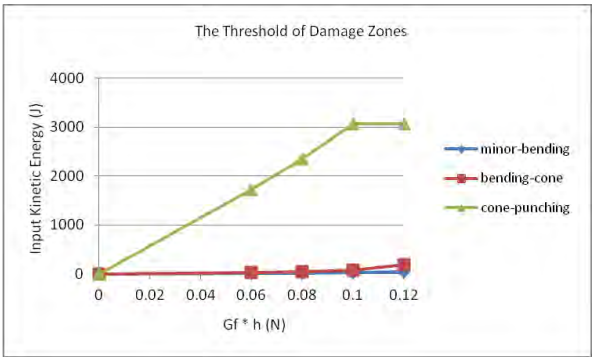

(a) Regimes of minor, bending, cone, punching damage

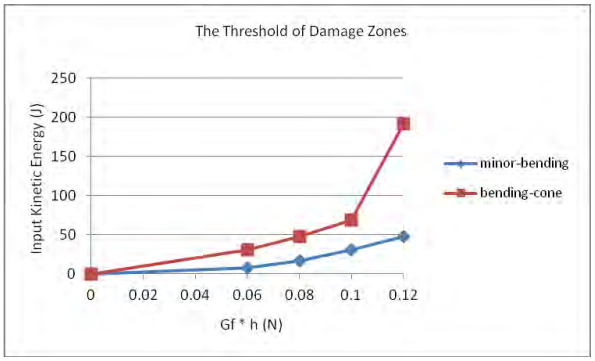

(b) Enlarged regimes of minor and bending damage

Figure 5.10 Regimes and threshold of different types of damage

In Figure 5.10, each curve represents a threshold for the transition from one type of damage to

another. The area between two adjacent curves is the regime that a particular type of damage (such as bending, cone) locates. It can be observed that with the increase of $G_f h$, the input energy $\frac{1}{2}mv^2$ needs for producing certain type of damage increases as well. Among these damage regimes, the local minor damage has the smallest regime as the input energy has to be very small. The bending crack also exists in a narrow band, with a large area of cone type crack over it. It is the typical damage pattern of glass under moderate impact energy. And for the regime of punching, there is no upper bound for it. The threshold of damage regimes is useful for both manufacturing and design.

5.4 Oblique Impact

If a non-zero horizontal component is involved in the velocity vector, an oblique impact will occur. In this section, the same configurations of the 2D glass beam in section 5.3 will be used. A set of oblique impact simulations were investigated according to different impact angles (Figure 5.11). In these examples, the vertical velocity was fixed at 5.85m/s, while the horizontal velocities are variable and point to the right, resulting in different oblique angles. Although the overall velocity will increase with the increase of horizontal component, perpendicular impact that along the weak direction of glass can be guaranteed.

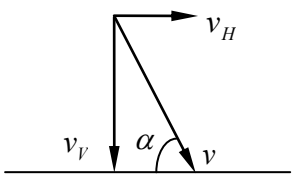

Figure 5.11 Definition of impact angle

According to Figure 5.11, when the horizontal velocity increases, the impact angle α decreases gradually. Damage responses under different oblique angles at t = 0.6 ms were shown in Figure 5.12 and 5.13. For impact angles larger than 45°, the oblique effect is not obvious and cone type cracks can be obtained. However, it can be observed from Figure 5.12 that with the increase of horizontal velocity, the right half of the cone lost the smoothness and became ragged.

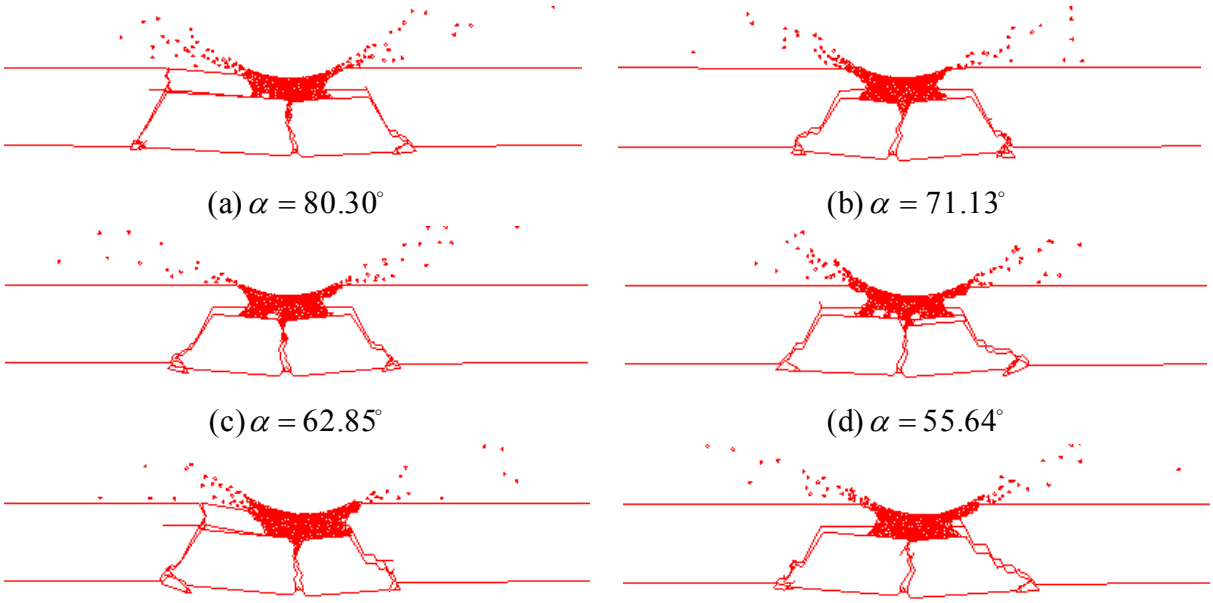

(a) $\alpha = 80.30^\circ$ (b) $\alpha = 71.13^\circ$

(c) $\alpha = 62.85^\circ$ (d) $\alpha = 55.64^\circ$

(e) $\alpha = 49.48^\circ$ (f) $\alpha = 45^\circ$

Figure 5.12 Damage responses of oblique impact ($\alpha \geq 45^\circ$) at t = 0.6ms

When the impact angle is between 0° and 45°, glass on the right, where the horizontal velocity points to, has to withstand compressive stresses and results in a complicated combined shear and compressive damage (Figure 5.13).

(a) $\alpha = 44.27^\circ$ (b) $\alpha = 39.89^\circ$

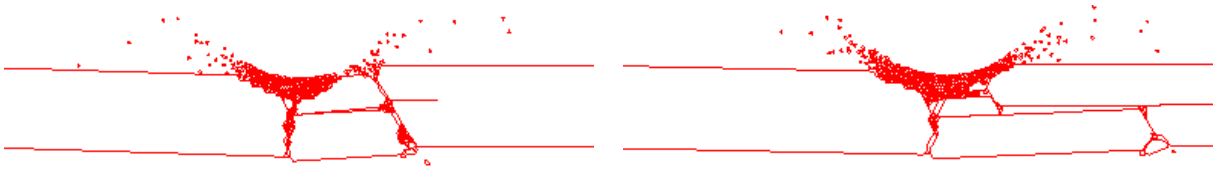

(c) $\alpha = 36.18^{\circ}$ (d) $\alpha = 30.33^{\circ}$

Figure 5.13 Damage responses of oblique impact ($\alpha < 45^{\circ}$) at t = 0.6ms

It can be concluded that when the impact angle is larger than 45°, no obvious change will be made to the crack pattern comparing with the perpendicular impact. Once the impact angle is smaller than 45°, oblique effect will be obvious, resulting in more damage to the side that horizontal velocity points to.

5.5 Stress Wave Propagation

In this section, the relationship between cracks and stress wave propagations was investigated. From the stress wave point of view, before the first dominant crack appears, stresses are transferred regularly in the glass media from the contact point to the far distance as is shown in Figure 5.14.

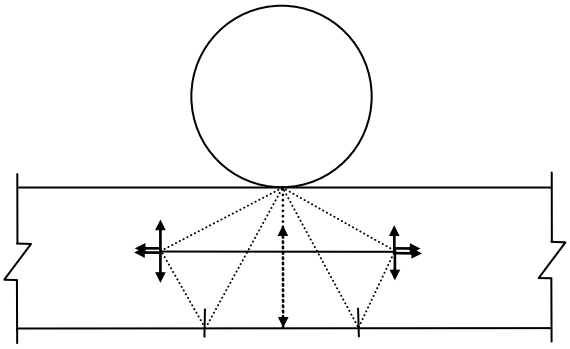

Figure 5.14 Travelling of stress waves in a shallow beam

For a shallow beam, stress waves travelling from the top can be effectively reflected back by the bottom of the beam. This will enable waves both travelling from top and bouncing back from the bottom meet at certain depth, resulting in a dominant horizontal crack. Figure 5.15 schematically presented the formation of the horizontal crack at different transient times.

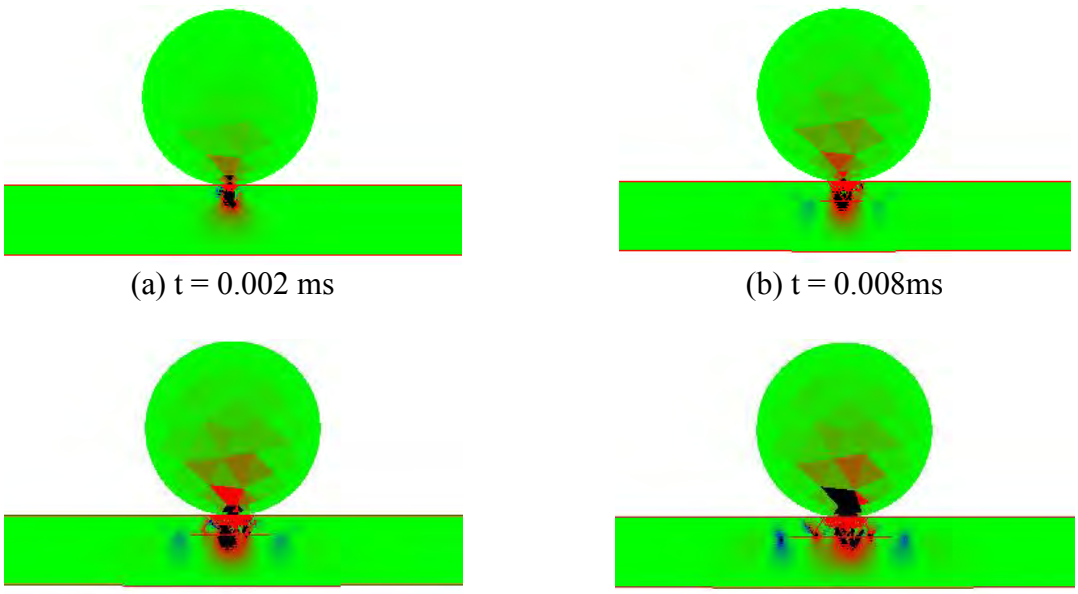

(a) t = 0.002 ms (b) t = 0.008ms

(c) t = 0.012ms (d) t = 0.014ms

Figure 5.15 Formation of the horizontal crack

According to Kolsky (1953), there are three types of waves that can propagate through a plane elastic solid with a free surface or a surface boundary between two solids: dilatational wave, distortional wave and Rayleigh surface wave. The particle motion in a plane dilatational wave is along the direction of propagation whilst in distortional wave it is perpendicular ro the direction of propagation. And the Rayleigh wave is along the free surface or surface between different solids. Among these three waves, the dilatational wave is dominant in this research.

The horizontal crack started from the centre of the impact area and extended to both directions.

However, the depth of the crack may vary and it depends on the amplitudes of both the waves that reflected back and generated from the contact point. Since the amplitudes of the stress waves are determined by the impact velocity, if the impact velocity increases, for example, from 5m/s to 15m/s, the depth of the horizontal crack will get deeper (Figure 5.16).

(a) v = 5m/s (b) v = 15m/s

Figure 5.16 Different impact velocities result in different depths of horizontal crack

Take the depth of horizontal crack from the upper surface of the beam to be h_o and the total depth of beam to be h, the ratio of h_o / h will increase along with the increase of impact velocity v (Figure 5.17), showing that higher impact velocity will make the dominant horizontal crack much deeper.

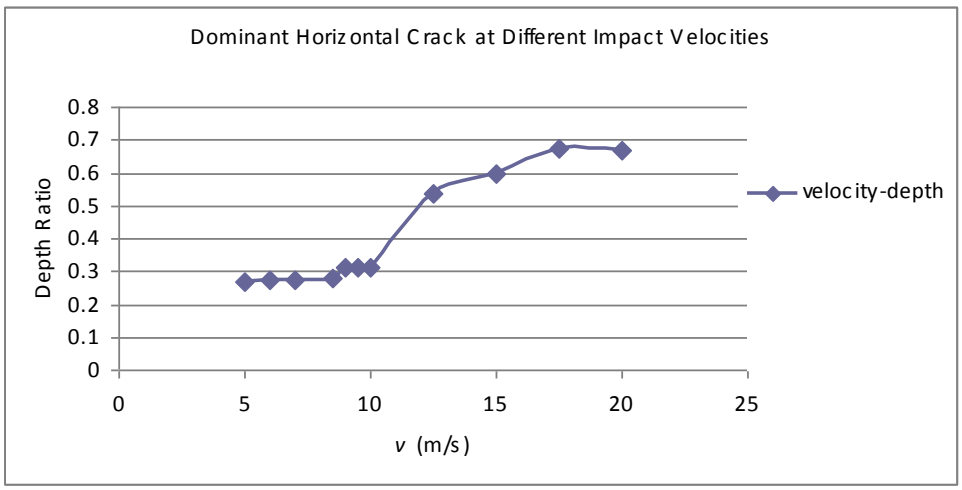

Figure 5.17 h_o / h at different applicable impact velocities

According to Figure 5.17, it can be observed that for lower impact velocities, the horizontal

crack is close to the top surface, while for higher velocities, its position is deeper. Also, conclusion can be made that the ratio h_o / h does not increase linearly with the impact velocity (there is a big increase after 10m/s), which indicated that the amplitude of stress wave is complicated with the impact velocity.

On the other hand, if there is no wave be reflected back or the wave that be reflected back is too weak, no dominant horizontal crack can be obtained. To study this, a glass block sized 75mm x 20mm subjected to a circle projectile with the radius of 1.57mm at the velocity of 2.2m/s will be investigated. The sample was placed on a rigid base to restrict its move along the vertical direction (Figure 5.18). The configuration was from an impact test conducted by Chai and Ravichandran (2009), and in the FEM/DEM simulation, 2D was used to replace the 3D test sample.

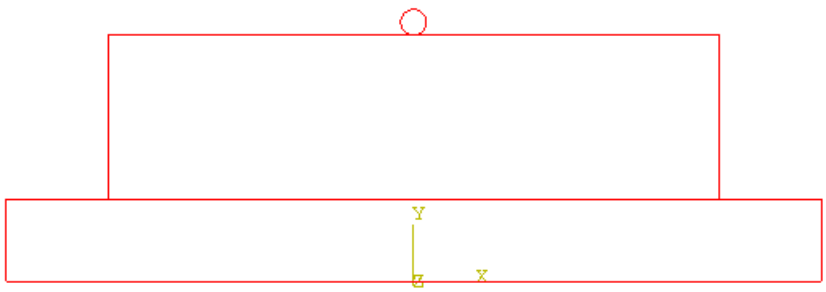

Figure 5.18 The configuration of the 2D glass block subject to impact

From Figure 5.19(a), (b) and (c), stress wave as well as its propagation within the block triggered by the impact of projectile can be seen very clearly. Since the block is thick comparing to the size of projectile, the strength of reflected stress waves are reduced through propagation thus the waves triggered by the impact becomes dominant. Since the stress waves generated by the projectile were too weak to make any horizontal crack when reflected back,

only some local damage within and around the impact area was obtained (Figure 5.19(d)).

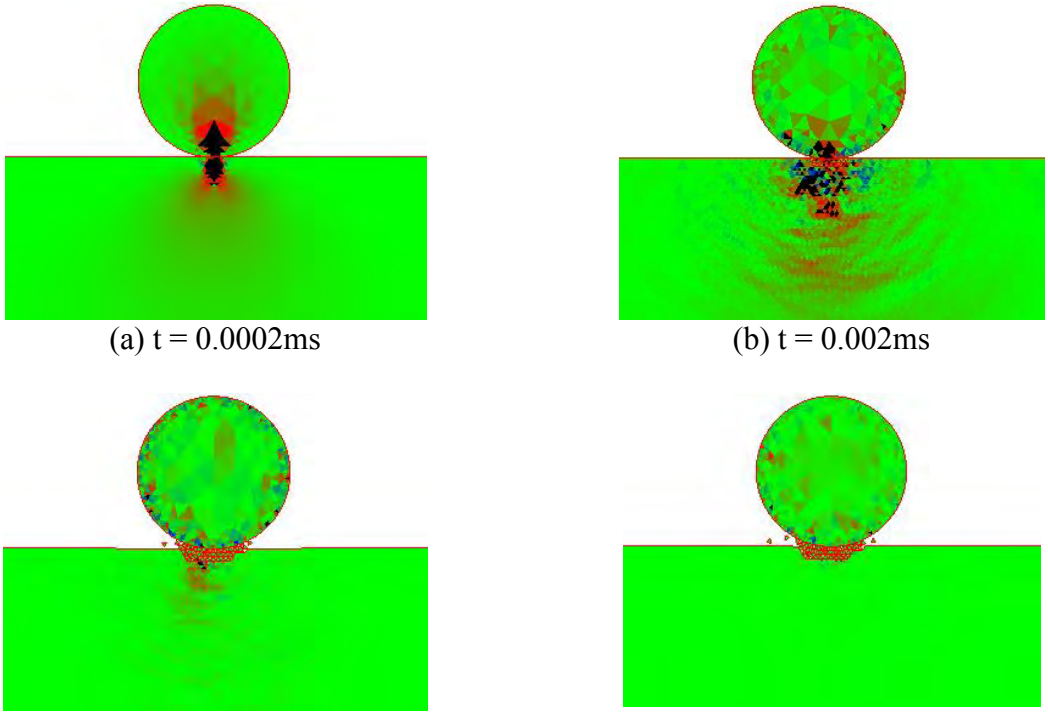

(a) t = 0.0002ms (b) t = 0.002ms

(c) t = 0.015ms (d) t = 0.02ms

Figure 5.19 Stress waves and local damage in a glass block

5.6 Beam Thickness

In this section, the influences of the thickness of beam on the damage responses subject to impact will be investigated. Consider a 1m long glass beam clamped at both sides (no rotation but free movement in horizontal direction) subjected to a 25mm radius steel circle impact, with the velocity of 5.85m/s. The thickness of the beam (h) is varied from 1cm to 5cm. The structural configurations and boundary conditions of this set of beams were given in Figure 5.20.

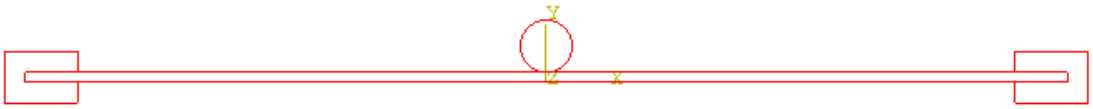

(a) h = 1cm

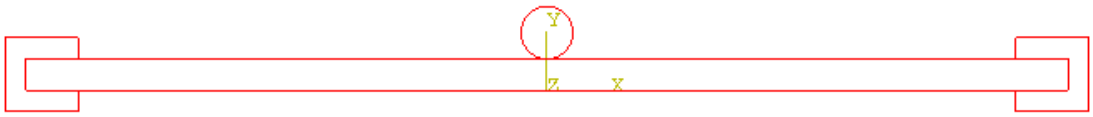

(b) h = 3cm

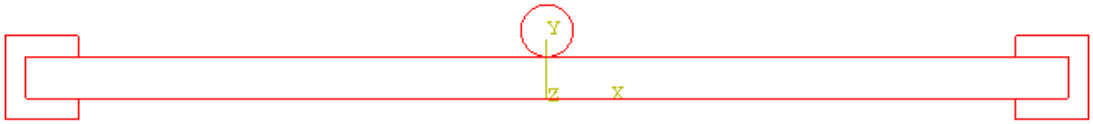

(c) h = 4cm

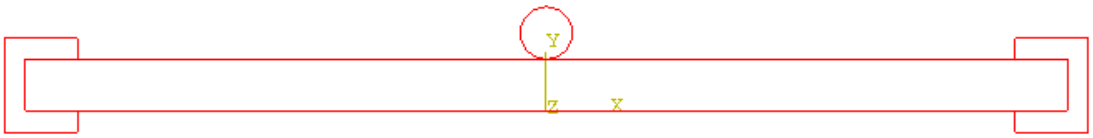

(d) h = 5cm

Figure 5.20 The structural configurations of different thickness beams

And damage responses at t = 0.6 ms were given in Figure 5.21.

(a) h = 1cm

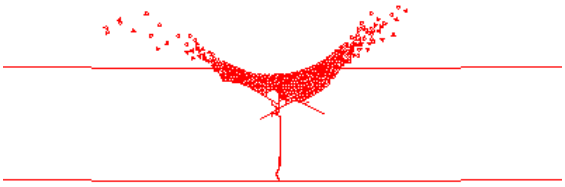

(b) h = 3cm

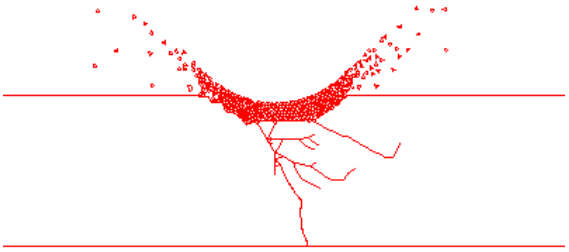

(c) h = 4cm

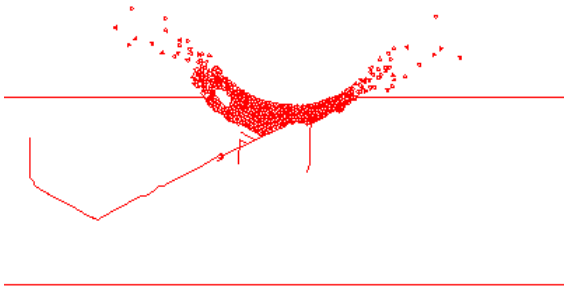

(d) h = 5cm

Figure 5.21 Damage response of beams with different heights at t = 0.6 ms

It can be observed that for beam with small *h*, fracture was thorough and the projectile may penetrate easily (Figure 5.21(a)). With the increase of *h*, it becomes more and more difficult for the projectile to penetrate (Figure 5.21(b), (c) and (d)).

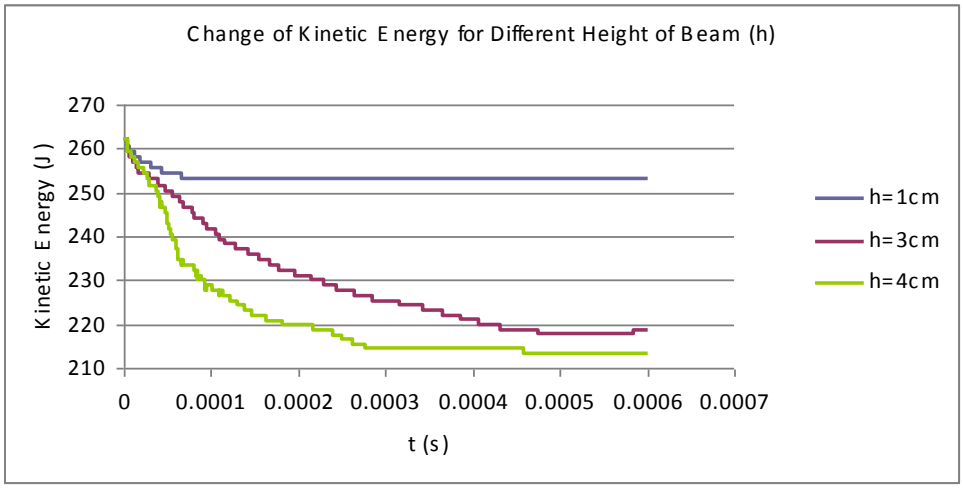

Figure 5.22 The change of kinetic energy for different heights of beams

The total kinetic energy for beams with different *h* has been presented in Figure 5.22. Three beams (*h* =1, 3 and 4cm) were studied and all of them exhibited the energy decay properties. Obviously, for smaller *h*, less kinetic energy was absorbed for the fracture, leaving a considerable amount after damage is completed. On the contrary, beams with *h* = 3 and 4 cm requires a lot of energy for the fracture, regardless of whether the projectile can penetrate the beam or not.

5.7 Projectile

In this section, focus will be given to the projectile size and number. If the density and velocity of projectile is not changed, larger projectile will bring in more kinetic energy, and

results in different damage responses of the glass beam. Meanwhile, multi-projectile impact is also common in engineering and examples in this section demonstrated that each damage crack almost grows independently if projectiles are not too close to each other.

5.7.1 Projectile Size

Consider a 1m long 20mm height beam (same beam and boundary condition from Figure 4.12(a)), impacted by a steel circle of different radiuses (*R*) varied from 5mm to 2cm at the velocity of 5.85m/s. Damage responses at t = 0.6 ms were given in Figure 5.23.

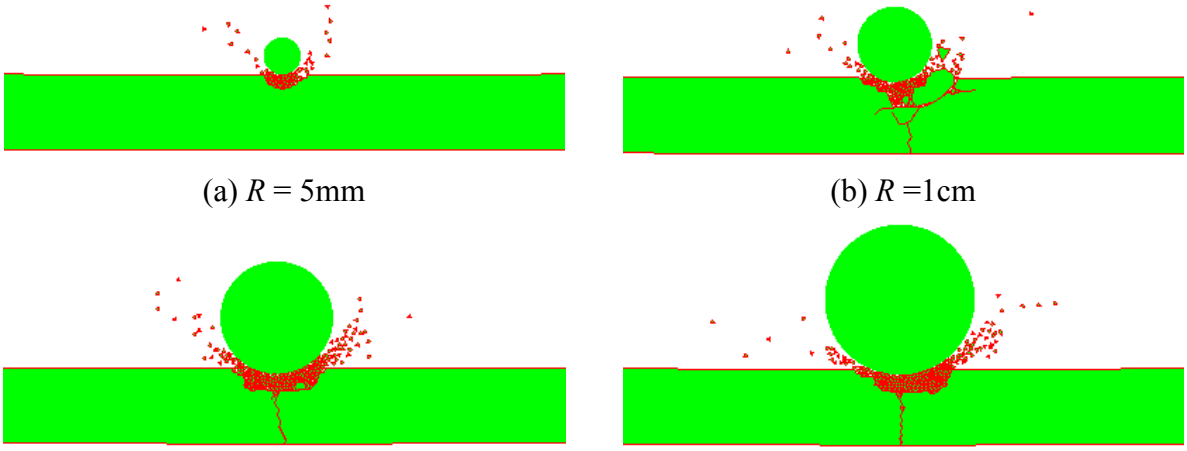

(a) *R* = 5mm (b) *R* =1cm

(c) *R* =1.5 cm (d) *R* = 2cm

Figure 5.23 Damage responses of beams subject impact of different radius of projectile at t = 0.6ms

According to the above figures, apart from Figure 5.23(a), central penetration cracks were obtained. The time when the central crack was formed versus the radius of ball was presented in Figure 5.24. It can be observed that, for the same impact velocity, the larger the size of projectile, the earlier the central crack will be formed. This is quite understandable as more input energy is introduced.

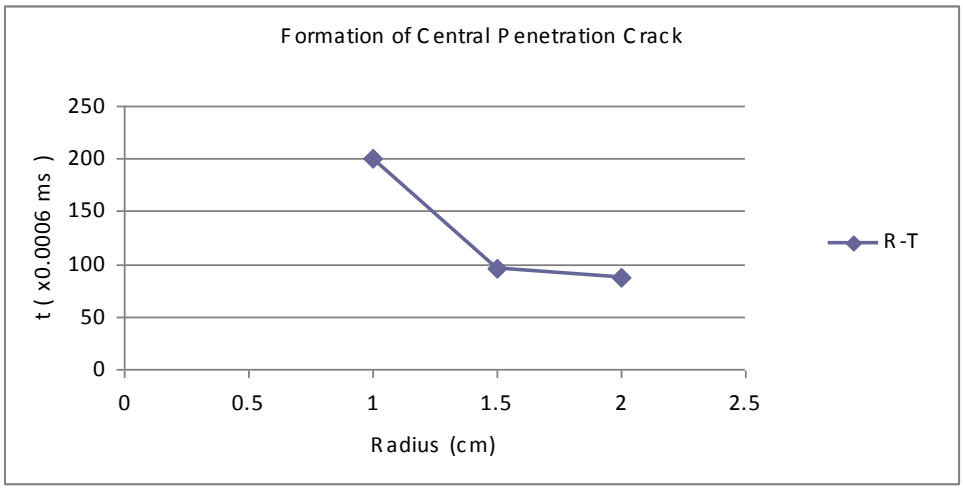

Figure 5.24 The time of the formation of the central crack

Together with the research in section 5.6, conclusions can be reached that for monolithic glass, unless the thickness of beam is very large or the size of projectile is very small or the kinetic energy of the projectile is low, the glass is always easy to be penetrated. The ratio η of the characteristic size of projectile to the beam thickness can be used as an index to estimate the extent of damage. According to figure 5.23, at low velocity impact, if $\eta < 0.5$, the beam may only experience some local damage and will not collapse. Otherwise, complete fracture and central through-thickness cracks seem inevitable.

5.7.2 Multi-Projectile Impact

All the studies presented in the previous sections were based on one projectile only. In this section, multi-projectile impact will be considered. And two steel circles with the radius of 25mm impacting a 2m long 20mm height beam at the velocity of 10m/s will be investigated. The distance between the centres of the two projectiles is 80mm. Structural configurations of

the impact problem as well as the mesh of that two projectiles and beam within the impact effective area were shown in Figure 5.25.

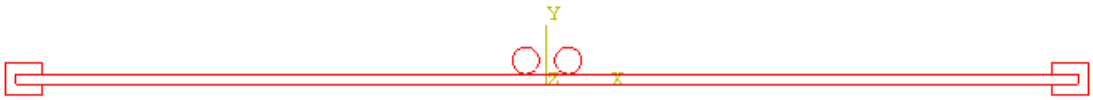

(a) The structural and boundary configuration

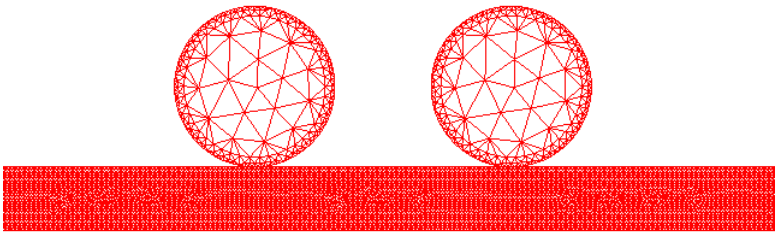

(b) The mesh configuration of the projectile and beam within impact area

Figure 5.25 The structural and mesh configurations of the double ball impact problem

The two projectiles hit the beam at the same time and damage responses at different transient times were given below in Figure 5.26. It can be observed that although there were two projectiles impacted the beam, each projectile generated a cone type crack independently.

(a) t = 0.3 ms

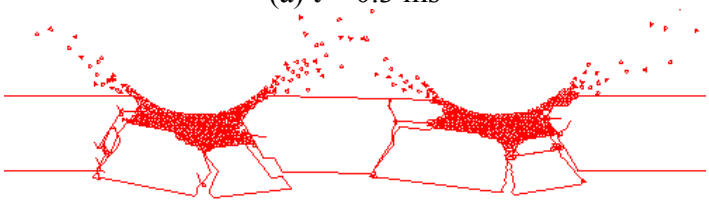

(b) t = 0.6 ms

Figure 5.26 Damage responses of beam subject to two projectile impact at the same time

Keep the impact velocity unaltered, if the projectile on the right is 1.71mm farther away from

the glass than the one on the left (Figure 5.27), the two projectiles will not hit the beam at the same time.

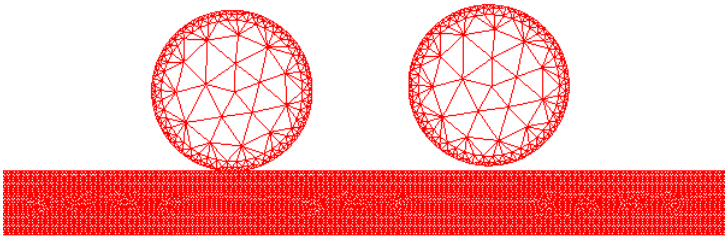

Figure 5.27 The projectile on the right is higher than the left one

The impact velocity is still 10m/s and the damage responses were presented in Figure 5.28. Under this velocity, the right projectile should arrive at the original surface of the beam at t = 0.171ms but only until t = 0.174 ms can some very tiny damage be observed (Figure 5.28(a)) as the beam has undergone some deformation under the impact of the left projectile and is no longer at its original position. This also reflected that FEM/DEM is capable of capturing such small deformation, enabling it stands out of its peers.

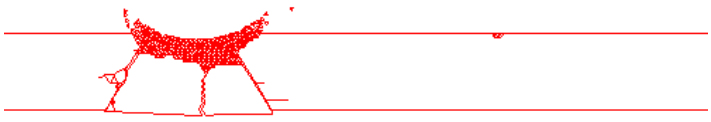

(a) t = 0.174 ms

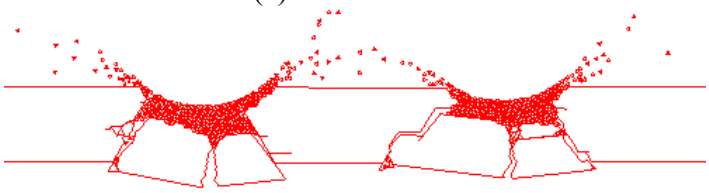

(b) t = 0.6 ms

Figure 5.28 Damage responses of beam subject to two projectile impact not at the same time

According to Figure 5.28, in spite of some tiny change on the shape of the crack, two cone

type cracks were still obtained. Comparing with Figure 5.26, it can be concluded that no matter the two projectiles hit the beam at the same time or not, cracks should be independent if their distance is not too close.

It is worth mentioning that if the two projectiles are very close to each other, the stress fields caused by the two impacts can overlap, which will result in a very complicated stress distribution. And in this case, the damage patterns may not independent any more.

5.8 Summary

This chapter preformed parametric studies over some important factors in the glass impact analysis, and conclusions were reached. Here some key points were summarized and can be used as guidance for the design of monolithic glass structures and components.

(1) As tensile strength and fracture energy are the two most important factors in the fracture model, these two parameters have been examined carefully. As was mentioned previously, higher tensile strength will make glass more difficult to fracture and penetrate while large fracture energy can improve the ductility to resist the brittleness. An ideal approach is to raise both the tensile strength and the fracture energy, and consequently, improving the performance of glass under impact.

(2) Impact velocity is a factor that engineers usually cannot control. It comes directly from the projectile, which is driven by wind (wind-borne debris) or attackers (stones, bullets). Results in this chapter agree well with the common sense that higher impact velocity will definitely

make the glass crack earlier to occur and more sever. On the other hand, oblique impact seems do not have a lot influence on the responses of glass even if the impact angle is less than 45° as the impact perpendicular to the beam is dominant. Since it is difficult to control the impact velocity and angle, the key is still to improve the resistance of glass.

(3) Besides the tensile strength, the thickness of glass (h) is also a crucial factor to resistant the external impact. According to the Euler beam theory, bending stiffness (EI) is quite relevant to the beam thickness:

$$EI = \frac{1}{12} bh^3 \tag{5.3}$$

where b is the width of the beam. Before fracture, h can control the flexural deformation of the beam and at least postpone the occurrence of main central crack. After fracture, large h can help prevent the further damage and penetration (Figure 5.21(d)) while small h can do nothing but leaving sharp shards (Figure 5.21(a)), which will do harm to people.

According to Figure 5.23, increasing the size of projectile has almost an equivalent effect on the damage responses as the thickness of beam did. The essence is the ratio of projectile size to the target height. Since the projectile is beyond the control of engineers, the conclusion can be arrived that if budget permits, increasing the dimension along impact direction (for 2D, beam height; for 3D, plate thickness) is a very feasible approach to resistant the impact.

All the examples above showed the vulnerability of monolithic glass under impact. Large sharp shards are almost inevitable when the impact velocity reaches certain level or the glass thickness is too thin comparing to the projectile size, regardless of the number of projectile or whether they hit simultaneously (Figure 5.26 and 5.28). This vulnerability indicated that a

different type of glass must be applied in important applications for structural purpose, and the laminated glass comes. In the next chapter, this kind of safety glass will be discussed and new fracture models will be developed for it.

MIXED MODE FRACTURE MODEL

6.1 Introduction

This chapter is focused on the mixed mode fracture modelling. Although Mode I fracture is dominant in brittle fracture, mixed mode (I + II) fracture still exists if the glass specimen is under combined tensile and shear loading condition especially when PVB interlayer is incorporated and corresponding model is need to be considered. In this chapter, two mixed mode (I + II) fracture models are developed for glass and laminated glass: the elasto-plastic model and the scaling model. Before modelling, the necessity of mixed mode fracture will be explained and brief literature review is carried out in this section.

6.1.1 The Mixed Mode Fracture

In chapter 4, a crack model based on the Mode I loading conditions was developed for the fracture of glass. According to Elices et al. (2002), as a cohesive model, there are two main drawbacks due to its nature:

(1) The model is realistic enough for monotonically de-cohesion (strain softening) behaviour, implying that unloading and reloading are not considered. Figure 6.1 illustrated that if the separation δ (o or s) is experiencing unloading, i.e. crack closing, the stress may trace back

along the softening curve and be larger than the previous stress level which is physically inadmissible.

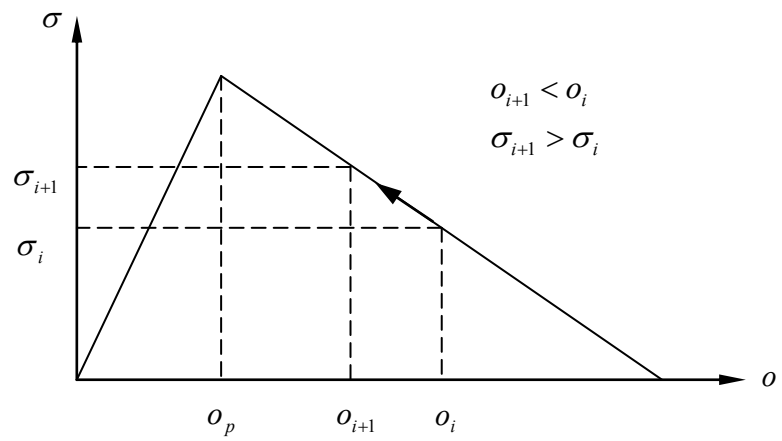

Figure 6.1 Higher stress obtained for unloading condition

(2) The model is developed for Mode I dominant loading condition. Although Mode I fracture is dominant for brittle material, mixed mode fracture may exist in a specific problem (such as a beam with a notch close to the support subjected to impact in the middle, see Figure 6.2). The existence of mixed mode can result in a different direction that cracks may develop along with.

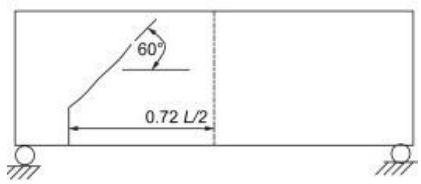

Figure 6.2 A simply supported beam subjected to middle impact with mixed mode fracture at the notch (after Zhang and Chen, 2009)

To avoid these drawbacks, mixed mode (I + II) fracture models for the FEM/DEM program are needed and unloading should also be considered.

6.1.2 Literature Review

There are several theoretical criteria and models developed for predicting fracture behaviour under mixed-mode loading in last century. Erdogan and Sih (1963) introduced the maximum tangential stress (MTS) criterion, which is also called the maximum circumferential stress (MCS) criterion by some other researchers. It assumes that crack will initiate and develop where the tangential/circumferential stress around the crack tip is the maximum. Later, Sih (1974) proposed the minimum strain energy density (MSED) criterion, assuming crack occurs along the direction where the strain energy density is the minimum. Meanwhile, the maximum energy release rate (MERR) criterion was developed by Hussain et al. (1974), Nuismer (1975) and Wu (1978). It is based on and extended from the classic Griffith's (1920) theory.

These models are prevalent in investigating the fracture of engineering materials under mixed mode loading. However, Ayatollahi and Aliha (2009) pointed out that for mixed mode fracture toughness of soda lime glass, values from these models are usually underestimated comparing with the experimental data.

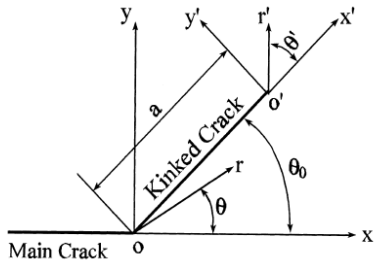

Figure 6.3 The main crack, kinked crack and coordinate systems (after Sutton et al. (2000))

In 2000, the crack tip opening displacement (CTOD) criterion was developed by Sutton et al. It assumes that crack will occur when CTOD reaches a critical level and is capable of analysing the kinking in arbitrary direction (Figure 6.3). Similarly to the MTS criterion, a generalised maximum tensile stress that taking the *T*-stress (stress parallel to the crack) into account was established by Smith et al. (2001). Yosibash et al. (2006) presented a failure criterion for brittle elastic material under mixed-mode loading extended from the failure criterion of Leguillon (Leguillon, 2002; Leguillon et al, 2003) but with emphasis on the PMMA (Polymethyl Methacrylate), which was often used as a lightweight and shatter-resistant alternative to glass) and ceramic V-notched specimens. Also, Chang et al. (2006) developed a general mixed-mode state (including mode I, II and III) for brittle cracked materials.

The failure behaviour between dissimilar materials (interface) under mixed mode conditions also has drawn attention from researchers. Ikeda et al. (1998) investigated the fracture mechanics of interface cracks between various dissimilar materials and presented the application of mixed-mode fracture toughness criterion. In their research, a stress intensity

factor approach was used and specimens were tested to verify the proposed model. Morais and Pereira (2006) conducted an analytical study on mixed mode bending of glass/epoxy laminates.

Although the fracture theories and criteria for mixed mode loading have been proposed from time to time, not many were well-established. Some of them are focused on some specific material (like concrete), others may be applicable to certain particular configurations and loading conditions. Modern development of glass and laminated glass structure requires new development or modification of failure criterion.

6.1.3 Layout of Chapter

Besides introduction, there are two independent sections proposing the two new mixed mode fracture models: the elasto-plastic damage model in section 6.2 and the scaling model in section 6.3. Each section contains essential derivation of the model followed with numerical examples and discussions.

The laminated glass is discussed and numerical examples are shown in section 6.4. The elasto-plastic fracture model will be used in the analysis, showing the advantage in energy absorption over the monolithic glass. And conclusions are also reached in the summary section at the end of this chapter.

6.2 Mixed Mode (I + II) Elastic-Plastic Fracture Model

In this section, mixed-mode (I + II) elasto-plastic fracture was developed. This model considered both Mode I and II into the fracture behaviour and unloading was taken into account. The model developed in this section is not only suitable for the fracture of monolithic glass as it can well adapt to problems which are Mode I dominant, but also can be employed for simulating the interface between glass and interlayer in laminated glass where mixed-mode loading may occur.

Before describing the model, literature on general elasto-plastic theory were briefly reviewed. Later, the main idea of the elasto-plastic fracture model was described, followed by numerical examples, completed with comparison and discussions.

6.2.1 Literature Review

Elasto-plasticity is widely known and used (Celik, 2001; Tian et al., 2009; Zhou and Zhu, 2010) in the brittle and ductile materials. As its name suggested, elasto-plastic theories postulate that deformation is composed of both elastic and plastic parts. The basic formulation of elasto-plastic and the concept of yield surface were introduced in many researchers' work, like Crisfield (1991). Based on these ideas, some elasto-plastic numerical models and

solutions were established.

In late 1960s, Zienkiewicz et al. (1969) studied the elasto-plastic approach to solve the plates containing perforation and notch. Ju (1989) introduced his coupled elasto-plastic theory and discussed its use in constitutive modelling. Jong et al. (1997) proposed an FEM approach for elasto-plastic damage based on anisotropic ductile materials. With the development of laminated and composite material, the constitutive relation was studied by many researchers (Park and Voyiadjis, 1997; Hayakawa et al., 1998; Tian et al, 2009) and achieved great progress. The elasto-plastic damage theories developed gradually, however, majority of them are emphasised on ductile materials.

Apart from the ductile materials, another area that elasto-plastic model is frequently used is concrete and concrete-like quasi-brittle materials. Bažant and Kim (1979) developed the elasto-plastic fracture theory for concrete based on the pioneering work of Dougill (1976). Later on, Simo and Ju (1987) employed an elasto-plastic damage theory to describe the material behaviour of concrete. The stiffness tensor was used as an internal variable in their work. Krätzig and Pölling (1998) compared the previously mentioned theories and proposed a new one for concrete under predominate compression, which demonstrated that elasto-plastic is not only valid in stretching but also in compression. Recently, the elasto-plastic model has been extended to the damage of concrete under high temperature (Nechnech et al., 2002).

Literatures of elasto-plastic model for glass are rare as its elasto-plastic behaviour may not as obvious as that of ductile and quasi-brittle materials. According to its general definition, since the total strain $\varepsilon = \varepsilon(elastic) + \varepsilon(plastic)$, the main task of a classical elasto-plastic model is to differentiate the elastic and plastic portions separately from the total strain by using a yield surface. Based on this idea, elasto-plastic approach similar to quasi-brittle material, such as concrete, can be extended to glass.

6.2.2 Model Description

The main idea of this model is the use of an elliptical yield/failure surface F (Figure 6.4), which has been defined by equation 6.1.

$$F = \left(\frac{\sigma_n / \sigma_{ult}}{f_1(\bar{d})} \right)^2 + \left(\frac{\tau / \tau_{ult}}{f_2(\bar{d})} \right)^2 - 1 \tag{6.1}$$

where $f_1(\bar{d})$ and $f_2(\bar{d})$ are the strain softening curves for Mode I and II fracture separately and $\bar{d}$ is the current damage index defined by Munjiza (2004). For simplicity, we assume $f_1(\bar{d}) = f_2(\bar{d}) = 1 - \bar{d}$, implying both mode I and II share the same linear descending curve. σ_{ult} and τ_{ult} equal to the ultimate tensile and shear strength f_t and f_s of the material respectively.

The stress starts from their initial intact surface F_0 and approaches zero with the increase of damage index $\bar{d}$. A possible path for the stress state was illustrated in Figure 6.4, it varied

from yield surface F_0 to F_1, then to F_2 and finally arrived at the origin. Since the same fracture index $\bar{d}$ was used for both opening $f_1(\bar{d})$ and sliding $f_2(\bar{d})$, the yield surfaces are similar in shape to each other. According to equation 6.1, the position and shape of the elliptical surfaces are updated by the fracture index $\bar{d}$ at each time step.

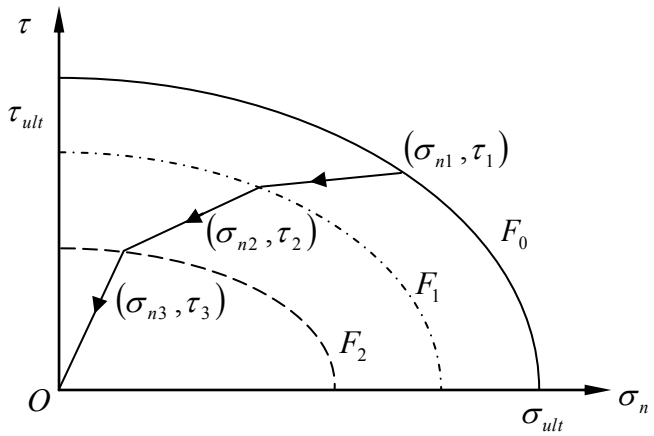

Figure 6.4 The elliptical yield surfaces and a possible stress path for softening

To perform the elasto-plastic model, the stress $\sigma_i = (\sigma_{ni}, \tau_i)$ and the deformation $\delta_i = (o_i, s_i)$ of the previous time step of each joint need to be stored. After obtaining the current deformation $\delta_{i+1} = (o_{i+1}, s_{i+1})$, the deformation increment can be calculated. Provided that the increment is a small value along each time step, we have:

$$d\varepsilon = \frac{\delta_{i+1} - \delta_i}{\delta_{\max}} \tag{6.2}$$

Use the elastic relation, the trial increment of stress can be obtained according to equation 6.3,

$$\begin{Bmatrix} \Delta\sigma_n \\ \Delta\tau \end{Bmatrix}^{trial} = D_e \, d\varepsilon \tag{6.3}$$

where D_e is the decoupled elastic matrix expressed in equation (6.4) with o_p and s_p

represent for the elastic limit of opening and sliding, respectively.

$$D_e = \begin{bmatrix} \frac{f_t}{o_p} & 0 \\ 0 & \frac{f_s}{s_p} \end{bmatrix} \tag{6.4}$$

If the new stress state $\left(\sigma_{ni} + \Delta\sigma_n^{trial}, \tau_i + \Delta\tau^{trial}\right)$ is within the yield surface ($F \le 0$) then it will be the genuine one. Otherwise ($F > 0$), the elasto-plastic stress beyond the yield surface can be reached by equation 6.5.

$$\begin{bmatrix} \Delta\sigma_n \\ \Delta\tau \end{bmatrix}^{elasto-plastic} = D_{ep}(1-\lambda)d\varepsilon \tag{6.5}$$

where $0 < \lambda < 1$ and it is used to tell the strain within and beyond the current yield surface (Figure 6.5).

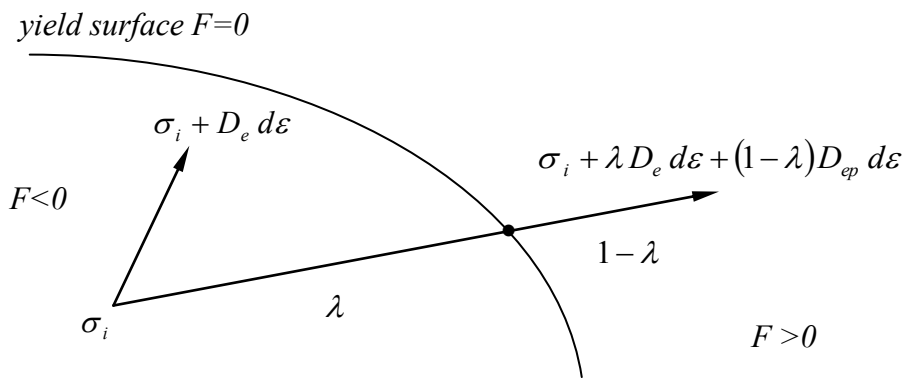

Figure 6.5 The stress calculation of the elasto-plastic model

D_{ep} is the elasto-plastic matrix which can be expressed in the following equation 6.6.

$$D_{ep} = D_e - \frac{D_e n_g n^T D_e}{H + n^T D_e n_g} \tag{6.6}$$

with associated plasticity $n_g = n = \frac{\partial F}{\partial \sigma}\left|\frac{\partial F}{\partial \sigma}\right|^{-1}$, H is the hardening modulus which is a scalar and $H = -\left(\left|\frac{\partial F}{\partial \sigma}\right|^2\right)^{-1}\left(\frac{\partial F}{\partial \bar{d}}\frac{\partial \bar{d}}{\partial \varepsilon_{p1}}, \frac{\partial F}{\partial \bar{d}}\frac{\partial \bar{d}}{\partial \varepsilon_{p2}}\right)\left(\frac{\partial F}{\partial \sigma}\right)$. So the stress for the next time step $\sigma_{i+1} = \sigma_i + \lambda D_e\, d\varepsilon + (1-\lambda) D_{ep}\, d\varepsilon$ can be obtained.

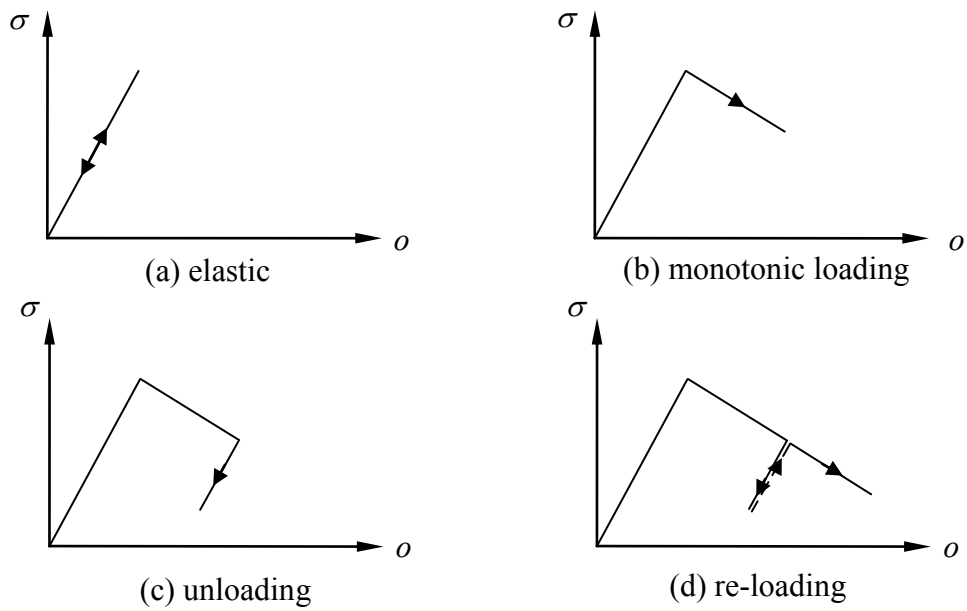

Figure 6.6 The stress path under variable conditions in elasto-plastic model

By using the elasto-plastic model, unloading can be considered in strain softening period. Take the example of normal stress σ and opening o, Figure 6.6 demonstrated the path that stress may experience under variable conditions. When the opening is smaller than the elastic limit, loading and unloading are travelling along the unique elastic path in Figure 6.6(a). After σ reaches the tensile strength, situation becomes complicated. If loading i.e. opening increases, continues, Figure 6.6(b) applies. If unloading occurs, the stress will decrease

parallel to the elastic hardening curve in Figure 6.6(c). Figure 6.6(d) represents the condition of reloading, pushing the stress back to the strain softening curve then decrease along it.

In addition, both opening and sliding as well as their damage index $f_1(\bar{d})$ and $f_2(\bar{d})$ are considered in the yield surface F. Further, the elasto-plastic matrix D_{ep} is also combined with F. These features enable both Mode I and II to be considered together and mixed-mode fracture is achieved.

6.2.3 Numerical Examples

1. Comparison with the Mode I model of the impact analysis on a glass beam

Consider a monolithic glass beam with the same structure and mesh configuration as the example in section 4.5.1. The beam is subjected to the impact of a steel ball with the radius of 25mm at the velocity of 8m/s so that results from the elasto-plastic model can be compared with that obtained from the Mode I model in chapter 5. Material properties are the same as listed in Table 4.1.

t = 0.006 ms

t = 0.06 ms

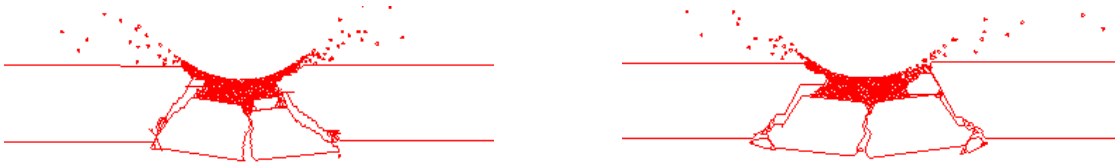

t = 0.6 ms

(a) Elasto-plastic damage model (b) Mode I fracture model

Figure 6.7 Comparison between elasto-plastic model and the original fracture model

Transient responses at the early stage of impact were presented in Figure 6.7, showing the damage initation and propagation process with the time step of 0.0002 μs . Both the responses of the elasto-plastic and Mode I fracture model (from chapter 4) were given for comparision.

For both models, damage started from the local contact area and a horizontal crack can be obtained. It can be observed from Figure 6.7 that by using the elasto-plastic model, a Hertzian type cone crack similar to the Mode I model was obtained. The cone was formed quickly at about t = 0.06 ms and there is no major change to the formation of the cone afterwards.

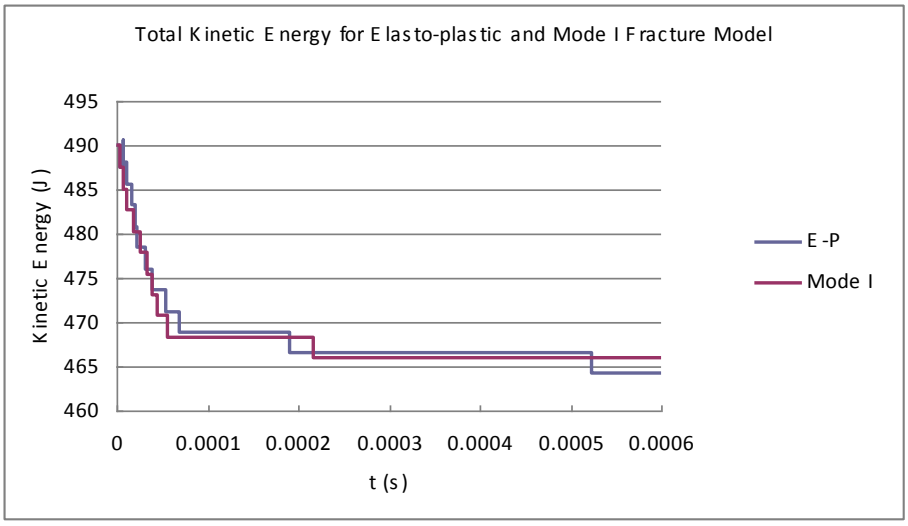

Figure 6.8 Total kinetic energy for elasto-plastic and Mode I fracture model

The elasto-plastic model achieved the similar results that Mode I model did. The evolution of total kinetic energy (J) of both the elasto-plastic model and the Mode I fracture model was showed in Figure 6.8. Just before 0.2 ms, the two curves are almost identical. After that, they are still very close. It also can be observed that the elasto-plastic model exhibits good energy decay property and convergence after the cracks have completed.

2. In-plane shear loading on a glass block

Consider a 100x100mm rectangular glass block bounded in a rigid steel channel, subjected to the impact of two steel square projectiles sized 10x10mm, so that in-plane shear loading was applied onto the glass block. The square projectiles hit the glass at a fixed velocity of 1m/s above and below the specimen separately. The horizontal distance between the two projectiles is 70mm and this is a Mode II dominant problem before the specimen undergoing severe damage. The structural and mesh configurations were schematically shown in Figure 6.9(a). Accordingly, damage response of the specimen at t = 1ms was given by Figure 6.9(b).

As can be seen, a classical shear crack was obtained in Figure 6.9(b) at the right top of the specimen. The crack angled 26° to the horizontal direction with some small branches. Meanwhile, some fragments caused by impact were obtained around the impact area. In this problem, Mode II definitely exists at early loading stage. As time elapsed, more and more

fragments will be created by the projectiles, resulting in a very complex stress state which is not Mode II dominant any more.

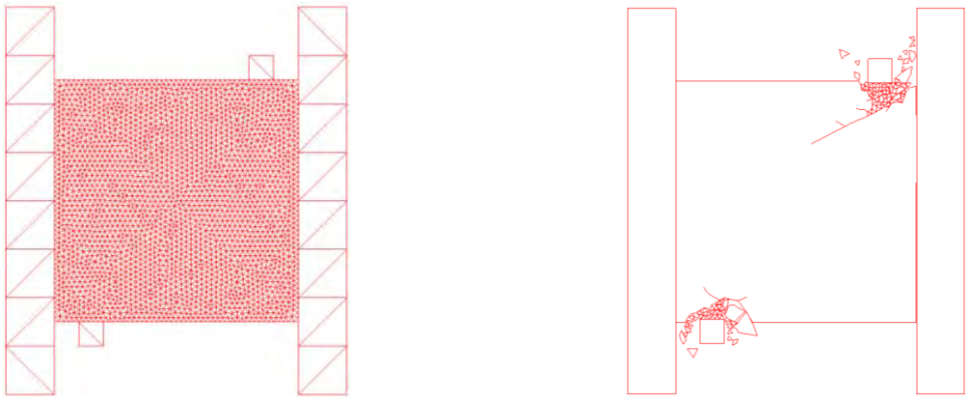

(a) Structure and mesh configurations (b) Damage response at t = 1ms

Figure 6.9 Rectangular glass block subject to in-plane shearing loading

Figure 6.10 illustrated the damage response using the Mode I fracture model. Comparing with results from the elasto-plastic model, there is no dominant oblique crack propagated from the right top impact point.

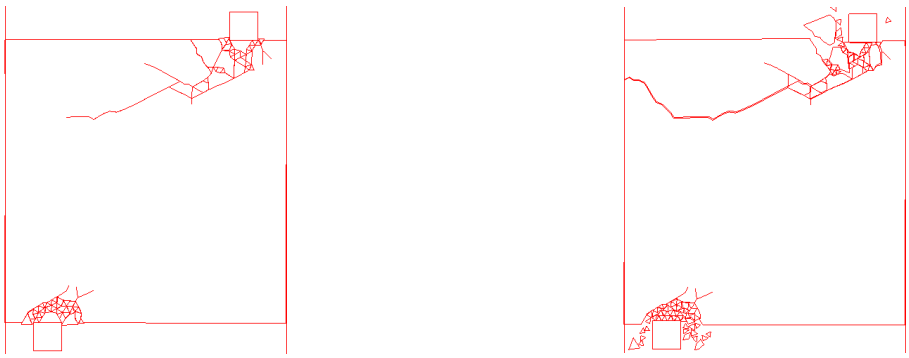

(a) t = 0.1ms (b) t = 1ms

Figure 6.10 the development of damage response using the Mode I fracture model

The examples of in-plane shear loading showed that despite some detailed differences on crack propagation, the result obtained using the elasto-plastic fracture model is largely similar to that of the Mode I fracture model. The reason of this similarity will be discussed later in section 6.2.4.

3. Unaxial compression on glass block

Shen et al. (1995) conducted a series of uniaxial compression test on gypsum with pre-existing flaws to study the failure mechanism of fractured rock mass. The test configuration was adopted to investigate the behaviour of glass under shearing and mixed loading condition.

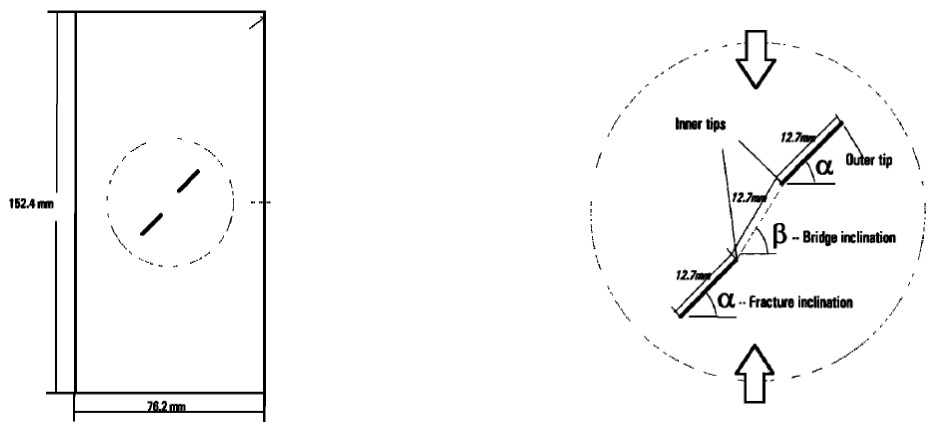

(a) The entire specimen (b) Details of pre-existing fractures

Figure 6.11 The geometry of specimen and pre-existing cracks (after Shen et al. (1995))

Figure 6.11 presented the test specimen, which is 76.2mm wide and 152.4mm high, with two parallel and offset pre-existing cracks in the middle. The two cracks are of 12.7mm long and at an angle (α/β) (Figure 6.11b) to the horizon. Here two sets of angles were considered, ($45^\circ/45^\circ$) and ($45^\circ/90^\circ$). The angles were such chosen that the specimen is under typical shearing ($45^\circ/45^\circ$) and shearing plus tension loading ($45^\circ/90^\circ$) near the pre-existing crack area.

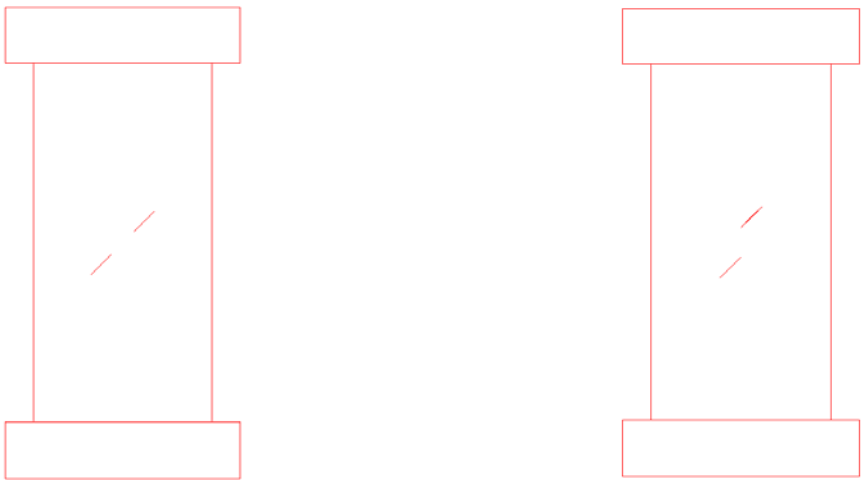

(a) $45^\circ/45^\circ$ (b) $45^\circ/90^\circ$

Figure 6.12 The configuration of uniaxial compression in FEM/DEM

In the FEM/DEM elasto-plastic simulation (Figure 6.12), the compression was achieved by fixing the rate of two steel block at 0.01m/s at each way and transient responses of specimen with (α/β)=($45^\circ/45^\circ$) and (α/β)=($45^\circ/90^\circ$) were given in Figure 6.13 and 6.14.

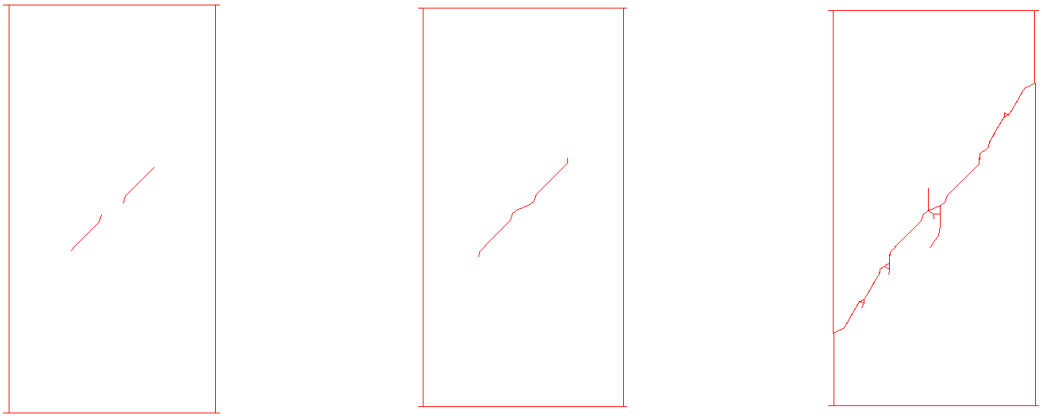

(a) t = 0.85ms (b) t = 0.925ms (c) t = 1.05ms

Figure 6.13 The development of cracks in specimen with $45^\circ/45^\circ$ cracks using the elasto-plastic fracture model

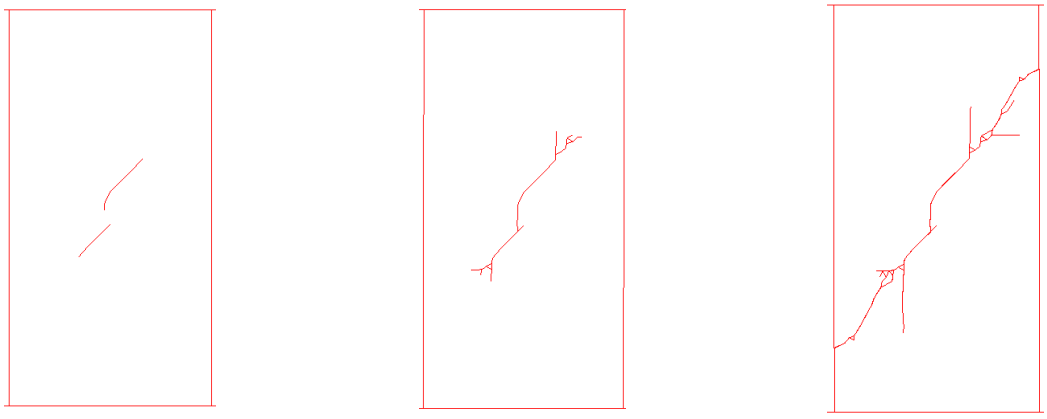

(a) t = 0.9ms (b) t = 1ms (c) t = 1.1ms

Figure 6.14 The development of cracks in specimen with $45^\circ/90^\circ$ cracks using the elasto-plastic fracture model

According to Figure 6.13 and 6.14, a crack that bridged the two pre-existing flaws was developed first in the middle of the specimen, followed by some branches at the other side of the pre-existing cracks away from the centre. Figure 6.15 showed the experimental observation from Shen et al. (1995). It can be concluded that although the results from the

FEM/DEM is not exactly the same as the experimental data (possibly due to material properties, loading rates and etc), the general damage patterns match each other well.

(a) $45^\circ / 45^\circ$ (b) $45^\circ / 90^\circ$

Figure 6.15 The experimental observation from Shen et al. (1995)

The numerical examples given in this section demonstrated that the developed elasto-plastic model is capable of simulating Mode I, II and mixed mode problems.

6.2.4 Discussions and Conclusions

According to Figure 6.7 and 6.8, the results generated by the elasto-plastic model and the Mode I fracture model are similar in crack shape and change of the total kinetic energy. These phenomena imply that for glass impact problem studied in this section, Mode I is dominant and is more important.

Actually, many research supported this point of view. Rao et al., (2003) pointed out that for brittle material, the critical Mode I stress intensity factor (K_{Ic}) is always smaller than that

(K_{IIc}) of Mode II ($K_{Ic} < K_{IIc}$). And under tensile, shear, tension- and compression-shear loading, the maximum Mode I stress intensity factor $K_{I\max}$ is always larger than its counterpart $K_{II\max}$. Therefore the $K_{I\max}$ reaches K_{Ic} before $K_{II\max}$ reaches K_{IIc}, making the Mode I fracture almost inevitable. Flocker and Dharani (1997b) also asserted that the maximum principal tensile stress is of primary concern since it corresponds to a Mode I crack, which suggested the importance of Mode I fracture.

Melin (1986) agreed that normal tensile stress is the only driving force for crack propagation. Research on the Mode II crack (see e.g. Lajtai, 1974; Melin, 1986, 1987) concluded that its growth can be promoted under a high confining pressure situation, and this statement was further supported by Zhao et al. (2006). But the so called “high confining pressure” is not available in ordinary glass (either beams or plates) impact problems.

Consequently, from the theoretical fracture mechanics side, the critical Mode II stress intensity factor K_{IIc} would not be reached before the Mode I fracture occur; and practically the condition that is Mode II prone is not available for the glass impact problems. Thus in the glass impact analysis, Mode I is dominant.

However, the statement that Mode I is dominant does not mean the shear stress has little effect on the response of glass. If the relative strength i.e. the long and short axis of the elliptical yield surface in Figure 6.4 be interchanged, three possibilities may result as shown in Figure

6.16. For tensile strength (f_t) larger than the shear stress (f_s), an ordinary shallow elliptical yield surface can be obtained (Figure 6.16a); for $f_t = f_s$, the surface is a circle (Figure 6.16b); for $f_t < f_s$, we have an reversed shallow ellipse.

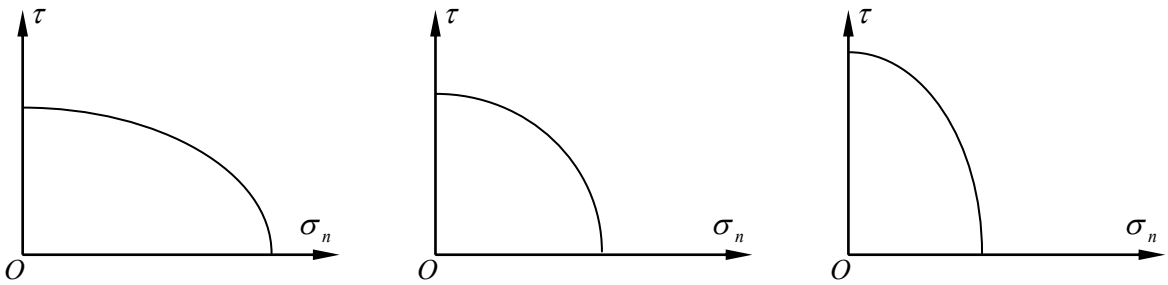

(a) $f_t > f_s$ (b) $f_t = f_s$ (c) $f_t < f_s$

Figure 6.16 The three shapes of the elliptical yield surface

If we keep either f_t or f_s constant, by changing the other strength will result in one of the three possibilities for the shape of the yield surface. In the following consideration, firstly, the f_t was fixed at 30MPa, with f_s increasing gradually from 15MPa to 60MPa. Figure 6.17 showed the damage response for different combinations of f_t and f_s.

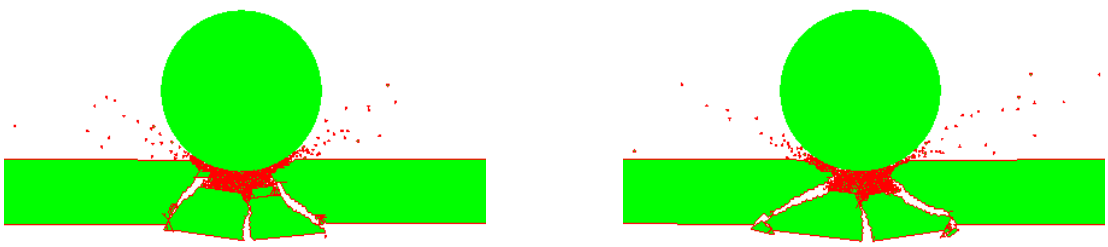

(a) $f_t : f_s = 2$ (b) $f_t : f_s = 1.5$

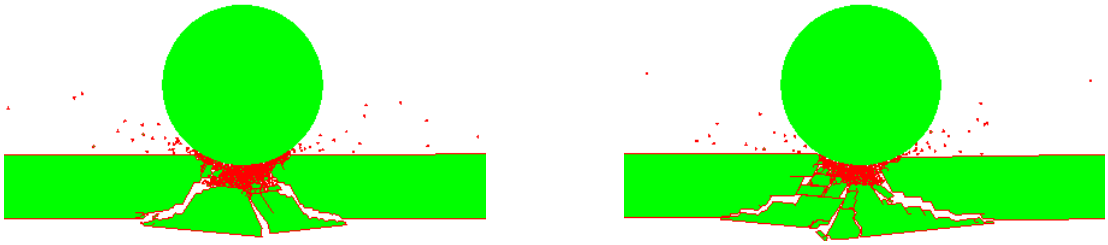

(c) $f_t : f_s = 1$ (d) $f_t : f_s = 0.5$

Figure 6.17 The damage response under different f_s with $f_t = 30\,\text{MPa}$ at t = 0.6ms

Figure 6.17(a) showed the original response that has been studied in section 6.2.3. With the increase of f_s, the damage area has been enlarged along with the increase of the crack angle to the load axis. According to Figure 6.17, more shear stress was taken since the shear strength was increased, making the cracks tended to propagate perpendicular to the load direction.

Now with f_s fixed at 30MPa, the value of f_t is increased gradually from 15MPa to 60MPa. The damage responses were shown in Figure 6.18, with the intermediate situation of $f_t = f_s$ shown in Figure 6.17(c).

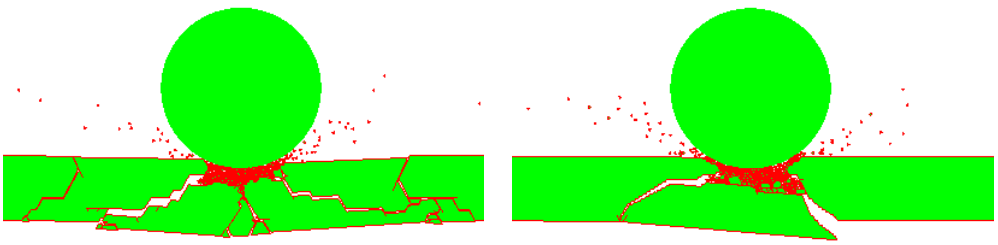

(a) $f_t : f_s = 0.5$ (b) $f_t : f_s = 2$

Figure 6.18 The damage response under different f_t with $f_s = 30\text{MPa}$ at t = 0.6ms

By observing the change of damage responses with f_t from 15MPa to 60MPa, the damaged area quickly got smaller. In Figure 6.18(a), the glass experience not only a cone but also bending not far away from the centre since the tensile strength is small. With the increase of tensile strength, the behaviour becomes more brittle, which is consistent with the conclusions drawn in chapter 5.

By comparing Figure 6.17 and 6.18, the change of the tensile strength results in a more dramatic change in the damage response than the shear strength did. This also demonstrated that the tensile failure (Mode I) is more important than shear failure (Mode II) in glass impact analysis.

Should some of the figures be selected from Figure 6.17 and 6.18 and re-arranged in Figure 6.19, the relationship between the ellipse shape and damage responses can be extracted. For the shallow elliptical yield surface (Figure 6.19a), the damage is usually an ordinary cone, extending smoothly with an angle from the load axis; on the contrary, the damage will tended to propagate perpendicular to the load direction, where the shear effect be enhanced.

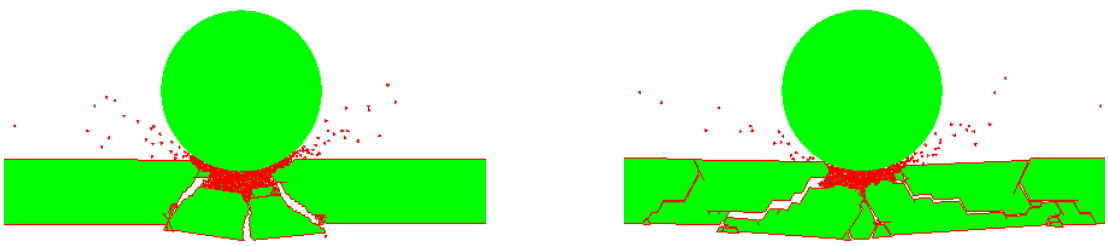

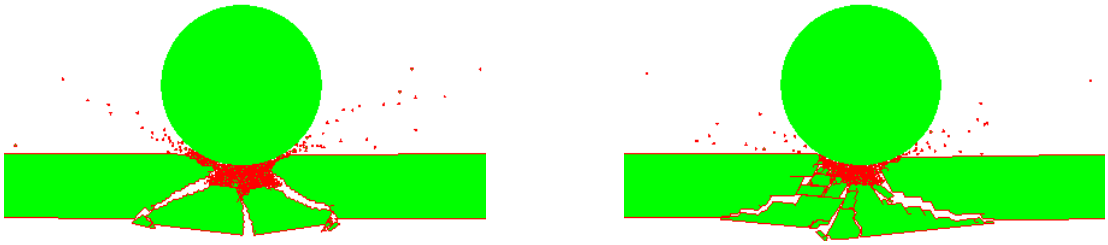

(a) $f_t : f_s > 1$ (b) $f_t : f_s < 1$

Figure 6.19 The relationship between the ellipse shape and damage responses

The study and discussion in this section demonstrated from both theoretical and numerical aspects that for glass impact analysis that Mode I is much more important than Mode II. Based on this assertion, the similarity between the results from both elasto-plastic model and the Mode I fracture model is reasonable and acceptable. The study on the shape of the elliptical yield surface revealed the possible damage patterns upon different combinations of f_t and f_s, giving a qualitative judgement before the actual simulation.

6.3 Mixed Mode (I + II) Scaling Model

In this section, scaling (or reduction) model will be discussed. The key of this model is the obtaining of a scaling factor based on the ultimate damage envelop and the current deformation, thus reduced stress state for current time step can be obtained. Since both opening and sliding are involved in the damage envelop, mixed-mode is likely to be taken into account. It is worth mentioning that the terminology “scaling factor” in this context is not a scalar parameter used by simple damage models (both isotropic and anisotropic). A scalar

parameter in simple damage models is used to evaluate the decrease of the initial stiffness (Jirásek, 2006, 2011) during damage process, while the scaling factor in this section does not change the material stiffness (which is equivalent to the slope of a constitutive curve), but affects the level of stress instead.

6.3.1 Model Description

The scaling model is based on the scaling of the strain softening curves to determine the current stress state. The triggering of scaling model relies on a detection function *T*, where *T* is expressed in equation 6.7:

$$T = \sqrt{\left(\frac{o}{o_p}\right)^2 + \left(\frac{sabs}{s_p}\right)^2} \tag{6.7}$$

Same as in the elasto-plastic model, o_p and s_p stand for the elastic limit of opening and sliding. To avoid unrealistic enlargement of *T*, for $o < 0$, o is taken as zero.

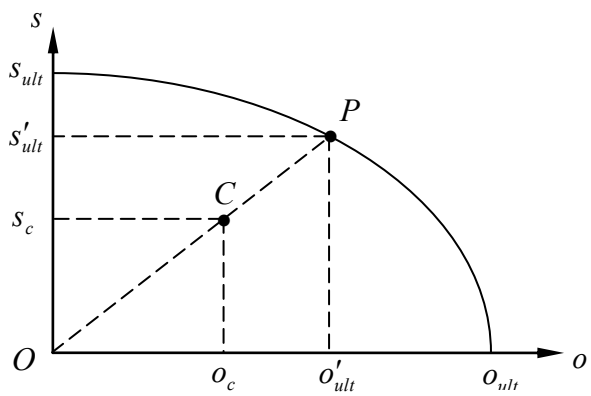

Figure 6.20 Determining new ultimate opening (*o*) and sliding (*s*) in scaling model

Figure 6.20 illustrated how to determine the new ultimate o and s in scaling model. The maximum damage envelope is defined by equation 6.8:

$$\left(\frac{o}{o_{ult}}\right)^2 + \left(\frac{s}{s_{ult}}\right)^2 = 1 \tag{6.8}$$

This elliptical envelope is fixed and its shape depends on the critical opening and sliding distance. It is the envelope that ensures all the separation exceeding it will result in complete damage and no future calculation for stress will be needed.

Suppose point C is the current state of separation (o_c, s_c) obtained initially from the FEM/DEM program by calculating integration points. Connect the origin O and point C and extend the line until it meets the damage envelope at point P. The coordinates of point P represents the reduced new ultimate separation o'_{ult} and s'_{ult}.

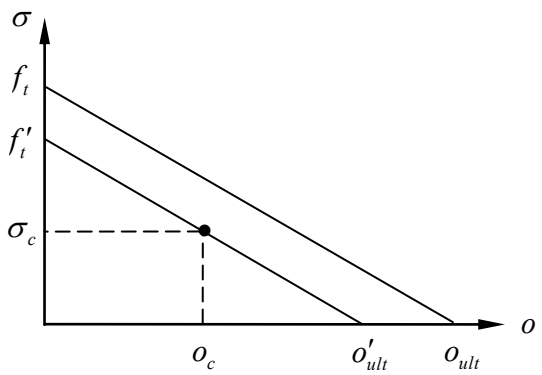

Figure 6.21 Mapping the current separation onto scaled strain softening curve

Take the normal bonding stresses for example, the ratio of $\frac{o'_{ult}}{o_{ult}}$ is used to scale the original strain softening descending curve and this process was schematically shown in Figure 6.21. The genuine tensile stress σ_c can be obtained by mapping the current o_c onto the scaled strain softening curve. Same approach can be applied to determine the tangential stress τ_c.

The main idea of this model is to obtain a scaling factor from the damage envelop to reduce the original strain softening curve, then genuine stress can be reached by mapping the current separation onto the reduced strain softening curve. The shape of the strain softening curve is not change but only scaled by the scaling factor, thus this model is universal and can be used for the strain softening curves of any shape.

It is worth mentioning that since both *o* and *s* are considered in the damage envelop, mixed property can be exhibited. However, the final stress is obtained by mapping the distance onto the scaled strain softening curves separately, so the tension and shearing are not heavily coupled and unloading is not considered either.

6.3.2 Discussions and Numerical Examples

In this section, the scaling model will be further investigated along with numerical examples. Some features of this model together with the corresponding response in simulation will be

discussed, and the shortcoming of this model will be discussed as well.

By using a scaling factor, a reduced strain-softening curve was obtained from this model. Since the area between the axis and the descending curve equals to the fracture energy, the actual value of this energy used in the analysis becomes un-physically smaller. This reduced fracture energy results in a less amount of energy that needed for the fracture process in comparison with the Mode I model.

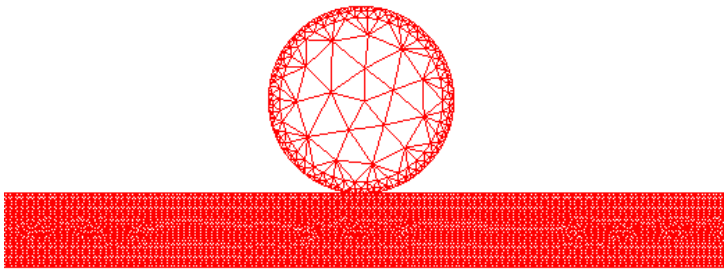

Figure 6.22 Mesh configurations of impact area and projectile

To verify the above-mentioned statement, consider a 2m long 20mm high glass beam (same structural configuration as in section 4.5.1) clamped at both ends. The beam was subjected to the impact of a 25mm radius steel ball at the velocity of 5.85m/s. Mesh configurations of the impact area of beam and projectile were shown in Figure 6.22.

The transient responses by using the scaling model were given in the Figure 6.23 and it can be observed that a cone-like crack pattern was obtained early at t = 0.12 ms. Although the cone shape is not as same as the one from Mode I crack model, they were generated at almost the

same time around t = 0.1 ms.

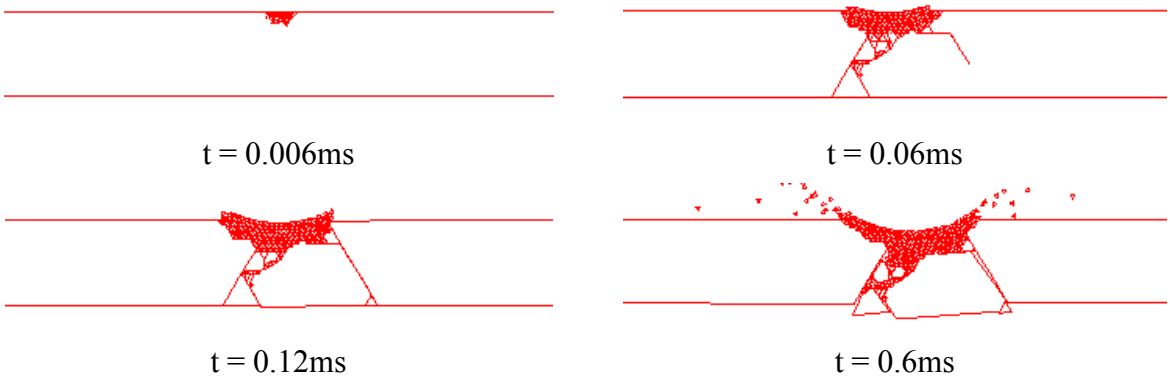

Figure 6.23 The transient damage response of glass using scaling crack model

Figure 6.24 schematically showed the decay curve of the total kinetic energy for both Mode I and scaling model. Since the scaling model was directly reduced from the Mode I softening curve proposed in chapter 4, they share the same shape of descending and the comparison between them is thus highly correlated.

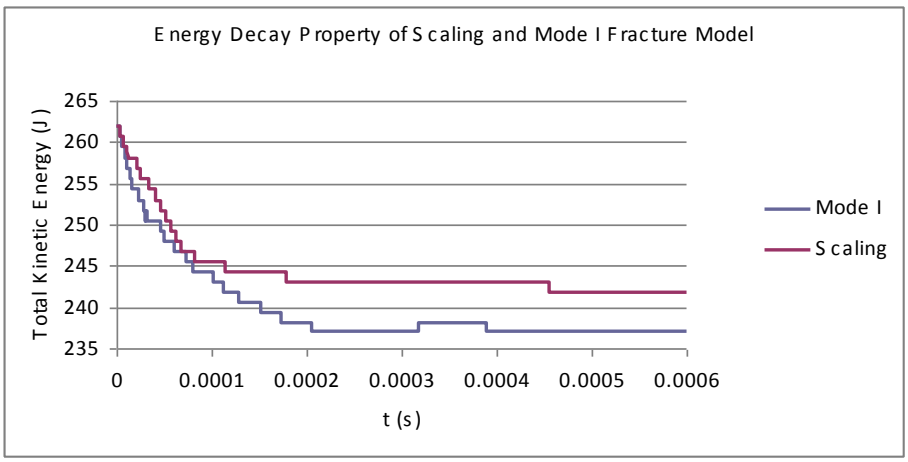

Figure 6.24 The energy decay curves of the scaling and Mode I fracture model

According to Figure 6.24, before the curve approach stable, about 20.2J out of the total 261.99J kinetic energy was absorbed for the fracture and deformation of the glass beam by using the scaling model, while this value was 25.01J for the Mode I fracture model. Since less kinetic energy was expended for fracturing, the residual kinetic energy of scaling model was higher than that of the Mode I model, leaving a gap between them. This phenomenon can be attributed to the reduced fracture energy due to the scaling. Since less energy was needed for the fracture process, more was retained after the completion of impact. In other word, less external energy is needed for fracturing if the scaling model was used instead of the Mode I mode, as the artificial scaling factor was introduced in the analysis.

And further, according to the parametric study in chapter 5, the reduced fracture energy implies that the glass become more brittle. That is why damage within a smaller area is obtained in comparison to the results of Mode I model.

The scaling model is a relatively simple reducing model and unloading is not considered. Suppose the point of the previous step within the damage envelope was *C1*, and for the next step, it moved to *C2* (Figure 6.25(a)). For simplicity, *O*, *C1* and *C2* were taken to be on the same straight line, thus they shared the same reduced softening curve. Obviously, unloading for both opening and sliding was occurred in this process. However, if the new point was mapped to the softening curve in Figure 6.25(b), the unloaded tensile stress is higher than that

of the previous step. The same applies to the shear stress.

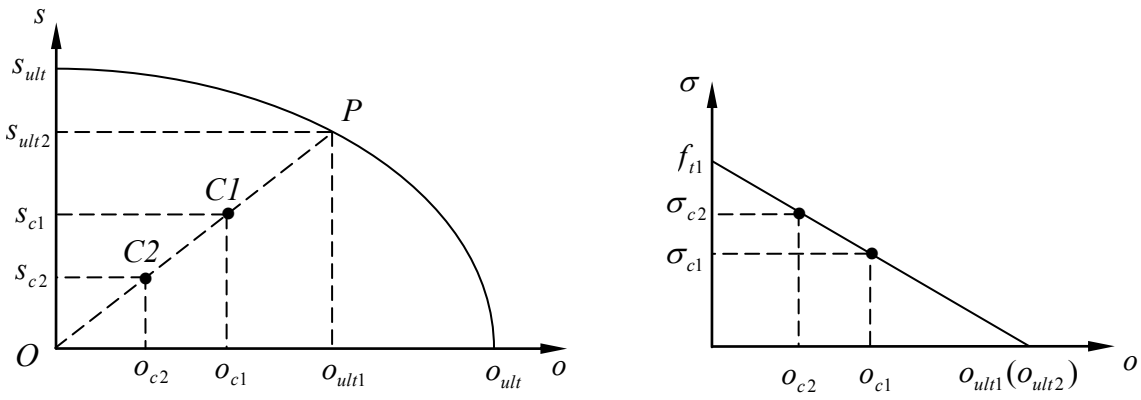

(a) Unload *C1* to *C2* along previous trajectory (b) Increase of unloading-stress σ_{C2}

Figure 6.25 Unloading not considered in the scaling model

Since it is an extreme case that point *C1* and *C2* share the same softening curve, the following discussion is for normal conditions which are more representative for the real simulation.

If *o* and *s* increase simultaneously ($o_{c2} > o_{c1}$ and $s_{c2} > s_{c1}$), the corresponding stresses should be $\sigma_{c2} < \sigma_{c1}$ and $\tau_{c2} < \tau_{c1}$. This is a basic law of the cohesive model and should be valid at all times. There are two possibilities in scaling model: the new point *C2* may situate in zone A or zone B as was illustrated in Figure 6.26.

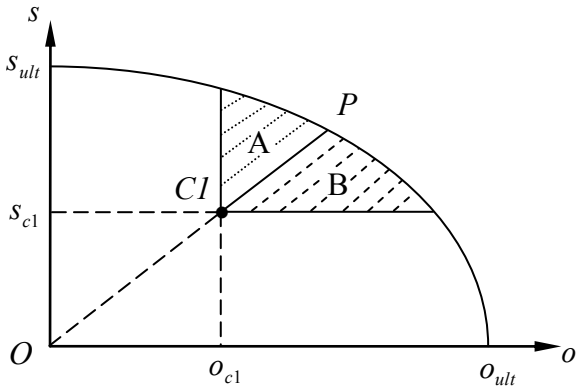

Figure 6.26 Possible zones A and B for the new stress point when both *o* and *s* increase

If the point *C2* was in zone A, then the current $o_{ult2} < o_{ult1}$ and $s_{ult2} > s_{ult1}$, which suggested that for normal stress, the newly obtained scaled softening curve will be lower than the old one of the previous time step, while for shear stress, the curve will be above the old one (shown in Figure 6.27).

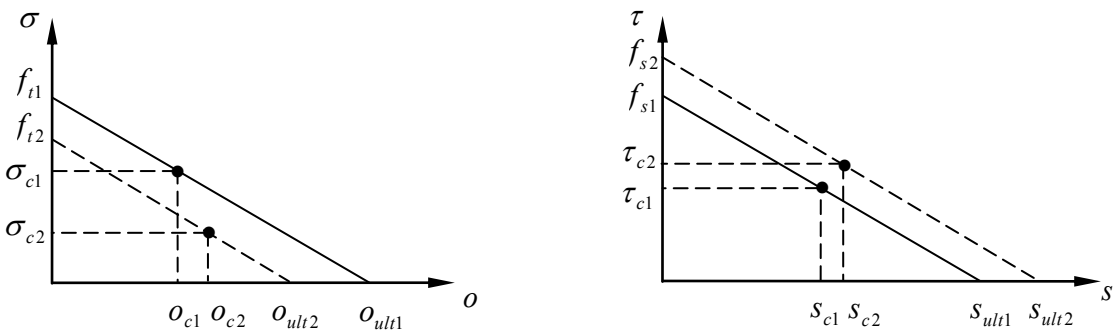

(a) $o_{c2} > o_{c1}$, $\sigma_{c2} < \sigma_{c1}$ (b) $s_{c2} > s_{c1}$, $\tau_{c2} > \tau_{c1}$

Figure 6.27 The tensile and shear stress development when the point is in zone A

According to Figure 6.27a, $\sigma_{c2} < \sigma_{c1}$ and there is no problem with the tensile stress. However for the shear stress, even if the sliding distance increases, the shear stress can be higher than that of the previous step (Figure 6.27b). Similarly, if the point *C2* was located in zone B, shear stress would be okay but the same problem will happen to the tensile stress as $\sigma_{c2} > \sigma_{c1}$ may occur.

In another case, if *o* increase and *s* decrease ($o_{c2} > o_{c1}$ and $s_{c2} < s_{c1}$), the new point *C2* will be in zone D (Figure 6.28a). In this situation, we have $o_{ult2} > o_{ult1}$, which means the new strain softening curves for normal stress is above the one of the previous step. According to Figure 6.28b, since $o_{c2} > o_{c1}$, the possibility that $\sigma_{c2} > \sigma_{c1}$ still exists.

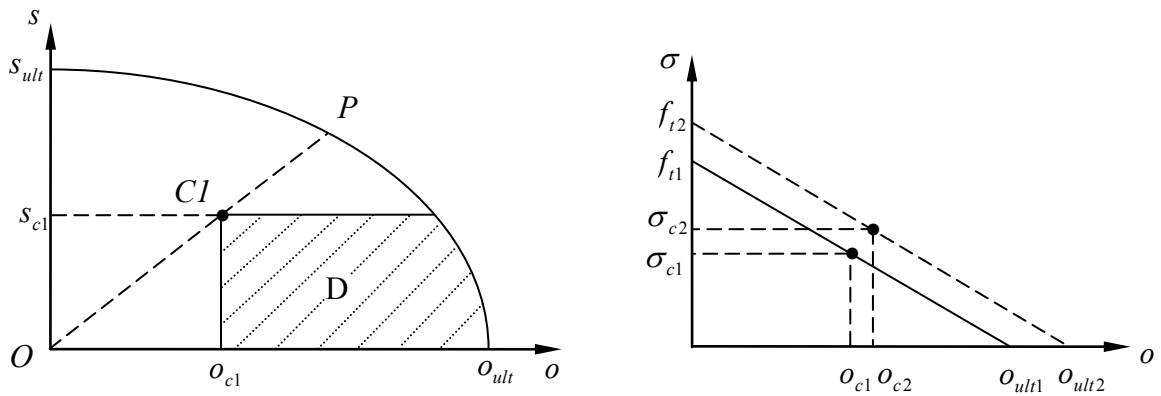

(a) Zone D that new point locates (b) Unrealistic tensile stress for loading

Figure 6.28 Condition of $o_{c2} > o_{c1}$, $s_{c2} < s_{c1}$ and possible tensile stress state

For other conditions, e.g. *o* decrease and *s* increase, or *o* and *s* simultaneously decrease,

similar conclusions can be derived in this approach performed above. Thus when *o* or *s* increases, the stress cannot be guaranteed to decrease, which is not acceptable. The increase in stress while loading in strain softening zone violated the basic law of cohesive model and will result in unrealistic stress in the simulated body.

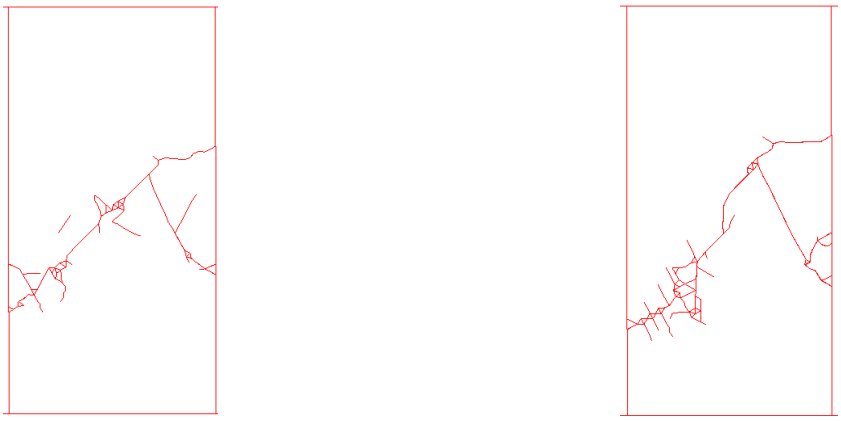

(a) $45^\circ / 45^\circ$ (b) $45^\circ / 90^\circ$

Figure 6.29 The compression results using the scaling model at t = 1.3s

Since the stress within the glass using scaling model can be unrealistic, fracture may occur at some places where it should not. According to Figure 6.29, the scaling model did not exhibit acceptable results as the elasto-plastic fracture model did.

6.3.3 Conclusions

Through the discussions and numerical examples performed above, some features of the scaling model can be addressed as follows:

(1) The scaling factor is artificially used in this model and reduced fracture energy is introduced as a consequence.

(2) The unloading is not considered in this model.

(3) The model cannot guarantee that stress will decrease while loading in the strain softening region, which may severely violate the basic principle of cohesive model.

(4) The model is largely acceptable on very general aspect but cannot do well in shearing and mixed mode problems.

From these points of view, the elasto-plastic model has some advantages over the scaling one. And in the following simulation of laminated glass, the elasto-plastic model will be used if not specified explicitly.

6.4 Laminated Glass

In this section, a completely new type of glass, laminated glass will be discussed. Briefly introduced in chapter 1, laminated glass is an assembly of glass sheets with interlayer(s). In this section, the previously-developed elasto-plastic fracture model will be employed to model the damage response of laminated glass after impact. The model will not only be applied to glass, but also the interfaces between the glass and interlayer.

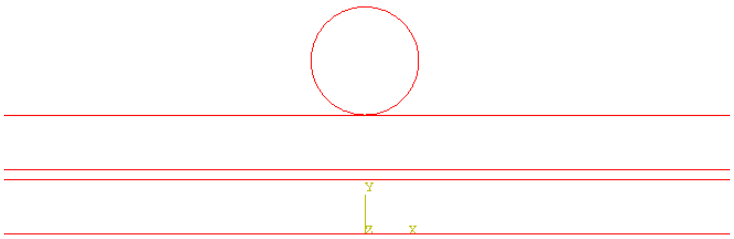

(a) The detailed laminated strategy

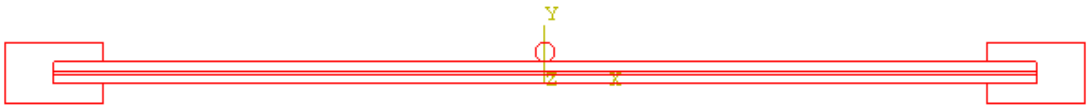

(b) The structural configuration and boundary condition of the laminated glass

Figure 6.30 Configurations of the projectile and the laminated glass

In this study, the laminated strategy that two glass layers adhered to a PVB interlayer in the middle (Figure 6.30a) will be investigated as it is widely used in industry. Consider a 1m long 22mm high laminated beam with both ends clamped in a rigid channel (Figure 6.30(b)), the beam is made up of two 10mm high glass layers and one 2mm high PVB interlayer. It was subjected to the impact of a steel ball with the radius of 10mm at the velocity of 2m/s. Here we assume the ability of PVB to resist deformation and fracture is sufficient enough thus large value of fracture energy was assigned. According to Vallabhan et al. (1992), Dhaliwal and Hay (2002) and data from other industry reports, material properties of PVB and the interface between glass and interlayer used in the analysis were given in Table 6.1.

	PVB	Interface
Young's Modulus	100MPa	Not applicable
Poisson's Ratio	0.4	Not applicable
Density	1100kg/m3	Not applicable

Fracture Energy	4 x10^4 N/m	200 N/m
Tensile Strength	20MPa	100MPa
Shear Strength	10MPa	50MPa

Table 6.1 Material properties of the PVB and interface

Damage responses of both laminated and monolithic glass using the same mesh configuration at t = 0.6ms were given by Figure 6.31. Obviously, both beams suffered local crushing damage on the top around the contact point and damages in both laminated and monolithic glass were quite similar.

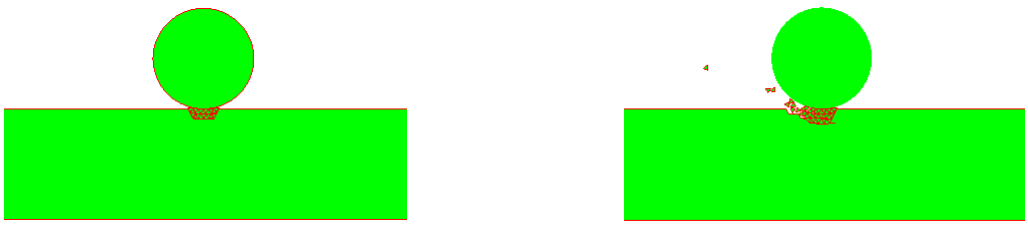

(a) Laminated glass (b) Monolithic glass

Figure 6.31 Damage response of laminated and monolithic glass under 2m/s impact at t = 0.6ms

From the kinetic energy curve in Figure 6.32, it can be observed that both laminated and monolithic glass experienced energy decay while laminated glass behaved better than the monolithic one. In conjunction with the Figure 6.31, although laminated glass absorbed more kinetic energy, the damage around the impact point was less severe than the monolithic glass in Figure 6.31(b). This is because, for laminated glass, the deformation of PVB interlayer absorbed kinetic energy. While for monolithic glass, energy was principally absorbed by the

fracture of glass elements.

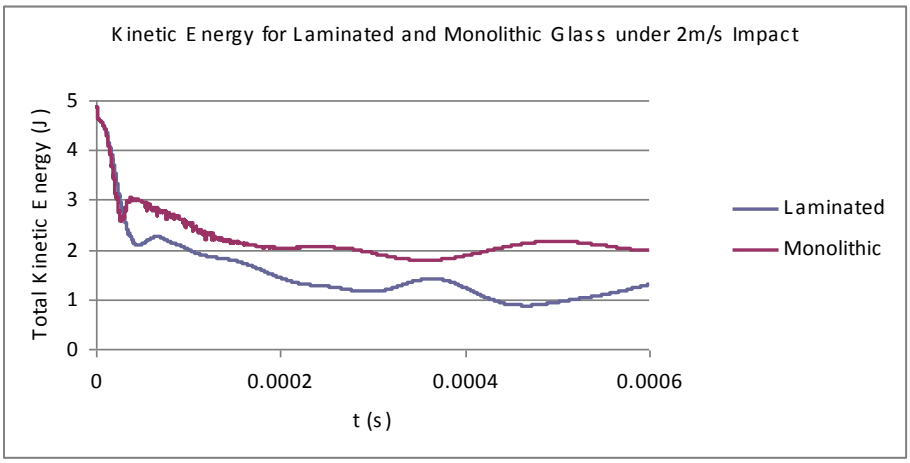

Figure 6.32 The total kinetic energy of laminated and monolithic glass system for v = 2m/s

In the previous low velocity impact example (2m/s), the "laminated glass strength equals or exceeds the strength of monolithic glass of the same nominal thickness" (Norville et al., 1998) can be clearly observed. To enable the interlayer exhibit its ductility and resistance further, the impact velocity of the projectile was raised to 18m/s. The transient responses of laminated glass beam at different times were shown in Figure 6.33.

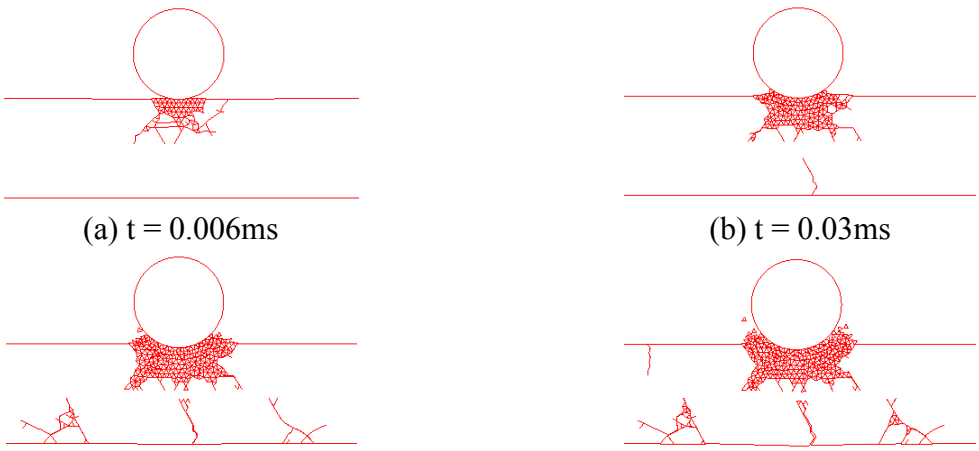

(a) t = 0.006ms (b) t = 0.03ms

(c) t = 0.06ms

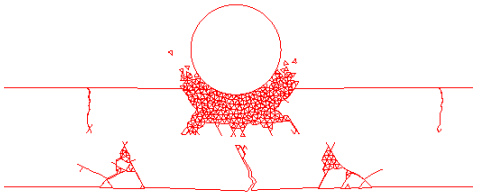

(d) t = 0.09ms

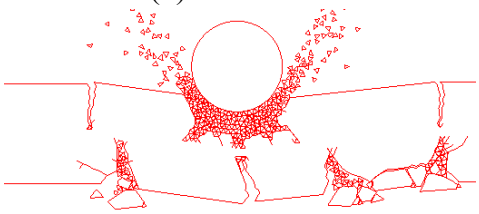

(e) t = 0.12ms

(f) t = 0.6ms

Figure 6.33 The transient responses of laminated glass beam under impact of projectile with velocity = 18m/s

The typical damage development of laminated glass beam can be concluded from Figure 6.33. At the beginning (Figure 6.33(a)), only some local damage can be observed near the contact area in the upper glass layer. The interlayer, lower glass layer as well as the interface was intact. Later on (Figure 6.33(b)), bending cracks started to develop from the bottom of the lower glass layer and propagated onto the interface between the interlayer and bottom glass layer. The bending crack at the bottom glass layer developed even further with the increase of the deformation of the soft PVB interlayer (Figure 6.33(c)) and soon it appeared in the top glass layer (Figure 6.33(d)).With time elapsing, bending developed even further in Figure 6.33(e) and (f) and more damage away from the contact area in glass layer was also observed.

It can be concluded that for laminated glass, upper glass layer is usually subject to some local crushing caused by the projectile before lower glass layer undergo some through thickness crack (bending) onto the interface. With the time elapsed, bending also can be found in the upper glass layer. The whole damage process is of the “crushing-bending” type. However, it is worth mentioning that distinct from monolithic glass using the same mesh and impact

velocity (Figure 6.34), the majority of fractured glass fragments are still adhered to the PVB interlayer and will not fall down, thus injury to human can be avoided.

Comparing Figure 6.33 and 6.34, cone crack that usually obtained for monolithic glass did not appear in laminated glass analysis. This is largely due to the introduction of interlayer in the middle of the beam. Since both beams suffered crushing on the top where the projectile contact at, cone crack can only be obtained at lower height as in Figure 6.34. The existence of ductile interlayer in the middle changes the stress propagation and crack development, making the cone unable to form.

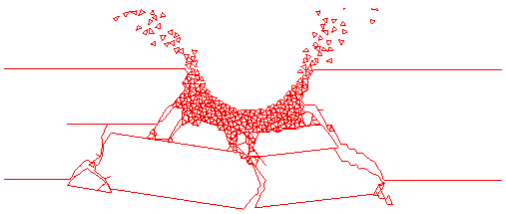

Figure 6.34 Damage response of monolithic glass at t = 0.6 ms

Figure 6.35 gave the kinetic energy curves of both monolithic and laminated system under the impact velocity of 18m/s. The difference between monolithic and laminated glass is obvious and significant. The monolithic glass quickly finished the fracture process around t = 0.02ms, leaving a relatively level curve after that. On the contrary, due to the ductility of interlayer, the laminated glass continuously absorbs the kinetic energy until the end of simulation. There is no indication that this absorption will approach completion till the end of the simulation. The kinetic energy curve will decrease further down but it will take too long to simulate.

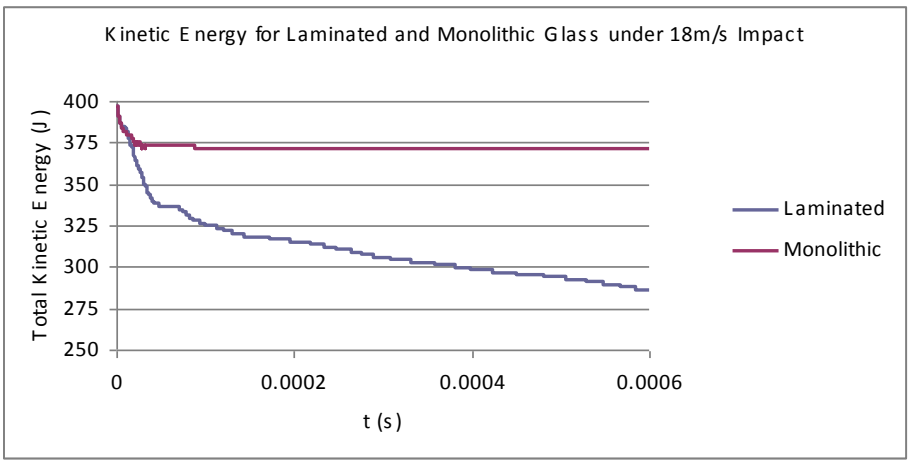

Figure 6.35 The total kinetic energy of monolithic and laminated glass system at v = 18m/s

Quantitatively, at the end of the simulation (t = 0.6ms), the absorbed kinetic energy is 25.1J for monolithic glass system, which is only 6.33% of the total 396.8J kinetic energy before impact. For laminated glass system, this number is 110.4J, 27.8% out of the initial kinetic energy. The introduction of PVB interlayer greatly improved the energy absorption performance of the laminated glass.

It is also worth mentioning that the deformation of the interlayer resulted in a larger damage area for laminated glass. According to Figure 6.33 and 6.34, a damage area of around 2-3 times of the diameter of the projectile was created by the impact on the monolithic glass, while for laminated glass, fracture propagated to 4-6 times of the projectile size far from the impact point. Fortunately, since most fragments are adhered to the interlayer, one conclusion can be drawn that under the same condition, laminated glass will be safer than monolithic one.

6.5 Summary

This chapter discussed the mixed Mode (I + II) fracture modelling and developed the elasto-plastic and scaling model for the fracture of glass, respectively. Each model was followed by numerical examples and discussions. Experimental observations from shearing and tension on gypsum were used as a reference to verify the proposed model, where the elasto-plastic model reached a better agreement than that of the scaling model.

For the elasto-plastic fracture model, mixed-mode was considered and unloading was taken into account. Ball impact and in-plane loading problems were analysed and results were compared with that from the Mode I fracture model developed in chapter 4, reaching some similarity. Uniaxial compression tests from Shen et al. (1995) were used as a reference in the testing of the ability of the model in simulating mixed mode problems. The results from the elasto-plastic model achieved good agreement and were verified. The similarity between the results from the elasto-plastic model and Mode I model were investigated both from the theoretical and numerical aspects. It can be concluded that Mode II is not important in glass fracture analysis, thus the similarity in result for the two models is understandable and acceptable.

For scaling model, results were compared with the data from the Mode I fracture model on the

ball impact example and a generally acceptable result was obtained. Since the strain softening curve was reduced by the scaling factor, the actual fracture energy required for the fracturing of glass in the analysis was smaller than that from the Mode I fracture model. Since the model cannot guarantee that stress will decrease while loading in the strain softening zone, it violates the basic law of cohesive model. Consequently, the stress field obtained within the body can be unrealistic, which may lead to unrealistic interaction forces between elements, and further change the separation that controls the crack. And as a result, an undesirable and unrealistic crack pattern can be obtained.

Laminated glass beams of typical three layers were investigated using the previously developed elasto-plastic fracture model. Numerical analysis in section 6.4 showed that for low input energy (comparing with the capacity of targets), laminated glass does not show much advantage over monolithic glass in terms of absorbing the kinetic energy. For higher input energy, the fracture resistance of PVB interlayer was well exhibited and the laminated glass has undergone large deformation. Meanwhile, fragments can be adhered to the interlayer, preventing the human from injury.

The ductility of interlayer also introduced the enlarged damage effective area of laminated glass, which is larger than that of monolithic glass. Since the fragments can be adhered to the interlayer instead of flying away, laminated glass is much safer than the monolithic ones under the same condition.

LAMINATED GLASS: COMPARISON AND PARAMETRIC STUDY

7.1 Introduction

In chapter 6, a laminated glass beam with a circular projectile impacting at velocity was investigated in 2D. The incorporation of the PVB interlayer enables the glass beam to resist the impact load without breaking into pieces. In this chapter, both the comparative and the parametric studies (section 7.2 and 7.3) on the laminated glass are performed. The elasto-plastic fracture model developed in chapter 6 will be employed in the 2D simulation if not otherwise indicated. Also, material properties given in Table 4.1 and 6.1 are used for the glass and interlayer respectively.

In the comparative study section, results generated by the FEM/DEM are compared and discussed with that from other research results using either the FEM or the DEM. Simulation on laminated glass using the FEM/DEM is verified on the reliability and accuracy. 2D examples from Flocker and Dharani (1997b) and Zang et al. (2007), along with a 3D laminated glass plate from Timmel et al. (2007) are chosen for investigation. Though not completely the same as the data provided (and actually should not as they are from different methods), results from the FEM/DEM reached good agreement with that from other methods and exhibited particular merits that cannot be otherwise obtained, such as: (1) modelling the flying fragments in contrast to the FEM; and (2) the resulting cracking pattern and

deformation in contrast to the ordinary DEM.

In the parametric study section, the focus is given to the properties of the interlayer as well as the interface of the laminated glass. The sensitivity of the behaviour of the interlayer with respect to input energy, strength of interface and the Young's modulus are investigated and their influences on the responses of laminated glass under impact are discussed.

The summary section 7.4 follows the parametric study immediately. The results in the comparative study showed that the FEM/DEM is capable of simulating the impact on laminated glass. And through parametric study, some guidance of design and manufacturing on the laminated glass are provided as well.

7.2 Comparative Study

The comparative study aimed at verifying the FEM/DEM was performed in this section. The FEM/DEM was compared with either the traditional FEM or the traditional DEM by using the same configuration with necessary modifications. Both 2D and 3D examples were included. For 2D examples in section 7.2.1 and 7.2.2, the elasto-plastic model was used, and for the 3D example in 7.2.3, the fracture model is the Mode I model as currently the elasto-plastic model has only been done for 2D stress state. Results demonstrated that the FEM/DEM is capable of analysing the impact problem on laminated glass. While reaching good agreement with the

FEM and DEM, its own features and advantages were retained.

7.2.1 2D Example - Comparison with 2D FEM

Flocker and Dharani (1997b) presented a method that allows the traditional finite element wave propagation code to model small projectile impact with low velocity on architectural laminated glass where fracture must be included in the analysis. In their research, a typical three-layer glazing window was considered: two soda-lime glass plies plus one PVB interlayer. Explicit finite element code DYNA2D (Whirley et al., 1992) was modified to incorporate cracking algorithm and used in the analysis.

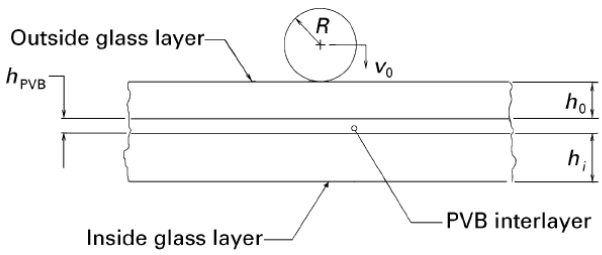

Figure 7.1 The configuration of the lamented glass unit used by Flocker and Dharani (1997b)

Figure 7.1 illustrated the laminated glass unit in their analysis. The thickness of outer glass layer $h_o = 4.76$ mm, the PVB interlayer $h_{PVB} = 1.59$ mm and the inner glass layer $h_i = 6.35$ mm. The laminated glass subjected to a normal impact of a 3.97mm radius steel ball at the velocity of 35.8m/s.

Along the direction that perpendicular to the impact, a non-reflective boundary was used, thus "finite thickness, infinite length" was realised. Since there is no such special boundary in the current implementation of FEM/DEM, length of 4cm was used, so that crack-forming process will not be much influenced by the stress waves that were reflected back from the two ends of the laminated glass.

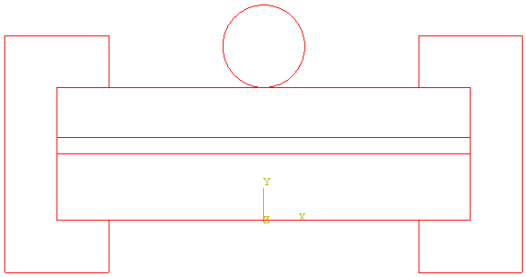

Figure 7.2 The configuration of the laminated glass used in FEM/DEM

In Flocker and Dharani (1997b), the glass and interlayer was assumed to be perfectly bonded, and this was achieved by assigning large fracture energy to the interface between the glass and PVB elements in the FEM/DEM. The configuration of model used in the FEM/DEM was shown in Figure 7.2 with elements sized 0.2mm within the laminated glass body and the outer surface of the projectile so that a circular shape can be obtained. Material properties used in this simulation were given in Table 7.1, where glass and steel properties (density, Young's modulus, Poisson's ratio) were taken from Flocker and Dharani (1997b) and the PVB data was from Vallabhan et al. (1992) as well as Dhaliwal and Hay (2002) which was mentioned in chapter 6. The fracture energies of PVB and steel have been assigned a large value so that fracture will not occur in either material.

	Glass	PVB	Steel
Young's Modulus	70GPa	100MPa	200GPa
Poisson's Ratio	0.25	0.4	0.29
Fracture Energy	4N/m	$4x10^4$ N/m	$2.5x10^6$ N/m
Tensile Strength	30MPa	20MPa	200MPa
Shear Strength	15MPa	10MPa	100MPa
Density	$2500kg/m^3$	$1100kg/m^3$	$7800kg/m^3$

Table 7.1 Material properties used in simulation

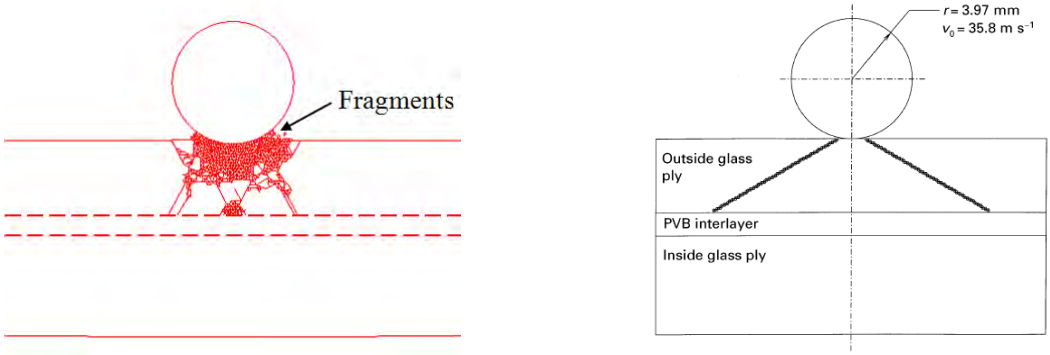

(a) FEM/DEM (a) FEM

Figure 7.3 Damage responses of laminated glass using both FEM/DEM and FEM at t = 7.6 μs

Figure 7.3 showed the responses of laminated glass using both the FEM/DEM and FEM at t = 7.6 μs. It can be observed that in Flocker and Dharani (1997b), a cone was obtained with the angle of 60° to loading axis, while for the results of the FEM/DEM, a cone type crack was obtained with the angle of about 30° to that axis. The angle of the cone obtained in FEM simulation looks more like the consequence of static indentation not dynamic impact. According to Cook and Pharr (1990), the sequence of Hertzian indentation produces a cone "at an angle of 68°" to the load axis. For dynamic impact, Knight et al. (1977) pointed out that the cone angle varies with the impact velocity. The higher the velocity, the smaller the

angle will be to the load axis. Also, size of projectile may has some influence on that. Figure 7.4 showed some cone angles in glass impact examples from the experimental observation of Knight et al. (1977), where a small angle to the load axis is common.

(a) 1mm diameter ball, 200m/s (b) 1mm diameter ball, 240m/s

Figure 7.4 Small cone angles to the load axis (after Knight et al. (1977))

Consequently, a cone angled about 30° to the load axis in the FEM/DEM simulation is acceptable and more akin to a dynamic response. Research in Knight et al. (1977) indicated that if the impact velocity is decreased, the angle to the load axis should increase accordingly. However, the FEM/DEM simulation with lower impact velocity in this example suggested that either the velocity is too low to form a cone, or a similar angle of cone was obtained. It is not currently clear why there is little change in the angle while velocity changes in contrast with the results obtained by Knight et al (1977). It may relate to the fracture criteria used and possibly the dilatancy characteristic of the model. For the moment, no dilatancy is assumed for the mode I fracture model and associated flow rule is assumed for the elasto-plastic model which may be different from the actual behaviour of the glass.

(a) Test result from Knight et al. (1977) (b) Result from the FEM/DEM

Figure 7.5 The median (M) and lateral (L) crack obtained 2 μs after impact

According to the theory of loading and unloading, lateral crack can be obtained when the specimen is undergoing unloading. In dynamic impact, since the projectile may be bounced up a little bit due to the rebound from the target after impact, the median and lateral crack can be observed very soon after the start of impact, as was shown in Figure 7.5a. Comparing with the crack type in Figure 7.5a and 7.5b, the traces of median and lateral cracks mapped well with the experimental observation, which demonstrated that the simulation in the FEM/DEM has undergo genuine dynamic impact. However, these two types of cracks cannot be found in the FEM simulation, which further indicated that no unloading occurred and suggested quasi-static-like loading was obtained.

According to the observation of Chaudhri and Kurkjian (1986), fine-particle debris can be found ejected during loading around the contact point, which cannot be seen in the FEM simulation but available in the FEM/DEM result. This is largely due to the intrinsic shortcoming that FEM is not capable of dealing with fragmentation.

Table 7.2 summarised the major differences between the results of FEM/DEM and FEM and

the key reasons for the difference.

	FEM/DEM	FEM	Cause
Cone crack angle to load axis	30	60	Dynamic impact in FEM/DEM while more static in FEM
Median and lateral crack	Yes	No	Genuine dynamic impact involve loading and loading in FEM/DEM
Fragmentation	Yes	No	Intrinsic properties, FEM is not capable of fragmentation

Table 7.2 The main differences between the results from FEM/DEM and FEM

It can be concluded that results from FEM/DEM reached a certain level of agreement with that from FEM, but closer to the experimental observation. A cone type crack was obtained but with different angle. Median and lateral crack were found in the FEM/DEM with some fine debris around the impact point. In both cases, the inner glass layer was intact, which can be explained that the fracture wave from the top was stopped by the PVB interlayer. Also, since the simulation time is very short, the laminated glass has not got a chance to experience large deformation, which can cause the bending cracks in both outer and inner glass layers.

7.2.2 2D Example - Comparison with 3D DEM

Zang et al. (2007) presented an investigation into the fracture behaviour of automobile laminated glass subject to rigid impact by using 3D DEM. Spheres were used as the basic particles and the entire failure process was shown demonstrating the advantage of laminated

glass in safety control. In their research, fixed laminated glass with two glass layers and one PVB interlayer, with the size of 100mm×98.8mm×4.76mm (0.76mm for PVB and 2mm for each glass ply) was studied. The laminated glass was subjected to the impact of a 12mm diameter ball with the mass of 1kg at the velocity of 30m/s.

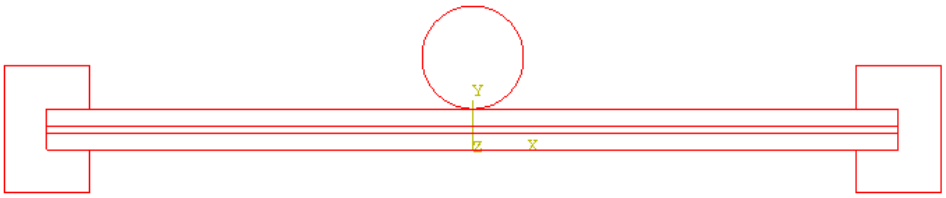

(a) The structural configuration of the laminated glass

(b) The element configuration of the laminated glass and projectile

Figure 7.6 The configuration of the laminated glass unit used in FEM/DEM simulation

In order to show the crack pattern with sufficient number of elements (it is expensive to do so in 3D, and the inefficiency of FEM/DEM simulation in 3D will be shown in chapter 8), a 2D example with 100mm×4.76mm and unit width (Figure 7.6) was used in the FEM/DEM simulation. As the model has been idealised from 3D to 2D and no reduction effect (such as the beam thickness, projectile size) be considered, some overall accuracy could be lost for this plate impact problem, but it will be beneficial in demonstrating the damage process. The particle size was 0.76mm diameter in DEM while in FEM/DEM, 0.38mm size elements were used, thus PVB can be modelled using two layers of elements. Since more elements with

finite deformation were used for the interlayer, the simulation of the ductility of the PVB can be simulated.

According to Zang et al. (2007), some physical parameters they used (Young's Modulus of glass, tensile and shear strength of glass and PVB, etc.) were slightly different from those given in Table 7.1, which have been tabulated in Table 7.3. To enable the fracture of interlayer, 50N/m fracture energy was assigned to the PVB.

	Glass	PVB
Young's Modulus	74.1GPa	100MPa (unchanged)
Tensile Strength	34.6MPa	18.62MPa
Shear Strength	17.9MPa	17.9MPa
Fracture Energy	4N/m (unchanged)	50N/m

Table 7.3 Updated material properties used in FEM/DEM simulation

Figure 7.7 showed the entire fracture process from the very beginning to 500 μs of both the FEM/DEM and DEM (Zang et al. (2007)) simulation. It can be observed that the transient responses in Figure 7.7(a) and (b) are similar. In both simulations, the projectile penetrated the laminated glass, eventually. And also it can be found that the relative position of the projectile and laminated glass reached a good agreement.

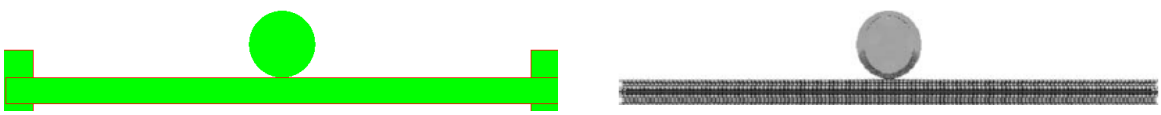

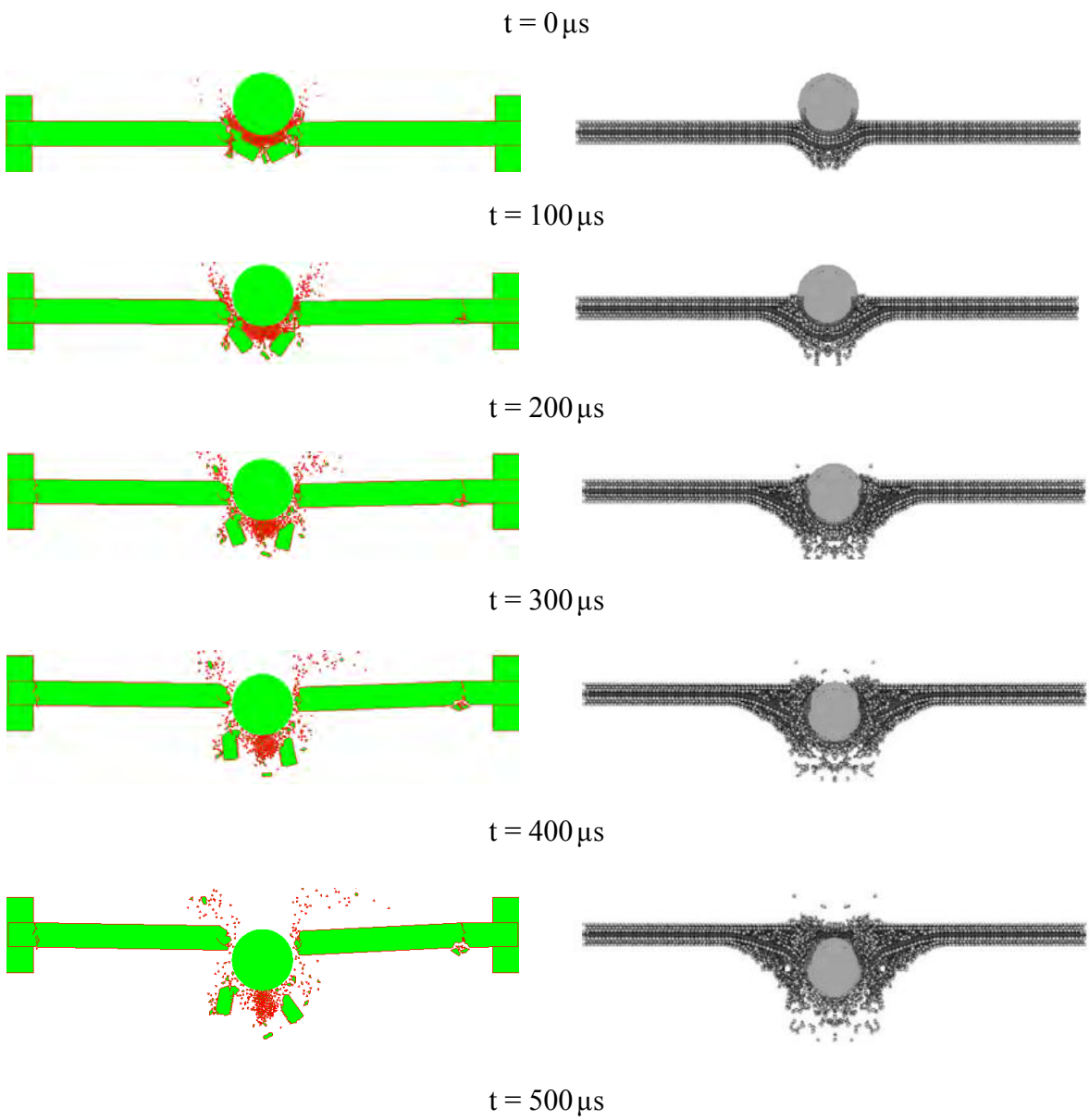

(a) FEM/DEM (b) Zang et al. (2007)

Figure 7.7 The damage processes by using FEM/DEM and DEM from 0 to 500 μs

However, despite a lot similarity, differences between the damage behaviours of the FEM/DEM and DEM can still be found:

(1) Between t = 100μs and 200μs, the PVB in FEM/DEM has been fractured by the large

impact energy brought in by the projectile, while the interlayer in Zang et al. (2007) experienced quite large deformation, which further postponed the breakage of laminated glass.

If the fracture energy of PVB interlayer is increased, the laminated glass will behave differently. Figure 7.8 showed the responses with fracture energies of 200N/m and 1000N/m in the middle of the impact area.

(a) 200N/m (b) 1000N/m

Figure 7.8 The responses of laminated glass beam with different fracture energies of PVB interlayer at t = 200 μs

It can be observed that although the fracture energy of the interlayer was increased, the PVB elements in the FEM/DEM simulation still cannot reach such large deformation as Figure 7.7(b) did though the deformation is substantially larger than the one obtained using lower fracture energy. Since the ball connection was used in the DEM, more deformability was obtained than the triangular elements used in the FEM/DEM.

(2) As to the fragmentation, results from the FEM/DEM have more small flying fragments

above the laminated glass and these fragments were obtained near the contact point almost immediately after the impact took effect while the fragments in Zang et al. (2007) can be observed no earlier than 0.3μs and most of them were below the sample.

(3) For the FEM/DEM, besides the elemental-sized fragments, there were two large pieces of glass fragments with fractured PVB adhered to, while for DEM the fragments were more divided and particle-based. From this point of view, the result of the FEM/DEM is closer to the reality and capable of simulating larger fragments.

(4) It should be noted that since two channels were included in the FEM/DEM to simulate fixed ends, some cracks can be found in the laminated glass body near its two ends due to bending and the restraint that these channels provided. These cracks were local and away from the impact effective area, thus will have little effect on the fracture pattern in the middle. And since the virtual fixed boundary was used, no such cracks can be observed in Zang et al. (2007).

The reasons for these differences are complicated. However, in spite of their differences, the FEM/DEM did achieve good agreement with the DEM and demonstrated its reliability in laminated glass simulation. It is worth mentioning that since the 3D laminated glass model be idealised to a 2D beam without any consideration of the change in the ball size, beam thickness or impact velocity, the final results and conclusions from the 2D FEM/DEM

simulation will need some modification if they are to be used for further design or analysis purpose.

7.2.3 3D Plate - Comparison with 3D FEM

Timmel et al. (2007) investigated a spherical projectile impacted on a fixed laminated glass plate using the explicit finite element solver LS-DYNA (LSTC, 2007). The glass layer was modelled with coinciding shell elements and the interlayer was modelled as a hyper-elastic membrane with no fracture was considered. Since only one shell layer was used for the two glass layers, the assumption that both layers fail at the same time was held. Consequently, in the FEM/DEM simulation, configuration of one glass layer over one interlayer was used.

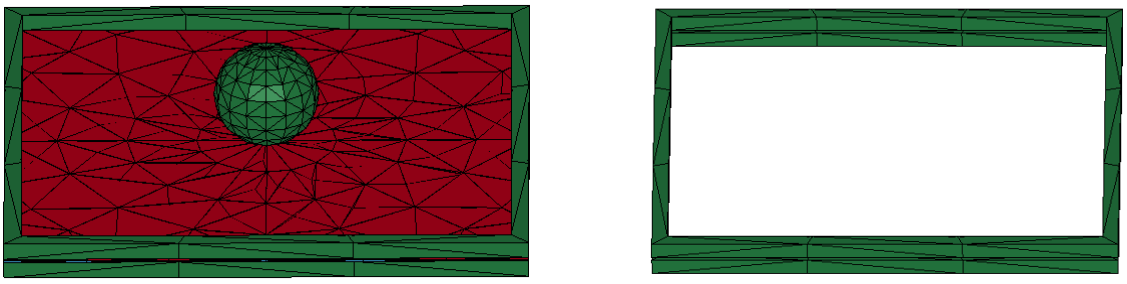

(a) Mesh configuration (b) Boundary condition

Figure 7.9 The structural, mesh and boundary configurations used in the FEM/DEM simulation

The laminated glass plate was a 1500mm x 1500mm square (Figure 7.9(a)) with the thickness of 5.38mm (5mm for glass and 0.38mm for the interlayer). The plate was clamped by two

20mm thick rigid steel frames as was shown in Figure 7.9(b). There will be no rotation within the steel frames but the plate can move freely in its own plane along the horizontal direction. Since the interlayer was assumed not being able to fracture, a 5mm thick interlayer was used in the FEM/DEM simulation to improve the computational performance as the time step can be larger without affecting the results. The spherical projectile is 300mm in diameter and 70kg in mass hitting with a velocity of 10m/s. The glass and interlayer material properties that used in the FEM/DEM analysis were adopted from Table 7.1 with the change of Poisson's ratio 0.23 from Timmel et al. (2007). Figure 7.10 showed the fracture pattern from the FEM/DEM simulation at t = 1.6ms.

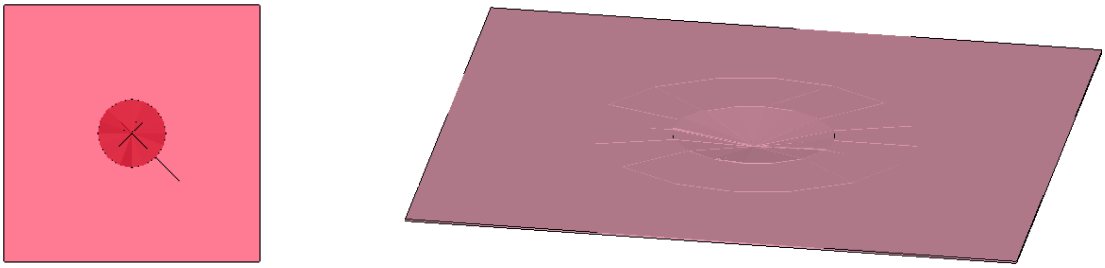

(a) Top view (b) Perspective view

Figure 7.10 The cracks at t = 1.6ms of the plate (1.5mx1.5m) by using the FEM/DEM

According to the Figure 7.10(a), the cracks developed from the centre of the plate along the tangential and radial direction. The cracks are not obvious in the figure. The perspective view in Figure 7.10(b) gave a clearer trend that the plate will undergo and indicated what the crack pattern will look like in the further simulation.

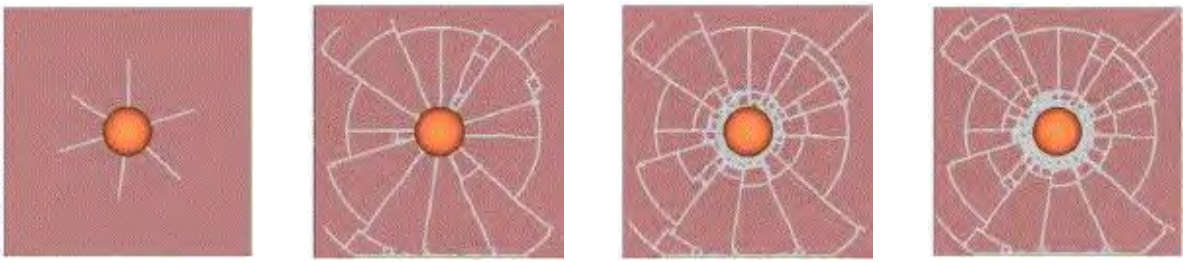

(a) t = 10ms (b) t = 20ms (c) t = 30ms (d) t = 40ms

Figure 7.11 The fracture patterns of the plate from Timmel et al. (2007) at different times

Figure 7.11 showed the fracture pattern obtained by Timmel et al. (2007). Since the FEM/DEM is quite slow in 3D, computation up to 40ms is very expensive and cannot be afforded in this research (each 1ms modelling may take one week of computation to complete in this case). But the current results at t = 1.6ms showed that micro radial-tangential cracks were partially formed. Comparing with the results in Figure 7.10, the crack pattern from the FEM/DEM is similar with that from Timmel et al. (2007) but developed faster than that, which is related to the rate of deformation and will be discussed later. It can be believed that with the elapsing of time, the deformation of laminated glass plate will become larger and larger. As a consequence, the glass will experience more bending, leading to much more obvious radial-tangential cracks.

The deformation trend of the laminated glass plate in z direction (i.e. the plane perpendicular to the impact direction) was presented in Figure 7.12. It can be seen that for both time points (t = 0.4ms and 0.8ms), the deformation in the middle of the plate is much larger than that of the outside area. And also with the time elapsing, the whole plate has undergone more

deformation as well.

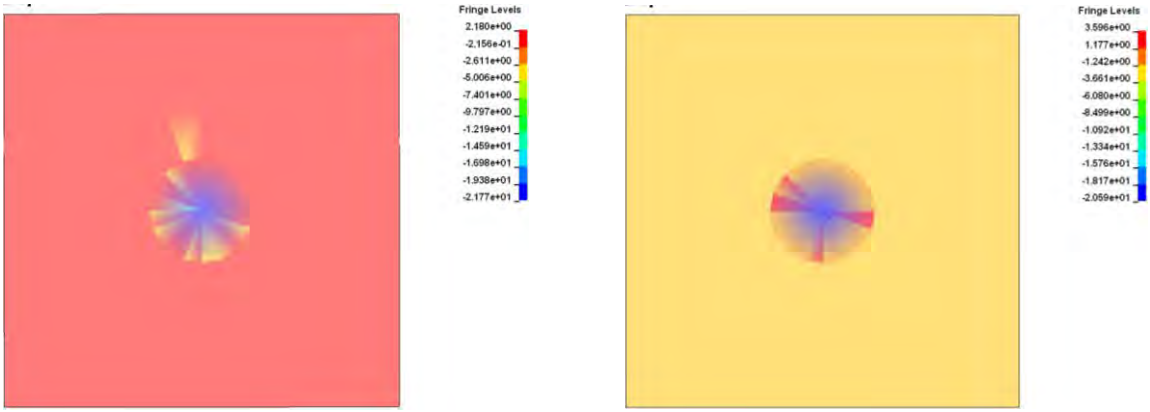

(a) t = 0.4ms (b) t = 0.8ms

Figure 7.12 z displacement of the plate at different times by Ls-Pre/Post (view from the top)

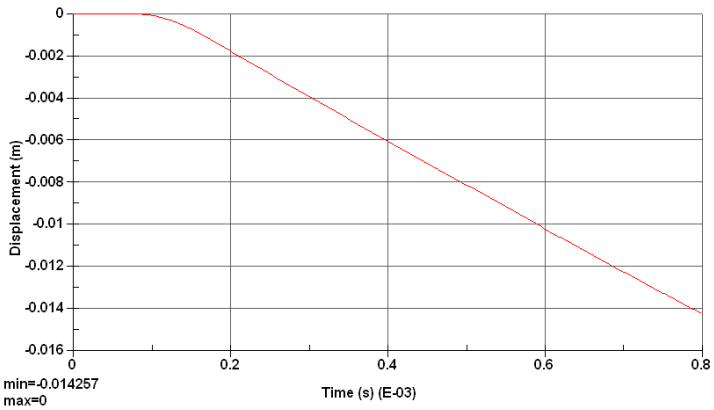

(a) The displacement obtained from the FEM/DEM simulation

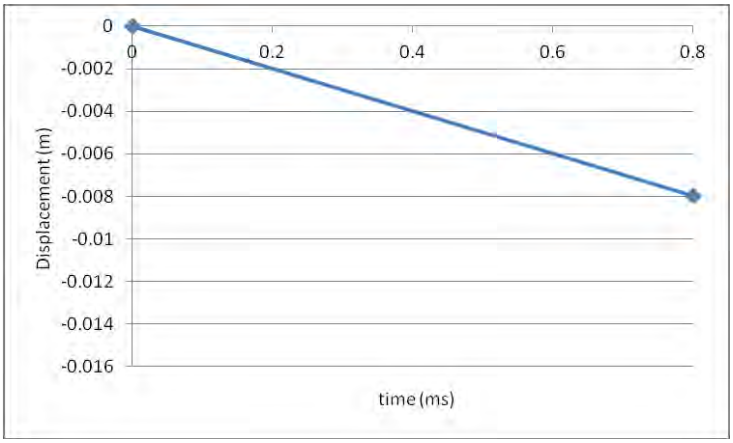

(b) Displacement curve interpolated from Timmel et al. (2007)

Figure 7.13 z-displacement of the central point in the laminated glass plate within 0.8ms

By investigating the point (Node 1911) in the centre of the plate, a curve of z displacement within 0.8ms was obtained from the FEM/DEM simulation (Figure 7.13(a)). From that curve, conclusion can be drawn that z displacement of the centre point increased almost linearly along the time except for a small flat interval at the very beginning, which can be attributed to the lag of the structure response. Figure 7.13(b) gave the deformation curve of the same point within 0.8ms interpolated from Timmel et al. (2007).

By calculating the slopes of both deformation curves in Figure 7.13, rate for FEM is 9.94mm/ms while for the FEM/DEM is about 20.37mm/ms. This explains why the fracture process in the FEM/DEM is faster than that in the FEM. The velocities of the projectile used in FEM and FEM/DEM were the same, and it is not clear why the movement and the fracture in the FEM/DEM simulation developed faster than that of the FEM. One possibility is related to the fracture criteria used and the location at which fracture is evaluated. This can be studied as future work.

The comparison of the z displacement of another three points (Nodes 1871, 1514 and 1795) on the plate (Figure 7.14(a)) were shown in Figure 7.14(b), where the red curve represents Node 1871, while the green and blue curves represent Node 1514 and 1795, respectively.

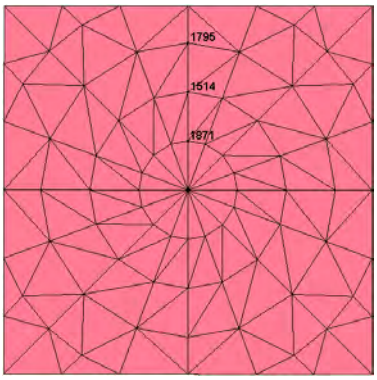

(a) Position of the three points

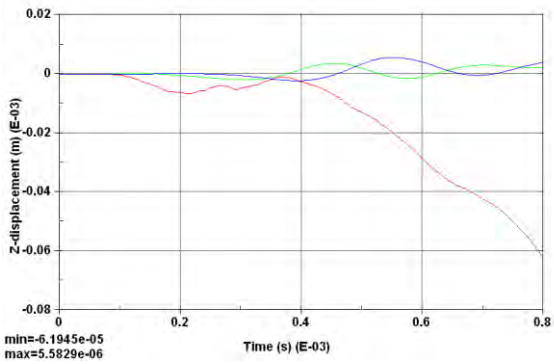

(b) The curve of z displacement of the three points

Figure 7.14 The three points and their displacement curves in z direction within 8ms

The three points were such chosen that they represent 200mm, 400mm and 600mm from the centre of the plate. Figure 7.14(b) indicated that for Node 1871, which is 200mm from the centre, exhibited the largest deformation among the three nodes (but still two magnitudes smaller than that at the centre point). The z displacement of nodes 1514 and 1795 are similar, oscillating along the zero-axis with very small amplitude within 0.8ms.

Through comparison, the damage pattern from the FEM/DEM showed that unlike the monolithic glass that always localised within a small area near the contact point, laminated glass with a ductile PVB interlayer can withstand larger deformation, which leads to more bending in the plate. This bending is indispensable for the propagation of the radial cracks and the initiation of the tangential cracks. In this example, the crack from the currently obtained results has not fully developed yet due to the short modelling time. With the development of bending, the radial-tangential cracks will be more obvious and propagated further.

The comparative studies investigated above showed that the FEM/DEM is capable of simulating laminated glass under impact. The reliability of the method as well as its results was verified as well.

7.3 Parametric Study

In the last section, 2D laminated glass examples (example one and two) were investigated for the verification of the elasto-plastic model and the FEM/DEM. In this section, parametric study over the laminated glass was performed. These parameters included the input energy (controlled by impact velocity), interface strength and Young's modulus of the interlayer. Structural, mesh and boundary configurations of the laminated glass example studied in section 6.4 (refer to Figure 6.30) were used for the purpose of this parametric study.

7.3.1 Input Energy

As has been discussed in chapter 5, different impact velocities will result in different responses of the monolithic glass, and so as to the laminated glass. As shown in section 6.4, for low impact velocity (2m/s), laminated glass do has some advantage over monolithic glass of the same thickness in absorbing the kinetic energy from the projectile, but not obvious. With the increase of the impact velocity (18m/s), more of the kinetic energy can be absorbed

by the laminated glass with a soft PVB interlayer. It should be noted that the impact velocity is just a single parameter of the total kinetic energy that projectiles brought in and laminated glass will behave differently under different input kinetic energies. Keeping the projectile the same and use different impact velocities, results can be obtained in terms of the input kinetic energy.

To ensure the PVB interlayer exhibit its ductility and fracture resistance, it was assigned with large fracture energy so that the fracture of interlayer is unlikely to happen. The structural configurations and material properties of the investigated samples are the same to that being used in section 6.4, and change of input kinetic energy is controlled by changing the impact velocity accordingly.

Figure 7.15 illustrated the responses of laminated glass beam under different impact velocity v ranged from 5m/s to 20m/s at t = 0.3ms. Corresponding damages of the monolithic glass using the same mesh at the same time were also given for comparison.

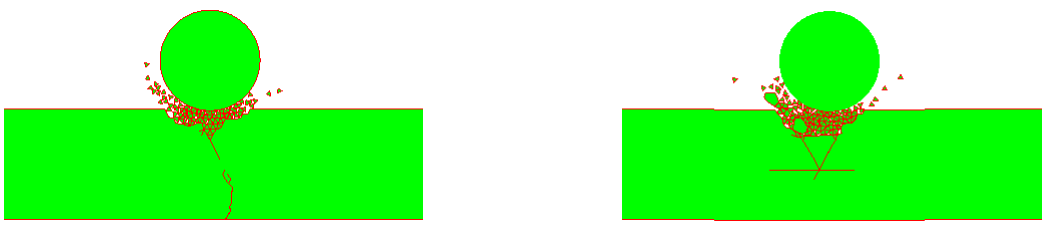

v = 5m/s

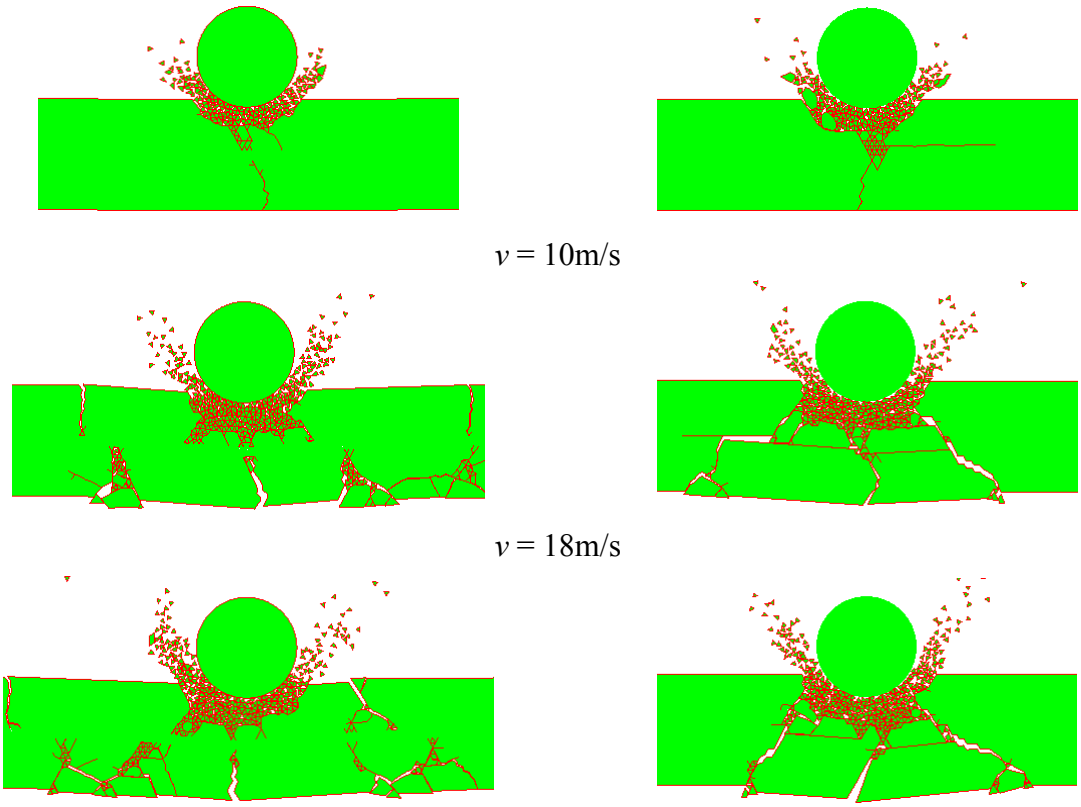

v = 10m/s

v = 18m/s

v = 20m/s

(a) laminated glass (b) monolithic glass

Figure 7.15 Response of laminated and monolithic glass under different velocities at t = 0.3ms

It can be observed from Figure 7.15 that for v = 5m/s, both the laminated and monolithic glass experienced some local crushing on the top near the impact area. For laminated glass, a central bending crack in the bottom layer was developed due to the high deformability of PVB interlayer, while cracks in monolithic glass did not propagated down to the bottom. For v =10m/s, damage in laminated glass has a similar crack pattern as that in v = 5m/s except for a bit more damage. With the increase of impact velocity, laminated and monolithic glass exhibited quite differently. For v = 18 and 20m/s, the top glass layer of laminated glass experienced crushing and some bending cracks were found near the contact point. Although

the bottom glass layer was protected by the interlayer, it has undergone large bending, and some bending cracks had resulted. For the monolithic glass, apart from the crushing near the contact area, a cone type crack was produced and the glass was penetrated by the projectile.

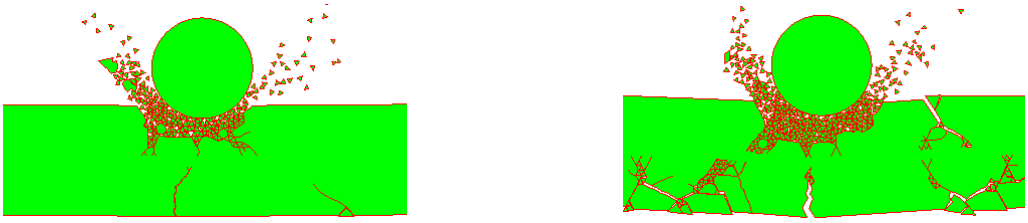

(a) Under 10m/s at t = 0.6ms (b) Under 20m/s at t = 0.3ms

Figure 7.16 The comparison between lower velocity with longer time and higher velocity with shorter time

Should the simulation (10m/s impact) be taken further to 0.6ms, the penetration of the projectile (Figure 7.16a) got slightly deeper than that of the 0.3ms in Figure 7.15a. However, comparing with the 20m/s impact at t = 0.3ms (Figure 7.16b), the impacts represent for two different mechanisms. For lower impact velocity, only the central bending crack that extends down to the interface between the glass and PVB is obtained; for higher impact velocity, more bending cracks in both upper and bottom glass can be observed due to larger deformation. The equivalent effect of higher impact at shorter time cannot be easily obtained by lower impact with longer simulation. The reason for this difference can be explained by the threshold of each mechanism. According to the parametric study of monolithic glass in chapter 5, each type of damage has a zone associated with it as was shown in Figure 5.10. If the input energy failed to reach the threshold of the next type of crack, damage will remain in the current

regime. That is a possible reason why the difference in crack pattern cannot be compensated by the longer simulation time.

The energy absorption ability of laminated glass does not necessarily increases along with the impact velocity. Should the initial kinetic energy be marked as K_i, the residual total kinetic energy of laminated and monolithic glass be taken as K_l and K_m, an index i (expressed in Equation 7.1) can be used for assessing the energy absorption capacity of monolithic and laminated glass. For laminated glass,

$$i = \frac{K_i - K_l}{K_i} \tag{7.1a}$$

and for monolithic glass,

$$i = \frac{K_i - K_m}{K_i} \tag{7.1b}$$

Obviously, the larger i, the better ability in absorbing the kinetic energy of projectile.

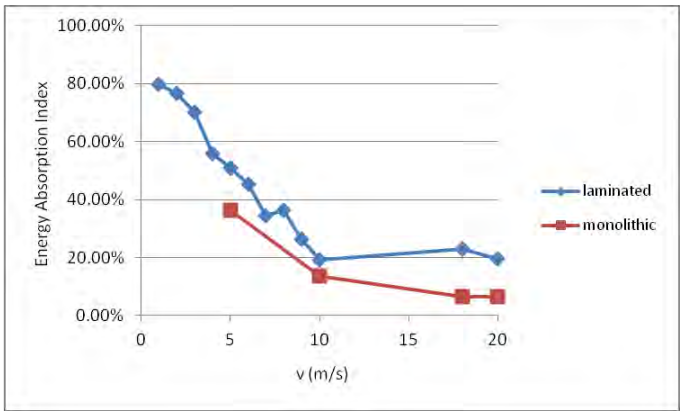

Figure 7.17 The trend of i ranged for laminated and monolithic glass from 1m/s to 20m/s

Figure 7.17 illustrated the trend i for both monolithic and laminated glass ranged from 1m/s

and 20m/s. Conclusion can be drawn that although the absolute reduced energy increased along with the increase of the impact velocity, the trend of i is decrease. Also, comparing with the monolithic glass, Figure 7.17 demonstrated again that laminated glass has better energy absorption capacity over monolithic glass.

The decrease of i can largely be attributed the role of PVB interlayer. For low impact velocity, the laminated glass experienced "glass controlled glass fracture". Since both the top and bottom glass layers were not severely damaged, the stiffness of glass held the whole laminated glass body well. Since the total kinetic energy K_i was not large in this stage and considerable amount was spent on the fracture of glass, i was kept at a high level. However, under high impact velocities, glass layer near the contact points failed quickly and were not able to resist further loading any longer. The whole laminated glass body was held together by the interlayer, and accordingly, this type of fracture can be defined as "PVB controlled glass fracture". The interlayer has large fracture energy and difficult to fracture. Meanwhile, the energy absorbed by the fracture of glass was limited, making i around 20% from 10m/s to 20m/s. This process is quite similar to the behaviour of the well-known reinforced concrete beam.

7.3.2 Bonding Condition

The interface between the glass and the interlayer enables each other adhered together and

make them work as a combined unit before it fails. In order to study the influences of the bonding condition on the behaviour of laminated glass, a variety of values of the interface strength (fracture energy) was used for evaluation.

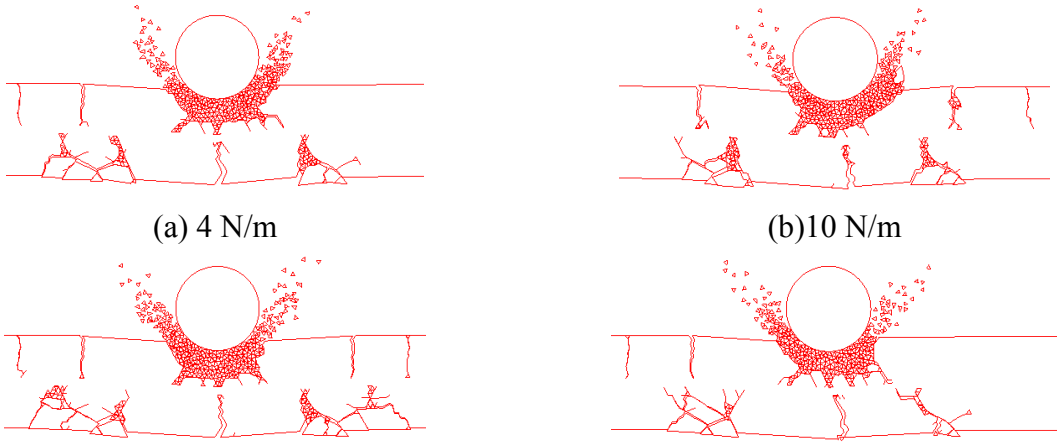

(a) 4 N/m (b)10 N/m

(c) 50 N/m (d) 100 N/m

Figure 7.18 Damage response of laminated glass with different interface strengths under 18m/s impact at t = 0.3ms

Figure 7.18 schematically showed the damage responses of the laminated glass beam under the impact of 18m/s at t = 0.3ms. The fracture capacity of the interface ranged from 4N/m (as small as glass is) to 100N/m. It can be observed from Figure 7.18 that in all the cases, the bending cracks have already propagated to the interface. Due to the ductility and flexibility of PVB interlayer, the fractured glass can be well adhered to the interlayer, which makes the crack difficult to propagate along the interface between the glass and interlayer. Among the examples studied, even the interface with 4N/m was able to resist the failure of itself, let alone examples with larger values.

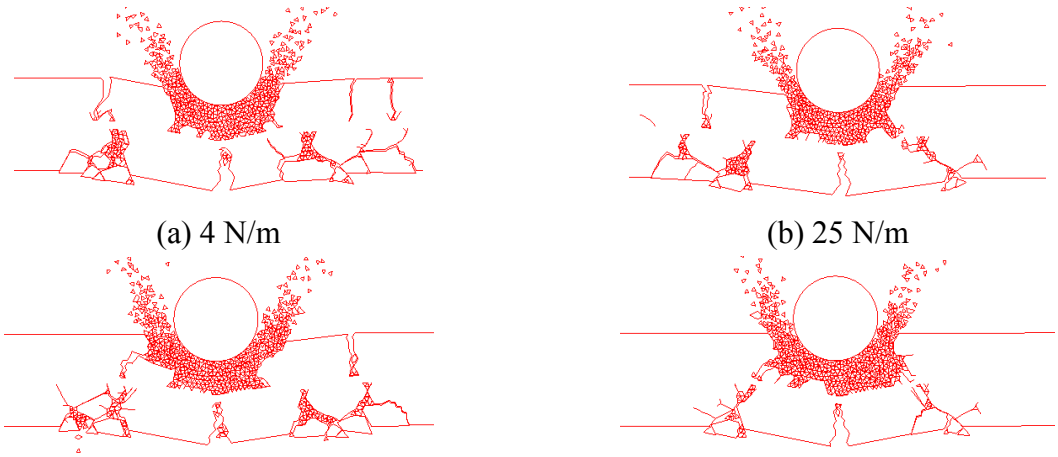

(a) 4 N/m (b) 25 N/m

(c) 50 N/m (d) 100 N/m

Figure 7.19 Damage response of laminated glass with different interface strengths under 30m/s impact at t = 0.3ms

Figure 7.19 schematically showed the damage responses of laminated glass beam under the impact of 30m/s at t = 0.3ms. Same range of the interface strength (4N/m to 100N/m) was chosen and similar conclusion can be reached as the impact of 18m/s does.

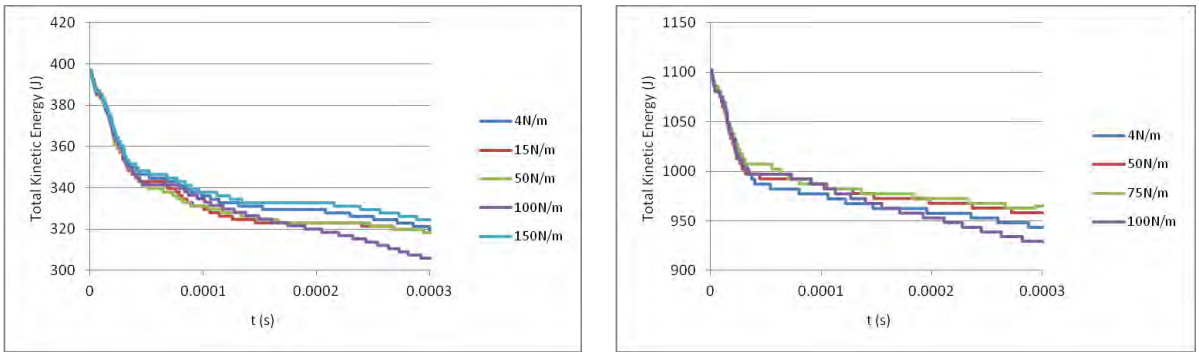

(a) 18m/s (b) 30m/s

Figure 7.20 The change of kinetic energy with different interface strengths under 18m/s and 30m/s impact within 0.3ms

The change of total kinetic energy under 18m/s and 30m/s impact within 0.3 ms were given in Figure 7.20 for different interface strengths. It can be observed that for both impact velocities, these bundles of curves with a variable interface reisitance were within a narrow band, which suggested that the interface strength did not play an important role in the fracture behaviour of laminated glass should the PVB interlayer is ductile enough. Since the PVB interlayer can deform considerably and be well adhered to the glass in most places, delaminatation is unlikely to occur. Figure 7.21 showed the responses of laminated glass under 18m/s at longer simulation time t = 2ms, and still no delamination can be observed although the PVB interlayer has undergone large deformation.

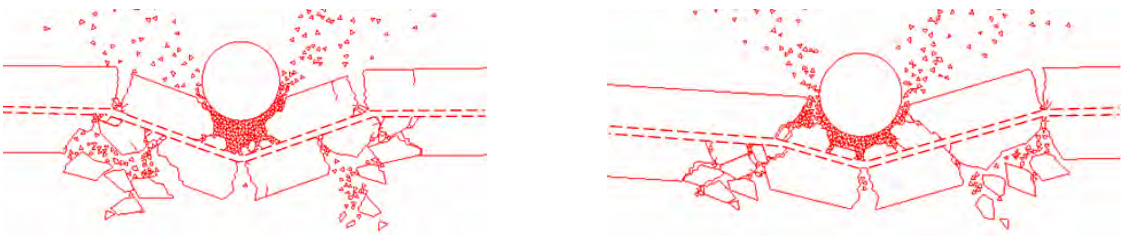

(a) 4N/m (b) 75N/m

Figure 7.21 The response of laminated glass with different strength of interface under 18m/s impact at t = 2ms

7.3.3 Interlayer Material

In this section, the young's modulus *E* of the interlayer will be studied. As in the previous study, the interlayer was adopted as the standard PVB where its material properties can be

found in Table 7.1. 100MPa was used as the Young's modulus E and 0.4 for the Poisson's ratio. In this section, investigation into the Young's modulus will be performed from 200MPa up to 200GPa.

According to the definition of the Young's modulus in Equation 7.2,

$$E = \frac{\sigma}{\varepsilon} \tag{7.2}$$

for a given stress σ, higher E requires a smaller strain ε to achieve equilibrium. In other words, the interlayer will become "stiff" with the increase of its Young's modulus.

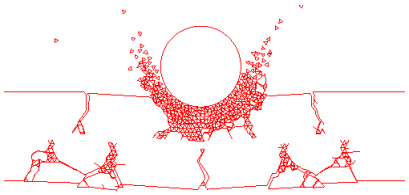

(a) E = 200MPa

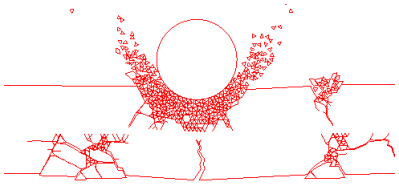

(b) E = 2GPa

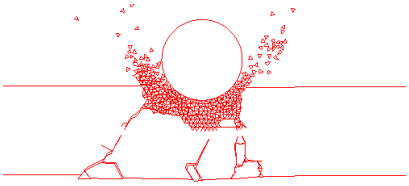

(c) E = 10GPa

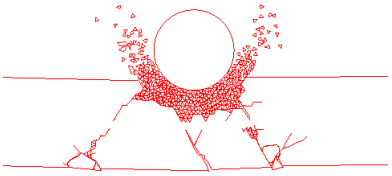

(d) E = 40GPa

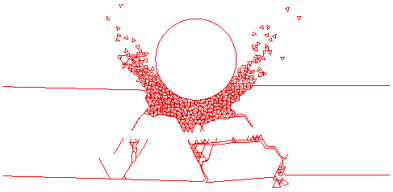

(e) E = 70GPa

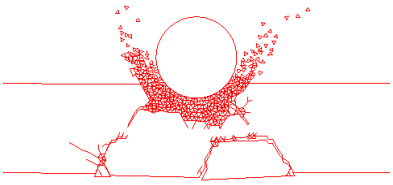

(f) E = 150GPa

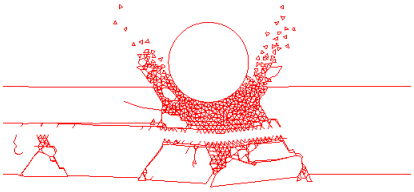

(g) E = 200GPa

Figure 7.22 Damage of laminated glass subject to 18m/s impact with different *E* at t = 0.3ms

Figure 7.22 gave the damage responses of laminated glass subjected to 18m/s ball impact at t = 0.3ms with different *E* selected from 200MPa to 200GPa. From that figure, conclusions can be drawn that four sections can be found which represent for different mechanisms. When *E* was no larger than 2GPa (Figure 7.22(a) and (b)), the damage patterns were similar to the results where *E* = 100MPa was used, which means the flexibility of the PVB interlayer was still dominant and most of the cracks in both top and bottom glass layers can be attributed to bending. When *E* was between 10GPa and 40GPa (Figure 7.22(c) and (d)), the interlayer exhibited some resistance to deformation, which resulted in a smaller damage area. When E was higher than 70GPa, delamination between the interlayer and glass started but not severe (Figure 7.22(e) and (f)). At *E* = 200GPa, delamination was typical in the damage. A further-developed delamination between glass and interlayer at t = 2ms was given in Figure 7.23 when 200GPa for *E* and 0.3 for the Poisson's ratio were used in the analysis.

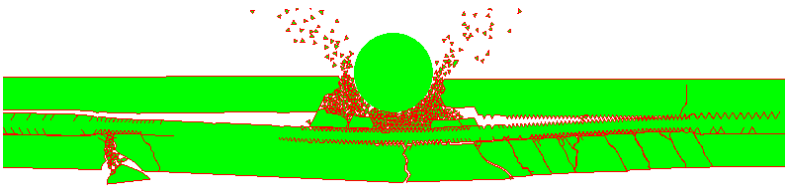

Figure 7.23 Delamination with the interface strength of 75N/m at t = 2ms under 18m/s impact

The change of i with different Young's modulus *E* of the interlayer was plotted in Figure 7.24 offers support to the different mechanisms that the laminated glass exhibited in Figure 7.22. The curves are wavy as different mechanisms were represented. Four sections (0.2-2,

5-40, 70-150, >200) can be roughly observed from Figure 7.24. The wavy effect cannot be eliminated even longer simulation was performed (Figure 7.24(b)).

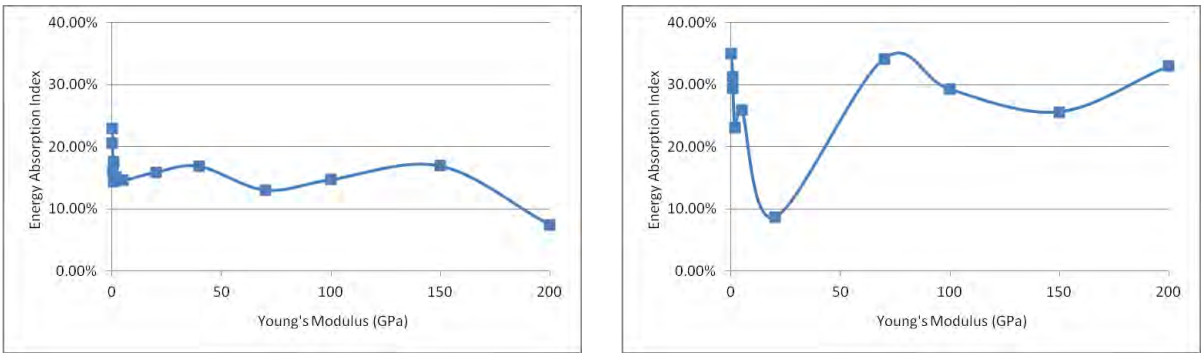

(a) t = 0.3ms (b) t = 1ms

Figure 7.24 Change of i with different Young's modulus E under 18m/s impact

Figure 7.25 provided the deformation curve for the centre of the laminated glass plate in section 7.2.3 when the PVB interlayer was replaced with one of steel property. By comparing with Figure 7.13(a), conclusions can be drawn that at t = 0.8ms, the z-displacement at the centre of the plate with PVB interlayer (14.26mm) is larger than that in Figure 7.25 (12.16mm).

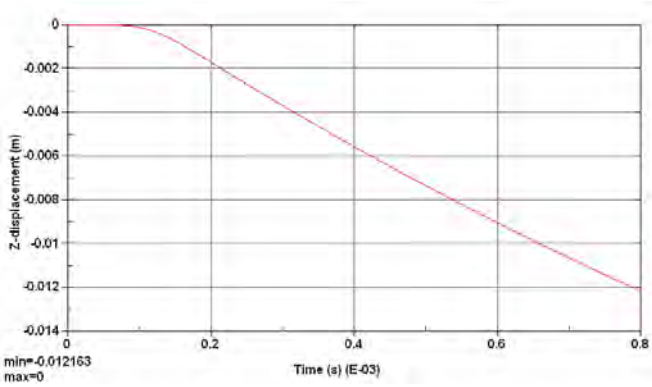

Figure 7.25 The z displacement of the centre of the laminated glass plate within 0.8 ms using

a steel interlayer

Should we look at the first section of Figure 7.24(b), the trend in energy absorption is clear almost linear descending as the first section of the curve was enlarged as shown in Figure 7.26. Since some "stiff" interlayer, such as SGP (about 1GPa), has started to be applied in the laminated glass, this suggested that laminated glass using such a stiff interlayer gets better control over the displacement at the expense of its energy absorption capacity.

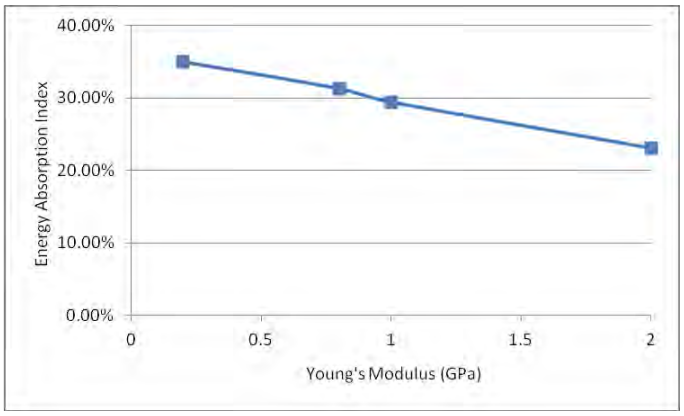

Figure 7.26 The change of i at t = 1ms with E from 0.2 to 2GPa

In general, both "soft" and "stiff" interlayers have advantages and diavantages. Different situations and applictions need different interlayer properties. For absorbing more energy, a soft interlayer (PVB) gives better performance over the stiff one, while for controlling the displacement and increasing the overall stiffness, a stiff interlayer (SGP) would be preferrable. The use of a stiff interlayer can increase the risk of delamination, where enough attention should be paid to.

7.4 Summary

This chapter performed the comparative and parametric study over the laminated glass through examples. In the comparative study section, results of laminated glass from the FEM/DEM were verified with the data from FEM and DEM (Flocker and Dharani, 1997b; Zang et al., 2007; Timmel et al., 2007).

(1) In the 2D comparison with Flocker and Dharani (1997b), a different angle of cone crack was obtained from the FEM/DEM along with some crushing near the contact point, which was not available in the FEM simulation. Either fine-debris or the appearance of median and lateral cracks indicated that FEM/DEM is producing genuine dynamic simulation while FEM yielded an expression of static loading.

(2) When comparing with the DEM results from Zang et al. (2007), agreement was achieved in general scenario, while some differences existed. More small fragments were obtained from the FEM/DEM and some large glass fragments were found after the fracture of the interlayer.

(3) The 3D laminated glass plate agrees well in both the crack pattern and z displacement with the results of Timmel et al. (2007) using the LS-DYNA solver. Although only results at t = 0.8

ms was shown, it is believed that the trend of the response will lead to satisfactory in the end.

In the parametric study section, input energy, bonding strength as well as the Young's modulus of interlayer were investigated, yielding some useful conclusions in design and manufacture. Details were given below.

(1) In the input energy study, index i was used to evaluate the advantage of laminated glass over monolithic and the energy absorption capacity, respectively. The concepts of "glass controlled glass fracture" and "PVB controlled glass fracture" were proposed, leading the study into the similar way that has been well understood in the reinforced concrete.

(2) The interface between the interlayer and glass did not play an important role in the failure of laminated glass when a soft PVB interlayer was used. The interlayer was well deformed and adhered to the glass, preventing the crack that has already reach the interface by bending develop longitudinally.

(3) Regarding the Young's modulus, a "stiff" interlayer (such as SGP) can have better control over the displacement, but the risk of delamination can be increased accordingly. On the contrary, applying a "soft" interlayer can improve the performance in absorbing the kinetic energy, at the expense of larger deformation and displacement. It would be a good idea to determine which kind of interlayer to use on a case-by-case basis.

In conclusion, the study in this chapter verified the reliability of the FEM/DEM in simulating the laminated glass subject to impact.

CONCLUSIONS AND RECOMMENDATIONS FOR FUTURE WORK

This chapter will summarise the work in the thesis and concluded the outcomes. Also, improvements that can be made to the FEM/DEM and future simulation are addressed.

The aims and objectives proposed in chapter one all have been achieved. In this thesis, the fracture behaviour of monolithic and laminated glass under hard body impact was simulated using the FEM/DEM. The FEM/DEM is relatively new. Despite some application in limited areas (such as rock failure and molecular dynamics), as far as the author is aware of, this is the first time that this method has been applied into the glass and laminated glass fracture analysis.

New fracture models for glass and laminated glass were also developed. Besides the Mode I fracture model already available in the FEM/DEM program Y, two mixed-mode (I + II) fracture models (the elasto-plastic and scaling models) were developed and studied in depth. The elasto-plastic model was developed for the glass as well as the interface between the glass and interlayer in laminated glass. The scaling model was developed based on the reduction of stress from the Mode I strain-softening curve. Comparison between these two models showed that the elasto-plastic model is more suitable for FEM/DEM simulation while some modifications are still required for the scaling model.

The parametric studies on glass and laminated glass were performed. Using the Mode I and elasto-plastic damage models, a range of parameters, including the fracture energy, tensile strength and impact velocity were investigated and their influences on the response and the fracture pattern of glass were studied. Tensile strength, fracture energy and the thickness were considered as the top three factors in controlling the performance of monolithic glass. For laminated glass, better energy absorption capacity over monolithic glass was shown and the relationship between the stiffness of interlayer and delamination was established.

8.1 Conclusions

The aim of this thesis is to analyse the fracture of glass under impact by using the FEM/DEM. In chapter 2, studies on the literatures of glass fracture reviewed the methods that used to investigate the problem. By comparing with experimental and other numerical methods, the FEM/DEM was demonstrated as a suitable method for crack initiation and propagation in glass.

Regarding the monolithic glass, a Mode I cracking model was developed in chapter 4, and be applied in the fracture analysis. The model was modified in such way that the strain softening curve has been adapted to glass. The model has shown good convergence with the refinement of element mesh, small enough time step and large enough penalty parameters. In the numerical examples computed, a cone type crack was obtained in 2D with considerable

number of elements along the direction of thickness. In 3D, for coarse mesh with one layer along the thickness, the damage was mainly localised within the impact effective area (section 4.5.2). With the increase of layers of elements along thickness, more bending can be obtained and radial cracks were observed in the example with four element layers. This is largely a numerical issue. For a specific plate, the bending capacity is intrinsic and will not change under the same impact velocity. If the plate is considered as an assembly of discrete elements, physically these elements have to be very small (at the atomic level). For FEM/DEM simulation, bending cracks can be obtained when the plate can undergo some out-of-plane deformation as a whole.

Parametric study on the monolithic glass was performed in chapter 5 following the Mode I crack modelling. Tensile strength, fracture energy and thickness were considered the top three parameters that can improve the performance of monolithic glass under impact. Higher tensile strength will make glass more resistant to fracture and penetrate while larger fracture energy can improve the ductility to resist the brittleness. The energy thresholds ($\frac{1}{2}mv^2$) of each type of damage against the fracture resistance ($G_f h$) were given, schematically presented the regimes from minor local crack to punching failure with the increase of impact velocity. According to the study, the cone and punching would be common in practice. Also the relationship between fracture pattern and the reflection of stress waves was revealed: for glass block with large thickness, reflected stress wave is too weak to make any meeting crack; for glass beam, this meeting crack can be obtained. Since the bending stiffness (*EI*) is a function

of the cube of the thickness, increase the thickness of glass (h) can improve the performance greatly. Before fracture, h can control the flexural deformation of the beam and at least postpone the occurrence of main central crack. After fracture, large h (larger than the characteristic length of projectile) can help prevent the further damage and penetration.

Two mixed-mode fracture models were developed in chapter 6: the elasto-plastic model and the scaling model. These models have been studied and discussed in details. For the elasto-plastic fracture model, mixed-mode was considered. Ball impact and in-plane shearing problems were analysed and results were compared with that from the Mode I fracture model developed in chapter 4 and some similarities were found. The results from the elasto-plastic model were verified with uniaxial compression tests from Shen et al. (1995). The similarity of results between the elasto-plastic model and the Mode I model has been investigated and attributed to the dominance of Mode I affect in glass fracture. Parametric study on the shape of yield ellipse was performed for the elasto-plastic model, reaching the conclusion that higher shear strength will make the crack be prone to propagate perpendicular to the load axis.

For the scaling model, since the strain softening curve was reduced by the artificial scaling factor, the actual fracture energy required for the fracturing was smaller than that of Mode I model. The limitation of the scaling model that stress may violate the basic law of cohesive model while loading in softening zone was also has been discussed. Currently, the scaling model is not suitable for modelling the impact on glass. Further modification is needed to

make sure the stress is correct and unloading be considered should the model be used for the analysis.

Laminated glass was simulated in both 2D and 3D and parametric study was performed in chapter 7. The results were compared and verified with data from FEM, DEM and experimental test. For comparison with the FEM, a different cone angle was obtained. With both the production of fine-debris and the appearance of median and lateral cracks, it is clear that FEM/DEM is modelling genuine dynamic simulation. The comparison with the DEM showed that the results from the FEM/DEM are more realistic, as the FEM/DEM yielded a more accurate estimate in stress and deformation than DEM did. Radial-tangential cracks were produced from the 3D laminated glass plate, reaching the similarity with the results from the FEM.

Influences of parameters including the input energy, bonding strength as well as the Young's modulus of interlayer were investigated and conclusions were reached: (1) laminated glass can absorb more kinetic energy from the projectile than monolithic glass due to the ductility of interlayer. (2) For laminated glass with a flexible interlayer, delamination is difficult to occur since the interlayer can endure large deformation and hold the fractured glass together well. (3) A "stiff" interlayer (such as SGP) can have better control over the displacement, but the risk of delamination can increase accordingly. The delamination behaviour when E = 200GPa is very obvious.

8.2 Future Work

Although some works have been done using the FEM/DEM as well as the glass fracture analysis in this thesis, there is still a lot to be improved in the future. This section is focused on the improvement on the FEM/DEM modelling and further analysis on the glass fracture problems.

8.2.1 The FEM/DEM Program

During the numerical analysis of fracture on glass under impact, the FEM/DEM program has been verified and demonstrated its applicability and reliability. However, since the current FEM/DEM program is a research program and still under development, there is a lot of improvements that can be made to enable the FEM/DEM program work better.

(1) Parallel Computation

The FEM/DEM program is slow. On average, it costs 5 μs per element per time step in 2D, while this increases dramatically to 300 μs in 3D (under windows XP platform, 2.66GHz CPU clock speed). A faster execution is urgently needed in 3D and such problem has already been raised in this thesis. In chapter 7, the 3D laminated glass will cost 40 weeks of computational time to complete 40ms of simulation, which would not be acceptable in

engineering computation.

Figure 8.1 showed the time (s) needed for each time step with different number of elements. It can be observed that for both 2D and 3D, the computation time increases almost linearly with the number of elements. This may restrict the large-scale simulation with great number of elements. Since the current FEM/DEM program is serial, one thing that can do in the future is paralleling the program on high performance computation (HPC) facilities using MPI technique. The advantages of the FEM/DEM can be much more obvious with the support of HPC parallel computing. As FEM/DEM is an explicit method, it is ideally suited for parallel computing.

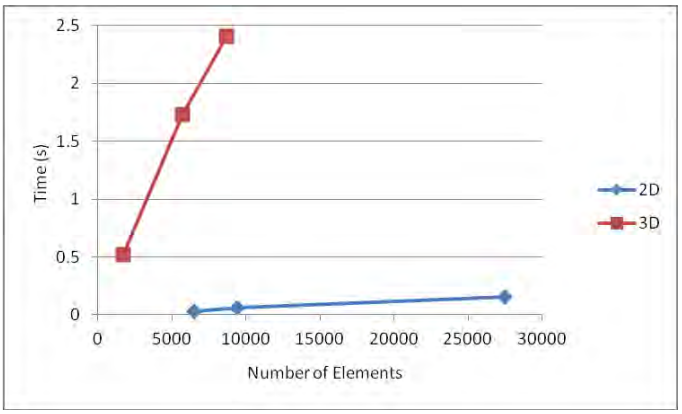

Figure 8.1 The computation time of each step (s) for different numbers of elements

(2) New element types

There are only two types of elements available in the current FEM/DEM program: constant strain triangle in 2D and constant strain tetrahedron in 3D. Since these two elements are the simplest type so far, computational time can be saved to some extent as the contact detection

and interaction is simpler. However, comparing with others elements, the shortcomings of the current available types of elements are also obvious.

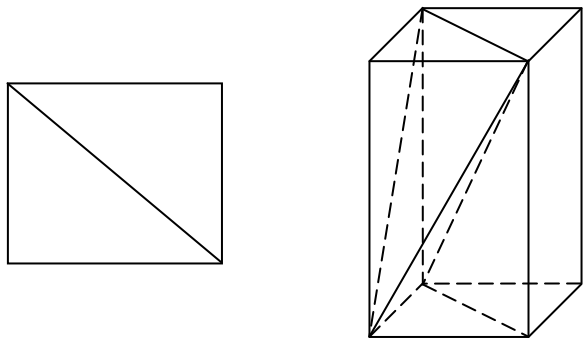

Fig 8.2 The reduction of element numbers by using rectangle in 2D and cube in 3D

One of the drawbacks is that more number of elements has to be used. From Figure 8.2, two triangles are needed for each rectangle, while five to six tetrahedrons for every parallel hexahedron. Thus implementing new rectangular and hexahedron elements can reduce the total number of elements. Also, higher order elements have advantage in deformation and representing, for instance, bending stress fields, which can make the analysis more accurate. New fracture criteria and interface elements accompanied with higher order discrete elements should also be considered. For higher order elements, the joint elements may change shape and more integration points need to be incorporated. With more integration points, the distribution of fracture energy amongst them would also have to be considered. The implementation of contact detection as well interaction in original FEM/DEM also has to be updated since the element shape may be changed and element side may no longer be straight.

(3) A unified pre/post-processing environment

The pre and post-processing environment needs to be improved. The current 2D post-processing program M is mainly for demonstration. Although Paraview was used in the latest 2D version, the output data package should be updated to contain more physical values for the convenience of analysis. And same applies to the 3D Ls-Pre/Post.

Comparing with the post-processing, pre-processing in the FEM/DEM program need more support. In this thesis, structures and meshes were set up and created in ABAQUS CAE, then transferred to the FEM/DEM format, which costs considerable time and may introduce errors. Should a unified FEM/DEM CAE environment be established, the efficiency of analysis can be greatly improved.

(4) Re-meshing property

The element meshes need to be assigned in the current FEM/DEM analysis before hand, so that cracks can initiate and propagate along the edges of two adjacent elements. However, sometimes the mesh generated by the user is not the best one that can reflect the real stress distribution within the object and re-meshing can be considered in this circumstance.

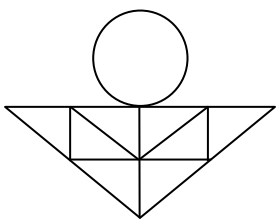

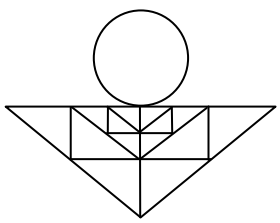

(a) Before re-meshing (b) After re-meshing

Figure 8.3 Mesh before and after re-meshing

Figure 8.3 illustrated the change of mesh after the re-meshing. Within one time step, the FEM/DEM should be designed to detect which elements are in contact, and then the related elements can be refined according to some algorithm. Thus a new mesh topology will be generated and passed onto the next step. By using the re-meshing, a coarse mesh can be used at the beginning of the computation, while FEM/DEM can adaptively refine itself to include necessary elements, leading to a better performance. It should be noted that re-meshing is usually an expensive approach, and the increased computation time should be assessed to see whether it will offset the obtained efficiency or not.

(5) Restart file

There is no restart file in the current FEM/DEM program. If the execution breaks down due to any unexpected incident before the end of the computation, the user has to start from the beginning. This poses high risk to computation. Since the database of FEM/DEM is updated after each time step, the restart file can be generated at a certain frequency. Instead of starting from the beginning, the user can continue the problem from the backup point by using the latest restart file. The restart file is also helpful when the total computation time is too long to be completed in one batch job. A large job can be decomposed into several small ones, and restart files can be used to link them together.

8.2.2 Glass Impact Analysis

On the side of glass fracture analysis, there is also some work that can be done in the future.

(1) Following up modelling

Although new models were developed in this thesis, they are still relatively simple. Modifications and improvements would be needed to make the models more reliable and usable under different situations. Improvement for the scaling model is needed to enable unloading and make sure that the basic principle of cohesive model is adhered to. Besides cohesive model, other model can be considered and new fracture criteria can be incorporated so that comparison can be made between different models and the most appropriate one for the fracture of glass can be determined.

(2) Further comparison with experiments

Despite of the verification in this thesis, further comparison with results from experimental test is necessary. The results of the FEM/DEM should be compared directly with the experimental data, which is part of reality. Some aspects that have not been well explored in this thesis, such as the resulting cone angle and resulting deformation rate, should be studied further.

(3) Modelling glass with pre-stress

In this thesis, the type of glass is restricted to the ordinary soda lime glass with no pre-stress. Future study can include some other glass types, like the toughened glass as it is also widely used in civil and automobile engineering. The existence of pre-stress will enable the glass to take higher load and break up into small dices when damaged, which is quite different from the fracture patterns currently obtained.

(4) Soft body impact

In this thesis, a typical hard body (usually steel ball) was used as the projectile. Apart from that, soft body impact is also important in everyday life. The investigation on the fracture of glass under impact can be extended to these soft impacts with longer contacting time and larger deformation of the projectile.

(5) Repeated load

Glass subjects to repeated or cyclic load can be considered in the further study. In military area, laminated safety glass subject to repeated explosion within a short time is common. It is a challenge for glass to resist such repeated impact waves as the previous wave may have an adverse effect on the resistance that the glass can provide for second wave. In civil engineering, serials of impacts on the glass or laminated glass are possible in a strong wind, and attention can be paid to.

Although there are some guidance and standard on the design of glass and laminated glass,

current fracture theory of glass under impact is far from well-established. This thesis applied the FEM/DEM into that analysis, provided a new perspective apart from the traditional FEM or DEM software package. With the development of the software and hardware, the analysis future by using the FEM/DEM can be applied even more widely.

REFERENCES

Adams, M. and Sines, G., 1978. A statistical, micromechanical theory of the compressive strength of brittle materials. *Journal of the American Ceramic Society*, 61, 126-131.

Anderson, T. L., 1991. Fracture mechanics: fundamentals and applications. 2nd ed. Boca Raton: CRC Press.

Andrews, J. P., 1931. Experiments on impact. *Proceedings of the Physical Society*, 43(1), 8-17.

Areias, P.M.A. and Belytschko. T., 2005. Analysis of three-dimensional crack initiation and propagation using the extended finite element method. *International Journal for Numerical Methods in Engineering*, 63(5), 760-788.

Axinte, E., 2011. Glasses as engineering materials: A review. *Materials&Design*, 32(4), 1717-1732.

Ayatollahi, M. R. and Aliha, M. R. M, 2009. Mixed mode fracture in soda lime glass analyzed by using the generalized MTS criterion. *International Journal of Solids and Structures*, 46, 311-321.

Baird, K.M., 1947. Shock wave in glass. *Nature*, 160, 24-25.

Ball, A. and McKenzie, H., 1994. On the low velocity impact behaviour of glass plates. *Journal of Physics IV*, C8-4, 783-788.

Bangash, T. and Munjiza, A., 2003. Experimental validation of a computationally efficient beam element for combined finite–discrete element modelling of structures in distress. *Computational Mechanics*, 30, 366-373.

Barenblatt, G. I., 1959. Equilibrium cracks formed during brittle fracture rectilinear cracks in plane plates. *Journal of Applied Mathematics and Mechanics*, 23(4), 706-721.

Barenblatt, G. I., 1962. The mathematical theory equilibrium cracks in brittle fracture. *Advances in Applied Mechanics (edited by Richard Von Mises, Theodore Von Karman)*, 55-129.

Barkai, O., Menouillard, T., Song, J. - H., Belytschko, T. and Sherman, D., 2012. Crack initiation and path selection in brittle specimens: A novel experimental method and computations. *Engineering Fracture Mechanics*, 89, 65–74.

Barsom, J. M., ed., 1987. Fracture mechanics retrospective. Philadelphia: American society for testing and materials.

Bazant, Z. P., 1976. Instability, ductility and size effect in strain softening concrete. *Journal of the Engineering Mechanics Division*, 102(2), 331-344.

Bazant, Z. P. and Cedolin, L, 1979. Blunt crack band propagation in finite element analysis. *Journal of the Engineering Mechanics Division*, 105(2), 297-315.

Bazant, Z. P. and Cedolin, L., 1980. Fracture mechanics of reinforced concrete. *Journal of the Engineering Mechanics Division*, 106(6), 1287-1306.

Bažant, Z. P. and Kim, S-S., 1979. Plastic-fracturing theory for concrete. *Journal of the Engineering Mechanics Division* (ASCE), 105(3), 407-428.

Bažant, Z. P. and Oh, B. H., 1983. Crack band theory for fracture of concrete. *Materials and Structures*, 16(3), 155-177.

Behr, R. A. and Kremer, P. A., 1996. Performance of laminated glass units under simulated windborne debris impacts. *Journal of Architectural Engineering*, 2(3), 95-99.

Behr, R. A., Minor, J. E. and Linden, M. P., 1986. Load duration and interlayer thickness effects on laminated glass. *Journal of Structural Engineering ASCE*, 112(6), 1141-1153.

Behr, R. A., Minor, J. E. and Norville, H. S., 1993. Structural behaviour of architectural laminated glass. *Journal of Structural Engineering*, 119(1), 202-222.

Behr, R. A., Minor, J. E., Linden, M. P. and Vallabhan, C. V. G., 1985. Laminated glass units under uniform lateral pressure. *Journal of Structural Engineering ASCE*, 111(5), 1037-1050.

Belytschko, T., Lu, Y. Y. and Gu, L., 1994. Element-free Galerkin methods. *International Journal for Numerical Methods in Engineering*, 37, 229–256.

Belytschko, T. and Black, T., 1999. Elastic crack growth in finite elements with minimal remeshing. *International Journal for Numerical Methods in Engineering*, 45, 601–620.

Bennison, S. J., Smith, C. A., Van Duser, A. and Jagota, A., 2002. Structural Performance of Laminated Glass Made With a “Stiff” Interlayer. Glass in Buildings, ASTM STP 1434, V Block, ed., ASTM International, West Conshohocken, PA, 57-64.

Bisrat, Y. and Roberts, S. G., 2000. Residual stress measurement by Hertzian indentation. *Materials Science and Engineering: A*, 288(2), 148–153.

Bouzid, S., Nyoungue, A., Azari, Z., Bouaouadja, N. and Pluvinage, G., 2001. Fracture criterion for glass under impact loading. *International Journal of Impact Engineering*, 25(9), 831–845.

Burchell, M. J. and Grey, I. D. S., 2001. Oblique hypervelocity impacts on thick glass targets. Material Sciences and Engineering, A303, 134-141.

Calderone, I. and Melbourne, W. H., 1993. The behaviour of glass under wind loading. Journal of Wind Engineering and Aerodynamics, 48, 81-94.

Camacho, G. T. and Ortiz, M., 1996. Computational modeling of impact damage in brittle materials. *International Journal of Solids and Structures*, 33, 2899–2938.

Carranza, F. L., Fang, B. and Haber, R. B., 1997. A moving cohesive interface model for fracture in creeping materials. *Computational Mechanics*, 19, 517-521.

[Cantilevered glass canopy, Tokyo] n.d. [image online] Available at: < http://www.lusas.com/case/civil/cantilevered.html > [Accessed 27 January 2013]

CEB–FIP Model Code, 1990. Bulletind Information No. 190a, 190b, Comite Euro

International du Beton (CEB), Lausanne.

Celik, M., 2001. Elasto-plastic behaviour of isotropic stepped plates. *Engineering Analysis with Boundary Elements*, 25, 455-460.

Ceriolo, L. and Tommaso, A. D., 1998. Fracture mechanics of brittle materials: a historical point of view. 2nd International PhD symposium in Civil Engineering, Budapest.

Cervera, M. and Chiumenti, M., 2006. Smeared crack approach: back to the original track. *International Journal for Numerical and Analytical Methods in Geomechanics*, 30(12), 1173–1199.

Chai, H. and Ravichandran, G., 2009. On the mechanics of fracture in monoliths and multilayers from low-velocity impact by sharp or blunt-tip projectiles. *International Journal of Impact Engineering*, 36, 375-385.

Chandra, N., Li, H., Shet, C. and Ghonem, H., 2002. Some issues in the application of cohesive zone models for metal–ceramic interfaces. *International Journal of Solids and Structures*, 39, 2827–2855.

Chang, J., Xu, J. and Mutoh, Y., 2006. A general mixed-mode brittle fracture criterion for

cracked materials. *Engineering Fracture Mechanics*, 73, 1249-1263.

Chaudhri, M. M. and Kurkjian, C. R., 1986. Impact of small steel spheres on the surfaces of "normal" and "anomalous" glasses. *Journal of the American Ceramic Society*, 69(5), 404-410.

Chen, J., 2012. Indentation-based methods to assess fracture toughness for thin coatings. *Journal of Physics D: Applied Physics*, 45, 203001.

Chen, X., Chan, A. H. C. and Yang, Y., 2010. A case study of impact on glass using the combined finite-discrete element method. *DEM5 Munjiza A. (ed.)*, 465-469.

Chen, X., Chan, A. H. C. and Yang, Y., 2012. Investigation on impact damage of glass using combined finite-discrete element method. Proceedings of the 20th UK Conference of the Association for Computational Mechanics in Engineering, Manchester, 227-230.

Clarke, D. R. and Faber, K. T., 1987. Fracture of ceramics and glasses. *Journal of Physics and Chemistry of Solids*, 48(11), 1115-1157.

Clough, R. W., 1960. The finite element method in plane stress analysis. *Proceeding of. 2nd ASCE Conference on Electronic*. *Computation*, Pittsburgh, Pa.

Clough, R. W., 1979. The finite element method after twenty-five years – a personal view. Engineering Application of the finite element method, Hovik, Norway, 1.1-1.34.

Cook, R. F. and Pharr, G. M., 1990. Direct observation and analysis of indentation cracking in glasses and ceramics. *Journal of the American Ceramic Society*, 73(4), 787-817.

Costin, L. S., 1989. Time-dependent deformation and failure. Fracture Mechanics of Rock. London: Academic Press.

Cour-Palais, B. G., 1987. Hypervelocity impact in metals, glass and composites. *International Journal of Impact Engineering*, 5, 221-237

Crisfield, M. A., 1991. Non-linear finite element analysis of solids and structures. Volume 1. John Wiley and Sons.

Cundall, P. A. and Hart, R. D., 1992. Numerical modelling of discontinua, *Engineering computations*, 9, 101-113.

Cundall, P. A. and Strack, O. D. L., 1979. A discrete numerical model for granular assemblies. *Geotechnique*, 29(1), 47-65.

Daux, C., Moes, N., Dolbow, J., Sukumar, N. and Belytschko, T., 2000. Arbitrary branched and intersecting cracks with the extended finite element method. *International Journal for Numerical Methods in Engineering*, 48, 1741–1760.

Dawson, S., 1995. Glass as a skin and structure. *Architects' Journal*, 32-34.

Dawson, S., 1997. Glass breaks a new barrier. *Architects' Journal*, 37-39.

de Borst, R., 1987. Computation of post-bifurcation and post-failure behaviour of strain-softening solids. *Computers and Structures*, 25, 211–224.

de Borst, R., Remmers, J. C., Needleman, A. and Abellan, M-A., 2004. Discrete vs smeared crack models for concrete fracture: bridging the gap. *International Journal for Numerical and Analytical Methods in Geomechanics*, 28, 583–607.

Delincé, D., Callewaert, D., Belis, J. and Van Impe, R., 2008. Post-breakage behaviour of laminated glass in structural applications. Challenging Glass conference on architectural and structural applications of glass, Veer B. L.(ed), 459-466.

Dhaliwal, A. K. and Hay, J. N., 2002. The characterization of polyvinyl butyral by thermal analysis. *Thermochimica Acta*, 391, 245–255.

Dharani, L. R., Yu, J., 2004. Failure Modes of Glass Panels subjected to soft missile impact. In Damage and Fracture VIII, Edited by C.A. Brebbia and A. Varvani-Farahami, WIT press, 163-171.

Dharani, L. R., Wei, J., Yu, J., Minor, J. E., Behr, R. A. and Kremer, P. A., 2005. Laminated architectural glass subjected to blast impact loading. *American Ceramic Society Bulletin*, 84(1), 42-44.

Dodd. G.., 1999. The design of a tall, ground based glass wall, stabilised by laminated glass fins. Proceedings of the Sixth International Conference on Architectural and Automotive Glass, Tampere, Finlandm

Dolbow, J., Moes, N. and Belytschko, T., 2000. Modelling fracture in Mindlin–Reissner plates with the extended finite element method. *International Journal of Solids and Structures*, 37, 7161–7183.

Dolbow, J., Moes, N. and Belytschko, T., 2001. An extended finite element method for modeling crack growth with frictional contact. *Computer Methods in Applied Mechanics and Engineering*, 190, 6825–6846.

Dougill, J. W., 1976. On stable progressively fracturing solids. *Journal of Applied Mathematics and Physics (ZAMP)*, 27, 423-437.

Du Bois, P. A., Kolling, S. and Fassnacht, W, 2003. Modelling of safety glass for crash simulation. *Computational Material Science*, 28, 675-683.

Duarte, C. A., Babuska, I. and Oden, J. T., 2000. Generalized finite element methods for three dimensional structural mechanics problems. *Computers & Structures*, 77, 215–232.

Dugdale, D. S., 1960. Yielding of steel sheets containing slits. *Journal of the Mechanics and Physics of Solids*, 8, 100-104.

Dussubieux, L., Gratuze, B and Maryse, B. L., 2010. Mineral soda alumina glass: occurrence and meaning. *Journal of Archaeological Science*, 37, 1646-1655.

Elaguine, D., Brudieu, M. A. and Storåkers, B., 2006. Hertzian fracture at unloading. *Journal of the Mechanics and Physics of Solids*, 54(11), 2453-2473.

Elices, M., Guinea, G. V., Gomez, J. and Planas, J., 2002. The cohesive zone model: advantages, limitations and challenges. *Engineering Fracture Mechanics*, 69, 137-163.

Erdogan, F and Sih, G. C., 1963. On the crack extension in plates under lane loading and transverse shear. *Journal of Basic Engineering*, ASME 85, 519-527.

Field, J., Walley, S., Bourne, N. and Huntley, J., 1994. Experimental methods at high rates of strain. *Journal de Physique IV,* 4, C8-3-C8-22.

Field, J. E., Walley, S. M., Proud W. G., Goldrein, H. T. and Siviour, C. R., 2004. Review of experimental techniques for high rate deformation and shock studies. *International Journal of Impact Engineering*, 30(7), 725–775.

Fisher-Cripps, A. S., 2007. Introduction to contact mechanics. Springer.

Flocker, F. W. and Dharani, L. R., 1997a. Stress in laminated glass subject to low velocity impact. *Engineering Structure*, 19 (10), 851-856.

Flocker, F. W. and Dharani, L. R., 1997b. Modelling fracture in laminated architectural glass subject to low velocity impact. *Journal of Material Science*, 32, 2587-2594.

Foote, R. M. L., Mai, Y-W and Cotterell, B., 1986. Crack growth resistance curves in strain-softening materials. *Journal of the Mechanics and Physics of Solids*, 34(6), 593–607.

Geandier, G., Denis, S. and Mocellin, A., 2003. Float glass fracture toughness determination by Hertzian contact: experiments and analysis. *Journal of Non-Crystalline Solids*, 318(3), 284-295.

Glathart, J. L. and Preston, F. W., 1968. The behaviour of glass under impact: theoretical considerations . *Journal of the Society of Glass Technology*, 9, 89-100.

Goodfellow, A. M. and Schleyer, G. K., 2003. Experimental investigation of corner-supported architectural glazing under pulse pressure loading. *Journal of Strain Analysis*, 38(5), 469-481.

Gorham, D. A. and Salman, A. D., 1999. Indentation fracture of glass and mechanisms of material removal. *Wear*, 233-235, 151-156.

Gogotsi, G. A. and Mudrik, S. P., 2010. Glasses: New approach to fracture behavior analysis. *Journal of Non-Crystalline Solids*, 356, 1021-1026.

Grant, P. V., Cantwell, W. J., McKenzie, H. and Corkhill, P., 1998. The damage threshold of laminated glass structures. *International Journal of Impact Engineering*, 21(9), 737-746.

Griffith, A. A., 1920. The phenomena of rupture and flow in solids. *Philosophical Transactions, Series A*, 221, 163-198.

Griffith, A. A., 1924. The theory of rupture. Proceedings of the First International Congress of Applied Mechanics, Delft, 55-63.

Griffiths, D. V. and Mustoe, G. G. W., 2001. Modelling of elastic continua using a grillage of structural elements based on discrete element concepts. *International Journal for Numerical Methods in Engineering*, 50(7), 1759–1775.

Grujicic, M., Pandurangan, B., Coutris, N., Cheeseman, B. A., Fountzoulas, C., Patel, P., Templeton, D. W. and Bishnoi. K. D., 2009. A simple ballistic material model for soda-lime glass. *International Journal of Impact Engineering*, 36, 386-401.

Guz, A. N. and Nazarenko, V. M., 1989a. Fracture mechanics of material in compression along cracks (review)-highly elastic materials. *International Applied Mechanics*, 25(9), 851-876.

Guz, A. N. and Nazarenko, V. M., 1989b. Fracture mechanics of materials under compression along cracks (survey)-structural materials. *International Applied Mechanics*, 25(10), 959-972.

Hayakawa, K., Murakami, S. and Liu, Y., 1998. An irreversible thermodynamics theory for elastic-plastic-damage materials. *European Journal of Mechanics - A/Solids*, 17(1), 13-32.

Haag, M. G. and Haag, L. C., 2006. Shooting incident reconstruction. Academic Press Inc.

Hegen, D., 1996. Element-free Galerkin methods in combination with finite element approaches. *Computer Methods in Applied Mechanics and Engineering*, 135, 143–166.

Hertz, H., 1896. On the contact of elastic solids. London: Macmillan.

Hill, G. R., 1982. Proposed demountable squash courts with glass walls. *The Structural Engineer*, 60A(3), 78-85.

Hills, D. A. and Sackfield, A., 1987. The stress field induced by normal contact between dissimilar spheres. *Journal of Applied Mechanics*, 54, 8-14.

Hillerborg, A., Modéer, M. and Petersson, P. E., 1976. Analysis of crack formation and crack growth in concrete by means of fracture mechanics and finite elements. *Cement and Concrete Research*, 6(6): 773-781.

Hocking, G., 1992. The discrete element method for analysis of fragmentation of discontinua.

Engineering Computations, 9(2), 145 – 155.

Hocking, G., Mustoe, G. G. W and Williams, J. R., 1985. Validation of the CICE discrete element code for ice ride-up and ice ridgecone interaction. In ASCE Specialty Conference, \ARCTIC '85", San Francisco.

Hoek, E. and Bieniawski, Z. T., 1965. Brittle fracture propagation in rock under compression. *International Journal of Fracture Mechanics*, 1, 137-155.

Holloway, D. G., 1968. The fracture of glass. *Physics Education*, 3, 317-322.

Hopper, J. A., 1973. On the bending of architectural laminated glass. *International Journal of Mechanical Sciences*, 15, 309-323.

Hooper. P. A., Sukhram, R. A. M., Blackman, B. R. K. and Dear J. P., 2012. On the blast resistance of laminated glass. *International Journal of Solids and Structures*, 49, 899-918.

Hopkinson, B. A., 1914. Method of measuring the pressure produced in the detonation of high explosives or by the impact of bullets. *Proceedings of the Royal Society A*, 213, 437–456.

Hopkinson, J., 1872. On the rupture of iron wire by a blow. *Proceedings of the Manchester Literary and Philosophical Society*, XI, 40–45.

Horii, H and Nemat-Nasser, S., 1986. Brittle fracture in compression: splitting, faulting and brittle-ductile transition. *Philosophical Transactions of the Royal Society of London. Series A, Mathematical and Physical Sciences*, A319, 337-374.

Huber, M. T., 1904. On the theory of elastic solid contact. *Annln Physics*, 14, 153-162.

Hussain, M. A., Pu, S. L. and Underwood, J., 1974. Strain energy release rate for a crack under combined mode I and mode II. In Paris PC, Irwin G. R. editors. Fracture Analysis, ASTM STP 560, Philadelphia, 2-28.

Ikeda, T., Miyazaki, N. and Soda, T., 1998. Mixed mode fracture criterion of interface crack between dissimilar materials. *Engineering Fracture Mechanics*, 69(6), 725-735.

Inglis, C. E., 1913. Stresses in a plate due to the presence of cracks and sharp corners. *Transactions of the Institute of Naval Architects*, 55, 219-241.

Irwin, G. R., 1956. Onset of fast crack propagation in high strength steel and aluminium alloys.

Sagamore Research Conference Proceedings, 2, 289-305.

Irwin, G. R., 1957. Analysis of stresses and strains near the end of a crack traversing a plate. *Journal of Applied Mechanics*, 24, 361-364.

Jaeger, J. C. and Cook, N. G. W., 1969. Fundamentals of rock mechanics. London: Methuen

Jefferson, A. D., 1989. Finite element analysis of composite structures. *PhD Thesis*, University of Wales College of Cardiff.

Jelagin, D., and Larsson, P-L., 2007. Hertzian fracture at finite friction: A parametric study. *Wear*, 265, 840–848.

Jin, F., Zhang, C., Hu, W. and Wang, J., 2011. 3D mode discrete element method: Elastic model. *International Journal of Rock Mechanics & Mining Sciences*, 48, 59–66.

Jirásek, M., 2006. Modelling of localized inelastic deformation. Lecture notes, Czech Technical University.

Jirásek, M., 2011. Damage and smeared crack models. *Numerical Modelling of Concrete Cracking*, 532, 1-49.

Johnson, K. L., O'Connor, J. J. and Woodward, A. C., 1973. The effect of indenter elasticity on the Hertzian fracture of brittle materials. *Proceeding of the Royal Society: Mathematical, Physical & Engineering Sciences*, A334, 95-117.

Jong, G. S., In, S. N. and Sahng, J. Y., 1997. A finite element approach to anisotropic damage of ductile materials in large deformations-Part I: An anisotropic ductile elastic-plastic-damage model. *International Journal of Fracture*, 84, 161-277.

Ju, J. W., 1989. On energy-based coupled elasto-plastic damage theories: constitutive modeling and computational aspects. *International Journal of Solid Structures*, 7, 803-833.

Karihaloo, B. L. and Xiao, Q. Z., 2003. Modelling of stationary and growing cracks in FE framework without remeshing: a state-of the-art-review. *Computers and Structures*, 81, 119-129.

Kawai, T., 1977. New element models in discrete structural analysis. *Japan Society of Naval Architects*, 141-174.

Kawai, T., Kawabata, K. Y., Kondou, I. and Kumagai, K. 1978. A new discrete model for analysis of solid mechanics problems. In Proceedings of the 1st Conference on Numerical

Methods and Fracture Mechanics, Swansea.

Khoei, A. R., Moslemi, H. and Sharifi, M., 2012. Three-dimensional cohesive fracture modeling of non-planar crack growth using adaptive FE technique. *International Journal of Solids and Structures*, 49, 2334–2348.

Klerck, P. A., Sellers, E. J. and Owen, D. R. J., 2004. Discrete fracture in quasi-brittle materials under compressive and tensile stress states. *Computer Methods in Applied Mechanics and Engineering*, 193, 3035-3056.

Knight, C. G., Swain, M. V. and Chaudhri, M. M., 1977. Impact of small steel spheres on glass surfaces. *Journal of Materials Science*, 12(8), 1573-1586.

Knott, J. F., 1973. Fundamentals of fracture mechanics, New York: John Wiley-Halsted Press.

Kolsky, H., 1949. An investigation of the mechanical properties of materials at very high rates of loading. *Proceedings of the Physical Society Section B*, 62, 676–700.

Kolsky, H., 1953. Stress waves in solids. Oxford: Clarendon Press.

Komvopoulos, K., 1996. Subsurface crack mechanisms under indentation loading. *Wear*, 199,

9-23.

Krätzig, W. B. and Pölling, R., 1998. Elasto-plastic damage-theories and elasto-plastic fracturing-theories – a comparison. *Computational Materials Science*, 13, 117–131.

Kruzic, J.J., Kim, D.K., Koester, K.J. and Ritchie, R.O., 2009. Indentation techniques for evaluating the fracture toughness of biomaterials and hard tissues. *Journal of the Mechanical Behavior of Biomedical Materials*, 2(4), 384–395.

Lajtai, E. Z., 1971. A theoretical and experimental evaluation of the Griffith theory of brittle fracture. *Tectonophysics*, 11(2), 129-156.

Lajtai, E. Z., 1974. Brittle fracture in compression. *International Journal of Fracture*, 10(4), 525-536.

Lajtai, E. Z., Carter, B. J. and Ayari, M. L., 1990. Criteria for brittle fracture in compression. *Engineering Fracture Mechanics*, 37(1), 59-74.

[Laminated Glass (SR002)] n.d. [image online] Available at: <http://image.made-in-china.com/2f0j00ueqEipldAhkF/Laminated-Glass-SR002-.jpg> [Accessed 27 January 2013]

Lawn, B. R., Evans, A. G. and Marshall, D. B., 1980. Elastic/Plastic indentation damage in ceramics: the median/radial crack system. *Journal of the American Ceramic Society*, 63, 574-581.

Lawn, B. R., and Swain, M. V., 1975. Microfracture beneath point indentations in brittle solids. *Journal of Materials Science*, 10(1), 113-122.

LeBlanc, M. M. and Lassila, D. H., 1993. Dynamic tensile testing of sheet material using the Split Hopkinson Bar technique. *Experimental Techniques*, 17(1), 37–42.

Le Bourhis, E., 2008. Glass: mechanics and technology. Wiley-VCH Verlag Gmbh & Co. KGaA.

Ledbetter, L.R., Walker, A. R. and Keiller, A. P., 2006. Structural use of glass. *Journal of Architectural Engineering*, 12(3), 137-149.

Leguillon, D., 2002. Strength or toughness? A criterion for crack onset at a notch. *European Journal of Mechanics - A/Solids*, 21(1), 61-72.

Leguillon, D., Laurencin, J. and Dupeux, M., 2003. Failure initiation in an epoxy joint

between two steel plates. *European Journal of Mechanics - A/Solids*, 22(4), 509-524.

Lindholm, U. S., 1964. Some experiments with the split Hopkinson pressure bar. *Journal of the Mechanics and Physics of Solids*, 12(5), 317–335.

Linger, K. R. and Holloway, D. G., 1968. The fracture energy of glass. *Philosophical Magazine*, 18(156), 1269-1280.

Lisjak, A. and Grasselli, G., 2010. Rock impact modelling using FEM/DEM. *DEM5 Munjiza A. (ed.),* 269-274.

Liu, P. F. and Zheng, J. Y., 2010. Recent developments on damage modeling and finite element analysis for composite laminates: A review. *Materials & Design*, 31(8), 3825–3834.

Logan, J. M., 1979. Brittle phenomena. *Reviews of Geophysics*, 17(6), 1121-1132.

Love, A. E. H., 1892. *A treatise on the mathematically theory of elasticity*, Cambridge University Press, UK

Love, A. E. H., 1944. *A treatise on the mathematically theory of elasticity*. New York : Dover Publications

LSTC, 2004. Ls- Pre/Post Training. 8th International Ls-DYNA user conference post conference training.

LSTC, 2007. LS-DYNA user manual.

Lukas, T. and Munjiza, A., 2010. Parallelization of an open-source FEM/DEM code Y2D. *DEM5 Munjiza A. (ed.)*, 206-211.

[MacMillan ballet highlight of Royal Opera House's new season] n.d. [image online] Available at: < http://www.telegraph.co.uk/culture/theatre/dance/8449107/MacMillan-ballet -highlight-of-Royal-Opera-Houses-new-season.html > [Accessed 27 January 2013]

Mahabadi, O. K., Grasselli, G. and Munjiza, A., 2010. Y-GUI: A graphical user interface and pre-processor for the combined finite-discrete element code, Y2D, incorporating material heterogeneity. *Computers & Geosciences*, 36(2), 241–252.

Malvar, L. J. and Warren, G. E., 1988. Fracture energy for three-point-bend tests on single-edge-notched beams. *Experimental Mechanics*, 28(3), 266-272.

Malvar, L. J. and Fourney, M. E., 1990. A three dimensional application of the smeared crack

approach. *Engineering Fracture Mechanics*, 35, 251-260.

Masters, F. J., Gurley, K. R., Shah, N. and George, F., 2010. The vulnerability of residential window glass to lightweight windborne debris. *Engineering Structures*, 32, 911-921.

Matwejeff, S. N., 1931. Criminal investigation of broken window panes. *The American Journal of Police Science*, 2(2), 148-157.

McJunkins, S. P. and Thornton, J. I., 1973. Glass fracture analysis. A review. *Forensic Sciences*, 2, 1-27

Melenk, J. M. and Babuska, I., 1996. The partition of unity finite element method: basic theory and applications. *Computer Methods in Applied Mechanics and Engineering*, 139, 289–314.

Melin, S., 1986. When does a crack grow under mode II conditions? *International Journal of Fracture*, 30(2), 103-114.

Melin, S., 1987. Fracture from a straight crack subjected to mixed mode loading. *International Journal of Fracture*, 32(4), 257-263.

[mimosa.com.sg] n.d. [image online] Available at: <http://mimosa.com.sg/site/glass-/Lami%20Glass.htm> [Accessed 15 April 2010]

Minor, J. E., 1994. Windborne debris and the building envelope. *Journal of Wind Engineering and Industrial Aerodynamics*, 53, 207-227.

Minor, J. E., Beason, W. L. and Harris, P. L., 1978. Designing for windborne missiles in urban areas. *Journal of the Structural Division, ASCE*, 104(11), 1749-1760.

Minor, J. E. and Norville, H. S., 2006. Design of window glass for lateral pressures. *Journal of Architectural Engineering*, 12(3), 116-121.

Moes, N., Dolbow, J. and Belytschko, T., 1999. A finite element method for crack growth without remeshing. *International Journal for Numerical Methods in Engineering*, 46, 131–150.

Morais, A. B. and Pereira, A. B., 2006. Mixed mode I+II interlaminar fracture of glass/epoxy multidirectional laminates – Part 1: Analysis. *Composites Science and Technology*, 66, 1889-1895.

Morris, J. P., Glenn, L. A. and Blair, S. C., 2003. The distinct element method - application to

structures in jointed rock. *Lecture Notes in Computational Science and Engineering: Meshfree Methods for Partial Differential Equations*, 26, 291-306.

Morris, J. P., Rubin, M. B., Block, B. I. and Boner, M. P., 2006. Simulations of fracture and fragmentation of geologic materials using combined FEM/DEM analysis. *International Journal of Impact Engineering*, 33, 463-473.

Munjiza, A., 1992. Discrete elements in transient dynamics of fractured media. Ph.D. thesis, Department of Civil Engineering, University of Wales, Swansea.

Munjiza, A., 2000. *Manual for the "Y" computer program*.

Munjiza, A., 2004. *The combined finite-discrete element method*. John Wiley and Sons.

Munjiza, A., 2008. Modelling fracture and fragmentation using open source FEM/DEM. *European Journal of Environmental and Civil Engineering*, 12, 1007-1030.

Munjiza, A., Andrews, K. R. F., White. J. R., 1997. Discretized contact solution for combined finite–discrete method. 5th ACME Conference, London UK, 96–100.

Munjiza, A., Andrews, K. R. F., 1998. NBS contact detection algorithm for bodies of similar size. *International Journal for Numerical Methods in Engineering*, 43(1), 131-149.

Munjiza, A., Andrews, K. R. F. and White, J. K., 1999. Combined single and smeared crack model in combined finite-discrete element analysis. *International Journal for Numerical Methods in Engineering*, 44(1), 41-57.

Munjiza, A., Andrews, K. R. F., 2000. Penalty function method for combined finite–discrete element systems comprising large number of separate bodies. *International Journal for Numerical Methods in Engineering*, 49, 1377–1396.

Munjiza, A., Bangash, T. and John, N. W. M., 2004. The combined finite-discrete element method for structural failure and collapse. *Engineering Fracture Mechanics*, 71, 469-483.

Munjiza, A. and Bicanic, N., 1994. A combined finite/discrete element approach to the simulation of progressive material fracture, Department of Civil Engineering, University of Wales, Swansea, UK, Report No. CR/828/94.

Munjiza, A. and John, N. W. M., 2002. Mesh size sensitivity of the combined FEM/DEM fracture and fragmentation algorithms. *Engineering Fracture Mechanics*, 69, 281-295.

Munjiza, A., Knight, E. and Rougier, E., 2011. *Computational Mechanics of Discontinua*. John Wiley and Sons.

Munjiza, A., Owen, D. R. J. and Bicanic, N., 1995. A combined finite-discrete element method in transient dynamics of fracturing solids. *Engineering Computations*, 12, 145-174.

Murgatroyd, J. B., 1942. The significance of surface marks on fractured glass, *The Society of Glass Technology*, 26, 153-155.

Mustoe, G. G. W., 1992. A generalized formulation of the discrete element method. *Engineering Computations*, 9(2), 181-190.

Myer, L. R., Kemeny, J. M., Zheng, Z., Suarez, R., Ewy, R. T. and Cook, N. G. W., 1992. Extensile cracking in porous rock under differential compressive stress. *Applied Mechanics Reviews*, 45, 263-280.

Needleman, A., 1987. A continuum model for void nucleation by inclusion debonding. *Journal of Applied Mechanics*, 54, 525-531.

Nechnech, W., Meftah, F. and Reynouard, J. M., 2002. An elasto-plastic damage model for

plain concrete subjected to high temperatures. *Engineering Structures*, 24(5), 597–611.

Ngo, D. and Scordelis, A. C., 1967. Finite element analysis of reinforced concrete beams. *Journal of the American Concrete Institute*, 64, 152-163.

Nijsse, R., 1993. Glass: a building material. Abt.

Norville, H. S., 1999. Strength factor for laminated glass. Glass processing days 1999, Tampere, Finland, 357-359

Norville, H. S. and Conrath, E. J., 2006. Blast-resistance glazing design. *Journal of Architectural Engineering*, 12(3), 129-136.

Norville, H. S., King, K. W. and Swofford, J. L., 1998. Behaviour and strength of laminated glass. *Journal of Engineering Mechanics ASCE*, 124(1), 46-53.

Nuismer, R. J., 1975. An energy release rate criterion for mixed mode fracture. *International Journal of Fracture*, 11(2), 245-250.

Oda, J., Zang, M. Y., Mori, T. and Tohyama, K., 1995. Simulation of dynamic fracture behavior of laminated glass by DEM. Trans 8th Calculation Dynamics Symp JSME, 429–430.

Oda, J. and Zang, M. Y., 1998. Analysis of impact fracture behaviour of laminated glass of bi-layer type using discrete element method. *Key Engineering Materials*, 145–149, 349–354.

Oliver, J., 1995. Continuum modelling of strong discontinuities in solid mechanics using damage models. *Computational Mechanics*, 17, 49-61.

Ougier-Simonin, A., Fortin, J., Guéguen, Y., Schubnel, A., Bouyer, F., 2011. Cracks in glass under triaxial conditions. *International Journal of Engineering Science*, 49, 105–121.

Owen, D. R. J., Feng, Y. T., de Souza Neto, E. A., Cottrell, M. G., Wang, F., Andrade Pires, F. M. and Yu, J., 2004. The modelling of multi-fracturing solids and particulate media. *International Journal for Numerical Methods in Engineering*, 60, 317-339.

Paraview, 2010. Paraview user's guide.

Park, B. J., Choi, Y. J. and Chu, C. N., 2002. Prevention of exit crack in micro drilling of soda-lime glass. *CIRP Annals - Manufacturing Technology*, 51(1), 347-350.

Park, T. and Voyiadjis, G. Z., 1997. Damage analysis and elasto-plastic behaviour of metal matrix composites using the finite element method. *Engineering Fracture Mechanics*, 56(5),

623-646.

Petrangeli, M. and Ožbolt, J., 1996. Smeared crack approaches—material modelling. *Journal of Engineering Mechanics*, 122, 545-553.

Pine, R. J., Owen, D. R. J., Coggan, J. S. and Rance, J. M., 2007. A new discrete fracture modelling approach for rock masses. *Géotechnique*, 57(9), 757-766.

Preston, F. W., 1926. A study of the rupture of glass. *Journal of the Society of Glass Technology*, 10, 234-269.

Pyttel, T., Liebertz, H. and Cai, J., 2011. Failure criterion for laminated glass under impact loading and its application in finite element simulation. *International Journal of Impact Engineering*, 38(4), 252–263.

Quinn, G. D. and Bradt, R. C., 2007. On the Vickers indentation fracture toughness test. *Journal of the American Ceramic Society*, 90(3), 673–680.

Rama Chandra Murthy, A., Palani, G. S. and Lyer, N. R., 2009. State-of-the-art review on fracture analysis of concrete structural components. *Sadhana*, 34(2), 345-367.

Rao, C. V. S. K., 1984. Safety of glass panels against wind loads. *Engineering Structures*, 6(3), 232-234

Rao, Q., Sun, Z., Stephansson, O., Li, C. and Stillborg, B., 2003. Shear fracture (Mode II) of brittle rock. *International Journal of Rock Mechanics and Mining Sciences*, 40(3), 355–375.

Rashid, M. M., 1998. The arbitrary local mesh refinement method: an alternative to remeshing for crack propagation analysis. *Computer Methods in Applied Mechanics and Engineering*, 154, 133-150.

Rashid, Y. R., 1968. Ultimate strength analysis of prestressed concrete pressure vessels. Nuclear Engineering and Design, 7(4), 334–344.

Repetto, E. A., Radovitzky, R. and Ortiz, M., 2000. Finite element simulation of dynamic fracture and fragmentation of glass rods. *Computer Methods in Applied Mechanics and Engineering*, 183, 3-14.

Rice, J. R., 1968. A path independent integral and the approximate analysis of strain concentration by notches and cracks. *Journal of Applied Mechanics*, 35, 379-386.

Robertas, B., Algis, D. and Rimantas, K, 2004. Discrete element method and its application to

the analysis of penetration into granular media. *Journal of Civil Engineering and Management*, 10(1), 3-14.

Roesler, F. C., 1956. Brittle fractures near equilibrium. *Proceedings of the Physical Society. Section B*, 69(10), 981-992.

Rots, J. G., 1986. Strain-softening analysis of concrete fracture specimens. In Fracture Toughness and Fracture Energy of Concrete, Wittmann, F. H. (ed.). Elsevier Science Publishers: Amsterdam, Netherlands, 137–148.

Rots, J. G., 1991. Smeared and discrete representations of localized fracture. *International Journal of Fracture*, 51, 45-59.

Rougier, E., Munjiza, A. and John, N. W. M., 2004. Numerical comparison of some explicit time integration schemes used in DEM, FEM/DEM and molecular dynamics. *International Journal for Numerical Methods in Engineering*, 61(6), 856–879.

Roylance, D., 2001. Introduction to fracture mechanics.

Salman, A. D. and Gorham, D. A., 2000. The fracture of glass spheres. *Powder Technology*, 107, 179–185.

Scholtes, L., Donze, F-V., 2012. Modelling progressive failure in fractured rock masses using a 3D discrete element method. *International Journal of Rock Mechanics & Mining Sciences*, 52, 18–30.

Schrefler, B. A., Secchi, S. and Simoni, L., 2006. On adaptive refinement techniques in multi-field problems including cohesive fracture. *Computer Methods in Applied Mechanics and Engineering*, 195, 444–461.

[Sears Tower Scary Glass Viewing Platform] n.d. [image online] Available at: < http://www.tafreehmela.com/tafreeh/84280-sears-tower-scary-glass-viewing-platform.html > [Accessed 27 January 2013]

Sedlacek, G., Blank, K. and Gusgen, J., 1995. Glass in structural engineering. *The Structural Engineer*, 73(2), 17-22.

Setoodeh, A. R., Malekzadeh, P., Nikbin, K., 2009. Low velocity impact analysis of laminated composite plates using a 3D elasticity based layerwise FEM. *Materials & Design*, 30(9), 3795–3801.

Shand, E. B., 1954. Experimental study of the fracture of glass. I. The fracture process,

Journal of the American Ceramic Society, 37(2), 52-59

Shen, B., Stephansson, O., Einstein, H. H. and Ghahreman, B., 1995. Coalescence of fractures under shear stresses in experiments. *Journal of Geophysical Research: Solid Earth*, 100(B4), 5975–5990.

Shutov, A. I., Frank, A. N., Novikov, I. A., Ostapko, A. S. and Bonchuk, A. S., 2004. Testing laminated glass for impact resistance. *Glass and Ceramics*, 61(3-4), 67-69.

Sih, G. C., 1974. Strain energy density factor applied to mixed mode crack problems. *International Journal of Fracture*, 10(3), 305-321.

Simo, J. C. and Ju, J. W., 1987. Strain- and stress-based continuum damage models—I. Formulation. *International Journal of Solids and Structures*, 23(7), 821–840.

SIMULIA, 2004. ABAQUS/CAE user's manual.

SIMULIA, 2011. Introduction to XFEM.

Smith, D. J., Ayatollahi, M. R. and Pavier, M. J., 2001. The role of *T*-stress in brittle fracture for linear elastic materials under mixed-mode loading. *Fatigue & Fracture of Engineering*

Materials & Structures, 24(2), 137-150.

Strouboulis, T., Babuska, I. and Copps, K., 2000. The design and analysis of the generalized finite element method. *Computer Methods in Applied Mechanics and Engineering*, 181, 43–69.

Strouboulis, T., Copps, K. and Babuska, I., 2000. The generalised finite element method: an example of its implementation and illustration of its performance. *International Journal for Numerical Methods in Engineering*, 47, 1401–1417.

Strouboulis, T., Copps, K. and Babuska, I., 2001. The generalized finite element method. *Computer Methods in Applied Mechanics and Engineering*, 190, 4081–4193.

Sukumar, N., Moes, N., Moran, B. and Belytschko, T., 2000. Extended finite element method for three-dimensional crack modelling. *International Journal for Numerical Methods in Engineering*, 48, 1549–1570.

Sun, X. and Khaleel, M. A., 2004. Modelling of glass fracture damage using continuum damage mechanics - static spherical indentation. *International Journal of Damage Mechanics*, 13, 263-285.

Sun, X., Khaleel, M. A. and Davies, R. W., 2005. Modelling of stone-impact resistance of monolithic glass ply using continuum damage mechanics. *International Journal of Damage Mechanics*, 14, 165-178.

Sun, X., Khaleel, M. A. and Davies, R. W., 2005. Modelling of stone-impact resistance of monolithic glass ply using continuum damage mechanics. *International Journal of Damage Mechanics*, 14, 165-178.

Sutton, M. A., Deng, X., Ma, F., Newman, Jr. J. C., and James, M., 2000. Development and application of a crack tip opening displacement-based mixed mode fracture criterion. *International Journal of Solids and Structures*, 37(20), 3591-3618.

Taylor, E. A. and McDonnell, J. A. M., 1997. Hypervelocity impact on soda lime glass: damage equations for impactors in the 400-2000 m range. *Advances in Space Research*, 20(8), 1457-1460.

Taylor G. I., 1946. The testing of materials at high rates of loading. *Journal of the Institute of Civil Engineers*, 26:486–519.

Tian, Y. P., Fu, Y. M and Wang, Y., 2009. Nonlinear dynamic response of piezoelectric

elasto-plastic laminated plates with damage. *Composite Structures*, 88, 169-178.

Tillet, J. P. A., 1956. Fracture of glass by spherical indenters. *Proceedings of the Physical Society Section B*, 69(1), 47-54.

Timmel, M., Kolling, S., Osterrieder, P. and Du-Bois, P. A., 2007. A finite element model for impact simulation with laminated glass. *International Journal of Impact Engineering*, 34, 1465-1478.

Timoshenko, S. and Prokop, S., 1959. *Theory of plates and shells*, McGraw-Hill, Newyork, USA

Toakley, A. R., 1977. Stresses and safety levels for glass liable to human impact. *Building and Environment*, 12, 87-95.

Tong, P. and Pian, T. H. H., 1973. On the convergence of the finite element method for problems with singularity. *International Journal of Solids and Structures*, 9, 313–321.

[Top tourist attraction - "Grand canyon skywalk"] n.d. [image online] Available at: < http://www.balcanexpres.com/2012/10/top-tourist-attraction-grand-canyon.html> [Accessed 27 January 2013]

Tsai, Y. M. and Kolsky, H., 1967. A study on the fractures produced in glass blocks by impact. *Journal of the Mechanics and Physics of Solids*, 15(4), 263-278.

Vallabhan, C. V. G., Das, Y. C., Magdhi, M., Asik, M. Z. and Bailey, J. B., 1993. Analysis of laminated glass units. *Journal of Structural Engineering ASCE*, 119(5), 1572-1585.

Vallabhan, C. V. G., Das, Y., and Ramasamudra, M., 1992. Properties of PVB interlayer used in laminated glass. *Journal of Materials in Civil Engineering*, 4(1), 71–76.

Varner, J. R., Hallwig, W. and Walter, A., 1980. Impact damage on annealed and on tempered flat glass. *Journal of Non-Crystalline Solids*, 38-39, Part 1, 413–418.

Wang, E. Z. and Shrive, N. G., 1993. On the Griffith criteria for brittle fracture in compression. *Engineering Fracture Mechanics*, 46(1), 15-26.

Wang, E. Z. and Shrive, N. G., 1995. Brittle fracture in compression: mechanisms, models and criteria. *Engineering Fracture Mechanics*, 52(6), 1107-1126.

Wang, F, Feng, Y. T., Owen, D. R. J., Zhang, J. and Yang, L., 2004. Parallel analysis of

combined finite/discrete element systems on PC cluster. *Acta Mechanica Sinica*, 20(5), 534-540.

Ward, J. B., 1987. Analysis of glass fracture. *Materials & Design*, 8(2), 100-103.

Warren, P. D. and Hills, D. A., 1994. The influence of elastic mismatch between indenter and substrate on Hertzian fracture. *Journal of Material Sciences*, 29(11), 2860-2866.

Weihe, S., Kröplin, B. and Borst, R. De, 1998. Classification of smeared crack models based on material and structural properties. *International Journal of Solids and Structures*, 35(12), 1289–1308.

Westergaard, H. M., 1939. Bearing pressures and cracks. *Journal of Applied Mechanics*, 6, 1939, 49-53

Williams, J. R., 1988. Contact analysis of large numbers of interacting bodies using discrete modal methods for simulating material failure on the microscopic scale. *Engineering Computations*, 3, 197-209.

Whirley, R. G., Englemann, B. E. and Halquist, J. O., 1992. DYNA2D, a nonlinear, explicit, two dimensional finite element code for solid mechanics. User manual, Lawrence Livermore

National Laboratory Report, UCRL-MA-110630.

Wu, C. H., 1978. Fracture under combined loads by maximum energy release rate criterion. *Journal of Applied Mechanics*, 45(3), 553-558.

Xiang, J., Munjiza, A., Latham, J-P. and Guises, R, 2009. On the validation of DEM and FEM/DEM models in 2D and 3D. *Engineering Computations: International Journal for Computer-Aided Engineering*, 26(6), 673-687.

Xu, J., Li, Y., Chen, X., Yan, Y., Ge, D., Zhu, M. and Liu, B., 2010. Characteristics of windshield cracking upon low-speed impact: numerical simulation based on the extended finite element method. *Computational Materials Science*, 48, 582-588.

Xu, X. P. and Needleman, A., 1994. Numerical simulations of fast crack growth in brittle solids. *Journal of the Mechanics and Physics of Solids*, 42, 1397–1434.

Yosibash, Z., Priel, E. and Leguillon, D., 2006. A failure criterion for brittle elastic materials under mixed-mode loading. *International Journal of Fracture*, 141, 291-312.

Young, T., 1807. *A Course of Lectures on Natural Philosophy and the Mechanical Arts: Vol. l*, London: Joseph Johnson, 144-148.

Zang, M. Y., Lei, Z. and Wang, S. F., 2007. Investigation of impact fracture behavior of automobile laminated glass by 3D discrete element method. *Computational Mechanics*, 41(1), 73-83.

Zhang, Y. Y. and Chen, L., 2009. Impact simulation using simplified meshless method. *International Journal of Impact Engineering*, 36(5), 651-658.

Zhao. S., Dharani, L. R., Chai, Li. and Barbat, S. D., 2006. Analysis of damage in laminated automotive glazing subject to simulated head impact. *Engineering Failure Analysis*, 13, 582-597.

Zhou, C. Y. and Zhu, F. X., 2010. An elasto-plastic damage constitutive model with double yield surfaces for saturated soft rock. *International Journal of Rock Mechanics & Mining sciences*, 47, 385-395.

Zienkiewicz, O. C., 1995. Origins, milestones and directions of the finite element method – a personal view. *Achieves of Computational Methods in Engineering*, 2, 1-48.

Zienkiewicz, O. C. and Taylor, R. L., 1967. *The finite element method*. McGraw-Hill.

Zienkiewicz, O. C., Valliappan, S. and King, I. P., 1969. Elasto-plastic solutions of engineering problems 'initial stress': finite element approach. *International Journal for Numerical Methods in Engineering*, 1, 75-100.

Zimmermann, E. A., Launey, M. E. and Ritchie, R. O., 2010. The significance of crack-resistance curves to the mixed-mode fracture toughness of human cortical bone. *Biomaterials*, 30(20), 5297–5305.